

Abstract

ZHANG, NINGYI. Fabrication and Utilization of PVDF Piezoelectric Thin Films Using Additive Manufacturing for Structural Health Monitoring. (Under the direction of Dr. Fuh-Gwo Yuan and Dr. Jingyan Dong).

Piezoelectric materials have the ability to transfer energy between electric field and force field. Compared with other polymer materials such as nylon and polyvinyl chloride, polyvinylidene fluoride (PVDF) has better piezoelectric properties. Therefore, there is considerable interest in materials that can improve the effective stress constants beyond the inherent sensitivity of PVDF devices. So far, the research focus is on improving material properties, such as optimizing drawing ratio and polarization temperature or applying high electric field.

In recent years, additive manufacturing (AM) technology has been applied more and more widely in the fields of microelectronics, magnetism and micromachineries. Progress in these areas depends on the ability to selectively and accurately print different components and materials into embedded or composite structures. The advantage of AM technology also included that it could accurately control the electrical field, the temperature and other parameters during the process. The potential application of AM technology in fabrication of PVDF sensor and smart structure could result in a great improvement on the performance of the sensor and at the same time a much-reduced manufacture cost.

It is well known that PVDF mainly have four phase structures, α phase, β phase, γ phase, and δ phase, depending on the chain conformations. Among all of those phases, the β phase possesses the highest dipole moments, and as a result, best piezoelectric performance. However, our current understanding of PVDF β phase formation mechanisms, including several thermodynamic calculations and molecular kinetic simulations, are limited and defective. Because those previous theories only consider the initial and final status of crystal phases, can provide some general explanation about the phenomenon, but are not able to provide the real guidance for the processing. Thus, the current processing for β phase PVDF is based on the empirical results instead of solid theoretical foundation. It would hinder the performance of PVDF by additive manufacturing. In this study, the author proposed a new mechanism on the α

to β transformation. The optimized PVDF piezoelectric films were obtained depending on the guidance of the mechanism, along with the AM technology.

In this study, the PVDF printing inks were initially synthesized using solution mixing process and then were printed on substrate under in-situ electric field. We further characterized our samples by using X-ray Diffraction (XRD), Fourier-transform infrared spectroscopy (FTIR), and Scanning Electron Microscope (SEM). The piezoelectric coefficients of those printed films were then measured. The β content and crystallinity were discussed with respect to the printing parameters including the selection of solvent, the solution concentration, the doped additives, printing temperature, printing speed, working voltage, and post printing treatment.

In order to obtain a high piezoelectric performance, the poling process on the printing platform was also analyzed and discussed. Besides, the printed PVDF thin films had a special electret structure, which may render some unique electrostrictive and piezoelectric behavior. The sensitivity evaluation of the printed PVDF thin film sensors without poling was conducted in both 33 and 31 modes. The characterized PVDF sensors exhibited relatively high d_{33} and d_{31} values than other unpolarized samples. The sensitivity of them can even comparable to the polarized commercial samples.

Fabrication and Utilization of PVDF Piezoelectric Thin Films Using Additive Manufacturing for
Structural Health Monitoring

by
Ningyi Zhang

A dissertation submitted to the Graduate Faculty of
North Carolina State University in
partial fulfillment of the
requirements for the degree of
Doctor of Philosophy

Mechanical Engineering

Raleigh, North Carolina

2019

APPROVED BY:

Dr. Fuh-Gwo Yuan
Chair of Advisory Committee

Dr. Jingyan Dong
Co-Chair of Advisory Committee

Dr. Larry Silverberg

Dr. Xiaoning Jiang

Biography

Ningyi Zhang attended the Central South University at Changsha, China and graduated from the material science in 2005. In 2008 he graduated from Powder Metallurgy Research Institute in Central South University and acquired the MS degree in material science. In 2013 he began his study in mechanical engineering at North Carolina State University, under Dr. Fuh-Gwo Yuan. His research interests include smart materials and structures, piezoelectric material, and additive manufacturing.

Acknowledgements

First of all, I would like to express my deepest gratitude to Dr. Fuh-Gwo Yuan, my advisor, for your support and guidance during the course of this project. I am so grateful for your patience, willingness and encouragement that developed my understanding and comprehension of the topics of graduate study. Not only in academia, but also in all aspects of my life. It is a real privilege to know and learn from such a competent and sincere person.

Thanks to Dr. Ying Luo and Dr. Caifeng Chen from Jiangsu University for your impartial assistance, especially with the laboratory items and testing facilities. I'll never forget what you've done for me, when I need it most!

Additional thanks go to the members of my committee members, Dr. Jingyan Dong, Dr. Larry Silverberg, Dr. Xiaoning Jiang, and Dr. Yuan-Shin Lee, for their assistance with the thesis and its defense, as well as Dr. Wenbin Huang and Dr. Xinjia Li for their help with sensitivity characterization. Thanks to Dr. Yiwei Han and Dr. Hantang Qin for introducing me to this area. Thanks to Dr. Weiyi Chang for assistance with PFM studies, and to all members of the research team for your valuable suggestions and constructive discussions throughout my involvement with this study.

To Mr. Yuan Zhu and Mr. Feixiang Cai, I don't think I need to say thank you. Because you're my brothers, for the whole life. Let's keep going together, and I'm sure we can do something big. Hurry up!

I would also like to thank my dear parents, who have constantly encouraged me to stick to my goals. I know exactly how hard these years came. I've never expected the journey I chose would be so long and so tough. Too many times, I doubted my decision, doubted the value of my research, even doubted everything in my life. But I hold one thing for sure: YOU ARE ALWAYS OUT THERE. I certainly wouldn't have made it this far without you. Dad, look at it. I become even better than you expected.

And Mama, I'm Coming Home!

Table of contents

Nomenclature	xii
1. Introduction and Background	1
1.1. Structural health monitoring (SHM)	1
1.2. Embedded smart composite structures.....	4
1.2.1. The basic concept of smart composite structures	5
1.2.2. The effects of embedded sensor/actuator on the integrity of the structures.....	7
1.2.3. The fabrication methods for the embedded smart composite structures.....	10
1.3. Additive manufacturing (AM) technology.....	14
1.3.1. Basic definition and development history of AM technology	14
1.3.2. Application of AM technology in sensors and other electronic devices.....	17
1.4. Introduction to polyvinylidene fluoride (PVDF)	19
1.4.1. The basics of piezoelectricity and ferroelectricity	21
1.4.2. The piezoelectricity of PVDF and its application in sensors/actuators	28
1.4.3. Structure and phase conformation in PVDF	32
1.4.4. Piezoelectric mechanism for PVDF.....	36
1.4.5. The conventional manufacturing processes for β phase PVDF	38
1.4.6. Material characterization methods for PVDF	42
1.5. Description of the fundamental problems.....	53
1.5.1. Basic design of the PVDF sensors	53
1.5.2. Wiring and metallic electrodes.....	55
1.5.3. Post-printing heat treatment and poling.....	57
1.5.4. The state of art in printed PVDF sensors/actuators	60
1.5.5. Motivation and challenges	63
1.6. Scope of thesis	65
2. Mechanisms of PVDF α to β phase transformation in printing process.....	67
2.1. The structural foundation of the proposed mechanism.....	68
2.1.1. Monomers	68
2.1.2. Chain Conformations	69
2.1.3. Phases.....	71

2.2.	The analysis of the basic G→T transition.....	76
2.3.	Central hypothesis: Physical process or Chemical process?.....	77
2.4.	Development of Gibbs energy under stress field and electrical field	79
2.5.	Verification and application of the proposed mechanism	81
2.5.1.	The term of internal energy.....	82
2.5.2.	The term of entropy	84
2.5.3.	The term of stress and electrical field	86
2.5.4.	The comprehensive analysis of the extended Gibbs-Helmholtz equation	89
2.6.	Analysis of melt and solid states processes.....	90
2.6.1.	The γ phase conformation.....	92
2.6.2.	The melt processing	92
2.6.3.	The solid state processing.....	94
3.	Fabrication and optimization of PVDF thin film by AM technology.....	96
3.1.	Processing of PVDF thin films	96
3.1.1.	Printing setup and apparatus	96
3.1.2.	Preparation of PVDF solvent.....	100
3.1.3.	The process control in printing	102
3.1.4.	SEM Results.....	105
3.2.	Parametric studies on the β -phase content of PVDF thin films.....	107
3.2.1.	The selection of solvents and additives.....	107
3.2.2.	The PVDF wt% of solutions on β phase production.....	110
3.2.3.	The doping of additives on the production of β phase.....	111
3.2.4.	The effect of voltage on β phase production.....	116
3.2.5.	The effect of printing speed on β phase production.....	118
3.2.6.	The effect of post printing treatment.....	121
4.	The integration of the poling process into the printing platform.....	125
4.1.	Conventional setup and parameters of poling processes	126
4.2.	Orientation of the ferroelectric dipoles	129
4.2.1.	The spatial distribution of dipoles after poling.....	129
4.2.2.	The estimation of effective poling time during printing and post treatment	132
4.2.2.	Ferroelectric switching time	136

4.2.3. The design and promotion of the poling instrument on the printing platform..	140
5. Sensitivity evaluation of the PVDF sensors.....	144
5.1. Sensor preparation	144
5.2. Piezoelectric characterization in 33 mode of operation.....	147
5.2.1. Piezoelectric Force Microscopy (PFM) test	149
5.2.2. The simplified model for the measured d_{33} values	154
5.2.3. The electret structure and giant electrostrictive	158
5.3. Piezoelectric characterization of PVDF sensors in 31 mode of operation.....	165
5.3.1. Experimental setup of instrument in 31 mode of operation.....	166
5.3.2. Testing d_{31} of PVDF thin film by the cantilever beam method	170
5.3.3. Free vibration sensing testing	173
6. Summary	180
References.....	181

List of tables

Table 1.1 3D printing chronology and milestones ²⁴	15
Table 1.2 Centrosymmetric in crystals with different symmetries	23
Table 1.3: Some material Properties of PVDF Film ³⁷	29
Table 1.4 Typical electroactive properties of various piezoelectric materials ³⁸	31
Table 1.5 Lattice constant of different phases in PVDF. ⁴²	35
Table 3.1 Conditions for printing solvent.....	101
Table 3.2 The crystallinity and β content of samples added with additives	115
Table 3.3 Electrical conductivity of the solvents and polymer solutions ⁷⁸	116
Table 4.1 Experimental conditions for corona poling process ⁷²	129
Table 5.1 Properties of the LDT1-028K sensor ¹²³	147
Table 5.2 The calculated d_{31} value with varied frequency	172

List of figures

Figure 1.1	A typical SHM system in aircraft.	3
Figure 1.2	A schematic of piezoelectric sensor network ⁵	6
Figure 1.3	The intelligent system and its relationship with the smart materials ¹¹	7
Figure 1.4	The influence of optical fibers on the fatigue lives for the embedded ¹²	9
Figure 1.5	The influence of embedded Copper foil on the compression properties ¹⁴	10
Figure 1.6	(a) Integration of PVDF sensors into 2D fabrics using dry fiber ²¹	11
Figure 1.7	The concept and structure of SMART layer ²²	12
Figure 1.8	A simple 2D to 3D conversion process of a smart layer ⁵	13
Figure 1.9	Examples of SMART Layers in basic shapes produced by Acellent, inc. ²³	13
Figure 1.10	The relationship between Piezoelectricity and Crystallographic structure ³²	23
Figure 1.12	Tensor directions for constitutive relation definitions ³³	24
Figure 1.13	A schematic view of an electrostrictive polymer, with a small AC ³²	28
Figure 1.14	Three monomer types in PVDF.....	32
Figure 1.15	Structure of conformation and crystal phases in PVDF.....	34
Figure 1.16	The lamellar crystal of PVDF crystal and its dipole orientation ³³	37
Figure 1.17	The stretching and polarization process in PVDF ³³	40
Figure 1.18	X-ray diffraction of Bragg's law ⁵⁶	43
Figure 1.19	The typical XRD patterns in PVDF (inset is the α phase) ⁴⁷	43
Figure 1.20	Schematic setup of a typical FTIR interferometer ⁵⁸	45
Figure 1.21	The ferroelectric and paraelectric phases adsorb peak ⁴³	46
Figure 1.21	The typic schematic of AFM ⁵⁶	48
Figure 1.23	The setup of Capacitance Measurement with LCR Meter.....	50
Figure 1.24	(a) The schematic of Sawyer-Tower circuit diagram.....	51
Figure 1.25	D-E loops at 1Hz under different electric fields for PVDF thin films ⁶⁴	52
Figure 1.26	Schematic of a typical PVDF piezoelectric sensor ³³	54
Figure 1.27	Schematic of the electrode poling system.....	58
Figure 1.28	Schematic of the corona poling system.....	59
Figure 2.1	The monomer of Polyvinylidene fluoride molecule.	68
Figure 2.2	Diagrams of (a) α -phase and (b) β -phase chain conformations in PVDF.....	70

Figure 2.3	The introduction of dipole perpendicular to the chain direction	71
Figure 2.4	(a)The conformation structure of $\alpha, \beta, \gamma, \delta$ phases in PVDF respectively.	73
Figure 2.5	The two-phase structure of PVDF ³⁸	75
Figure 2.6	The transition procedure of G and T status through the rotation.....	76
Figure 2.7	Phase diagram with respect to the VDF% of P(VDF-TrFE) at 1bar ⁴⁶	83
Figure 2.8	The percentage change of phase β , $F(\beta)$ ⁹⁶	85
Figure 2.9	The comparison of the chain length.....	88
Figure 2.10	Manufacturing chart for the α , β , γ and δ phases in PVDF.....	91
Figure 3.1	(a) The setup of near-field electrospinning (NFES) process. ⁷⁶	97
Figure 3.2	(a) The setup of the EHD printing. ¹⁰⁰	99
Figure 3.3	(a) 3D printing process for PVDF thin films,.....	100
Figure 3.4	The needles, the syringe, and the printing platform used in this study	104
Figure 3.5	SEM results for the (a) image of cross-section in PVDF thin film	106
Figure 3.6	XRD patterns of thin film prepared by 12wt% NMP and DMAC solvent.....	109
Figure 3.7	XRD patterns of thin film prepared by 14wt% GBL solvent	110
Figure 3.8	XRD patterns of PVDF thin films prepared with varied PVDF wt%.....	111
Figure 3.9	XRD patterns of PVDF thin films prepared with 15wt% PVDF	112
Figure 3.10	FT-IR results of PVDF thin films prepared with 15wt% PVDF	113
Figure 3.11	The XRD pattern of 14wt%PVDF in NMP	117
Figure 3.12	The XRD patterns of PVDF thin films prepared in GBL.....	119
Figure 3.13	The XRD patterns of PVDF thin films prepared in NMP	120
Figure 3.14	The integration of poling and post heat treatment	122
Figure 3.15	The XRD patterns of sample as printed and samples	123
Figure 4.1	The schematic of (a) the corona poling system	127
Figure 4.2	The space distribution of (a) space charges (SC) ⁶⁴	131
Figure 4.3	Surface potential map of glass collecting board.....	134
Figure 4.4	1-D potential map of substrate panel	135
Figure 4.5	Dependence of the activation field E_a on the reciprocal ¹²¹	138
Figure 4.6	Plots of the logarithm of switching times ¹²¹	139
Figure 4.7	The varied switching time as a function of applied field.....	140
Figure 4.8	The designs for prolong the effective poling time.....	141

Figure 4.9	The structure of printing platform showing the needle to electrode.....	143
Figure 5.1	PVDF sensor LDT1-028K ¹²³	146
Figure 5.2	PVDF film open circuit. (operated in d_{33} meters)	148
Figure 5.3	Schematic diagram of AFM operation ¹²⁵	150
Figure 5.4	The harmonic displacement response	151
Figure 5.5	The polynomial regression of displacement response	153
Figure 5.6	The distribution of the polarized region and the active region	155
Figure 5.7	Schematic diagram of a typical EHD printing process. ⁹⁸	159
Figure 5.8	Distribution of trapped electric charges ⁹⁸	160
Figure 5.9	Direct piezoelectric effect in electron irradiated PVDF-TrFE ¹²⁹	162
Figure 5.10	Longitudinal strain in a high-energy electron irradiated ³²	163
Figure 5.11	The mechanism for Giant electrostrictive effect.....	164
Figure 5.12	The setup of a Cantilever Beam ¹³²	167
Figure 5.13	Diagram showing (a) the voltage source ¹³²	168
Figure 5.14	Charge Amplifier Circuit Design ¹³²	169
Figure 5.15	The setup of d_{31} characterization tester system	170
Figure 5.16	A vibration measurement system (a) schematic (b) physical map	174
Figure 5.17	Output voltage of PVDF piezoelectric thin film.....	176
Figure 5.18	The voltage response signal in commercial PVDF sensor	177
Figure 5.19	The voltage response signal in printed PVDF sensor	177
Figure 5.20	Response of feedback signal to excitation signal	178

Nomenclature

PVDF Poly (Vinylidene Fluoride)

XRD X-ray diffraction

FTIR Fourier-transform infrared spectroscopy

Å 1 Angstrom (\AA) = 10^{-10} meter (m)

D Traditional dipole moment unit - Debye (D) = 3.34×10^{-30} C-m

T_g Glass transition temperature

T_c Curie transition temperature

T Mechanical stress - Pa = N/m^2

S Mechanical strain -dimensionless

E Electric intensity -V/m

D Electric displacement - C/m

ϵ^T, ϵ^S Permittivity- $\text{F/m} = \text{C}/(\text{mV})$

e Piezo constant - $\text{C/m}^2 = \text{N}/(\text{mV})$

d Piezo constant - $\text{m/V} = \text{C/N}$

g Piezo constant - $\text{m}^2/\text{C} = (\text{mV})/\text{N}$

c^E, c^D Elastic stiffness - Pa = N/m² = J/m³

s^E, s^D Compliance - Pa⁻¹ = m²/N = m³/J

ϵ_0 Permittivity of vacuum = 8.854x10⁻¹² (F/m)

d_{31} Transverse piezoelectric constant

d_{33} Longitudinal piezoelectric constant

A Piezoelectric film electrode area

q Electrical charge in the piezoelectric sensor

C_p Capacitance of the piezoelectric sensor

C_c Capacitance of the sensor wire leads

C_F Charge amplifier feedback loop capacitance

L Half of sensor length

h Sensor thickness

I Sensor cross-sectional moment of inertia

Q_e Electrical charge approximated at quasi-static conditions

1. Introduction and Background

Structural health monitoring (SHM) created demands for all kinds of innovative design of features and structures while the AM (Additive Manufacturing) technology can provide potential tools to realize them. The development of a general, in situ health monitoring system require the fabrication of better embedded smart sensor system. Despite the rapid progress of various designs and implementation of sensor systems for SHM, the smart structure that can seamlessly integrate embedded sensing systems with the composite structures was demanding and not well established. However simply embedding the sensors into the composite laminates may cause non-flat non-uniform structure with worse integrity. The non-uniform composite-sensor interfaces could be the critical sites of stress concentration, and significantly degrade the mechanical and fatigue properties of the structure. The initial goal of this study, therefore, was to illustrate the potential for AM technology to address this issue. Previous research in this area achieved great progresses on the printing of electrical circuit for varied kinds of sensors and other devices. Only in recent years, as the development of AM technology, the so called “all-printed” sensors became promising and closer to real application. It meant people were not only going to print the electrical circuit, but also to print the functional part of the sensors, including varied kinds of smart materials. Is it possible to find an appropriate material that can be printed and integrated in the structures to satisfy the SHM application? This is the primary question need to be answered in this study.

1.1. Structural health monitoring (SHM)

Structural health monitoring (SHM) can be defined as a methodology capable of monitoring the performance of structures throughout their operational service lifetime, while being able to identify various types and severity of damage incurred in a structure ¹. It is a revolutionary method for monitoring structural integrity, which involves the use of multidisciplinary fields, including sensors, materials, signal processing etc. The method was invented especially aimed at the integrity of critical composite part in aircraft. In military and civil aircraft, the use of advanced composite materials is increasing rapidly, because they have considerable advantages

over traditional metals in terms of high specific strength and stiffness. However, composite structures are vulnerable to low-speed impact or fatigue damage, which may result in serious underground damage (matrix cracks, delamination and fiber breakage), which is difficult to detect from the outside. Therefore, low-speed impact damage resistance and damage tolerance are the main detection items in aircraft certification process. Traditional aircraft structural integrity inspection requires downtime and non-destructive methods, such as ultrasonic imaging or X-ray photography, which is very labor-intensive and prone to human errors, leading to serious consequences. A fast in-situ diagnosis/prognosis of the integrity of in-service structures on a continual real-time basis was naturally a goal for the end users and manufacturers ².

With the help of SHM, people can identify a problem early in a structure's lifespan. Structures were evaluated from the most basic level of damage presence, up to damage location, damage nature, damage extent, and finally to entire structural prognosis. It can also greatly reduce the cost and time of repairing related components and prevent potential catastrophic failures and loss of life, especially for major and key structures. As shown in Figure 1.1, a typical structural health monitoring system consists of three main parts: sensor network, integrated hardware and related software. When the system starts to work, the piezoelectric components can generate guided waves in the structure, and then these signals are recorded by adjacent piezoelectric sensors in the actuator/sensor network. The diagnostic system indicates that the piezoelectric actuator generates a pre-selected diagnostic signal and transmits it to the adjacent sensors. The response of these sensors can then interpret the changes occurring in the structure according to the location and size of the damage or the change of material characteristics. The method used in the diagnosis process is based on comparing the current sensor response with the previously recorded signal. The difference between the two sets of signals contains rich information about structural changes. In SHM system, the sensor provides an electrical or optical response to external stimuli, and the response is reversible when the stimulus disappears.

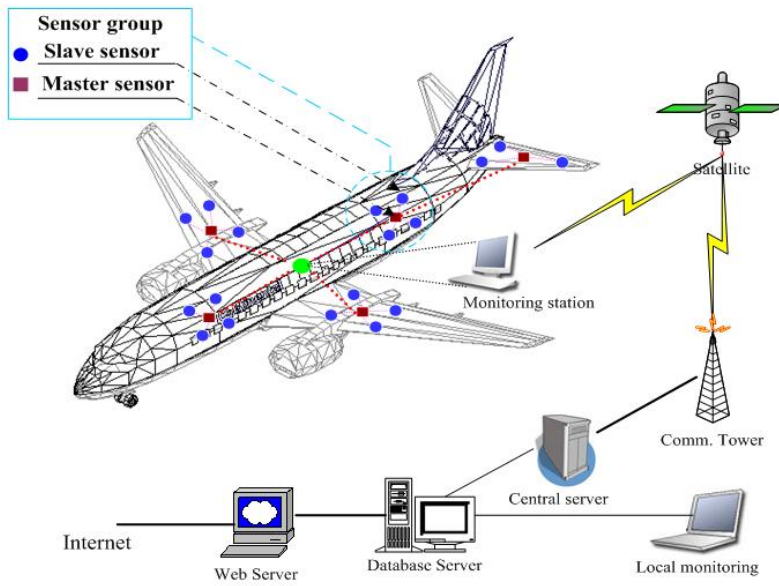


Figure 1.1 A typical SHM system in aircraft.

At present, there are two typical structural health monitoring methods: (a) passive SHM; and (b) active SHM. Passive SHM infers structural health mainly by measuring various operating parameters. For example, flight parameters (airspeed, air turbulence, vibration level, etc.) can be monitored, and then specific algorithms can be used to infer how long the aircraft will last and how much is expected to remain. Passive SHM is useful, but it does not directly check whether the structure is damaged. On the contrary, active SHM can directly assess structural health by detecting the presence and extent of structural damage. In this regard, the active SHM approach is similar to the approach adopted by non-destructive assessment, but it is a step forward: it attempts to develop permanently mountable structures and monitoring methods to provide critical structural integrity analysis.

In general, it is not feasible to permanently install traditional NDE sensors in structure, especially in applications with high weight and cost, such as aeronautics and astronautics. However, for piezoelectric sensors, the situation is different. They are small, light and cheap. They can be made into different geometric shapes and embedded in different structures. They can be glued to the surface of the structure, or installed inside the object, or even embedded between the structural layer and the non-structural layer to form a complete functional layer.³ Therefore, by embedding this smart device into the structure, SHM technology can help aircraft transit from

plan-based maintenance practice to condition-based maintenance. The goal is to improve maintenance agility, improve aircraft availability, shorten turnaround time, and reduce costs throughout the life cycle.

There are still some issues for embedding these smart sensors/actuators into the structures: Because of the large dimension, and the rigidity, the mounted PZT sensor will produce the non-uniformity, which will lead to the stress concentration. Thus, the new damage could originate from this stress concentration. In addition, sometimes the explosion of sensor to the environment can result in the age of the sensors, which could reduce their sensitivity. Otherwise, the adhesion of the sensor is subject to varied influence, including the temperature, stress, vibrations etc... Which could make the connection of sensor to be fragile and reduce its reliability. To address this problem, the smart layers are developed in recent years. Firstly, the sensors are made from the flexible polymer materials to increase its adaptability and reduce the stress concentration. Secondly, the dimension of smart layers is usually very small (less than 1/10 of the structure dimension). Thirdly, the sensors and traces are packaged within the composite prepreg, to prevent the age and disconnection.

1.2. Embedded smart composite structures

Since large aerospace structures had critical high-stress or flight-critical areas that brought chronic structural problems, the architecture developed for a SHMS required a dense network of sensors to monitor the incipient damage in these problem areas. The problem areas also included those hard to inspect and maintain without extensive disassembly of the surrounding structure. Therefore, the hardware of SHM system was composed of a distributed sensor network. These sensors were embedded into the structure and can collect information and sent it to the electronic monitoring device. At present, PZT piezoelectric sensor and fiber Bragg grating (FBG) are the most commonly used sensing units in composite structures. To perform in-situ diagnosis, these sensors needed to be permanently embedded and installed in the critical sites of the structure^{1,4}. The problems were usually produced during the attachment process. For example, PZT sensors

was currently the most widely used piezoelectric wafer. Because of its large dimension, and the rigidness, the mounted PZT sensor will produce the non-uniformity, which will lead to the stress concentration. Thus, the new damage could originate from this stress concentration. In addition, sometimes the explosion of sensor to the environment can result in the age of the sensors, which could reduce their sensitivity. Otherwise, the adhesion of the sensor was subject to varied influence, including the temperature, stress, vibrations etc... Which could make the connection of sensor to be fragile and reduce its reliability. To address this problem, the smart layers were developed in recent years. Firstly, the sensors are made from the flexible polymer materials to increase its adaptability and reduce the stress concentration. Secondly, the dimension of smart layers is usually very small (less than 1/10 of the structure dimension). Thirdly, the sensors and traces are packaged within the composite prepreg, to prevent the age and disconnection.

1.2.1. The basic concept of smart composite structures

In sensor system, one of the most important technologies is the embedding and integration of sensors in the structure. Sensors permanently embedded in composite structures can provide all-weather monitoring capabilities. A large number of sensors supported on a thin flexible dielectric film called SMART layer provide a simple and effective way to integrate large sensor networks into complex three-dimensional structures, and show great potential⁵. Sensor networks permanently embedded in composite structures can be used not only for active sensing but also for passive sensing to monitor the health of structures in a full life cycle. As shown in Figure 1.2⁵, sensor network layer can usually be integrated into composite structure and installed on the existing structure during manufacturing or surface, thus providing built-in health detection for the internal and external states of the structure. The advantage of the sensor network method is that the micro piezoelectric sensor network provides a wide area coverage for data acquisition, so as to detect as many impacts and damages as possible, to facilitate the use and ensure the consistency of information.

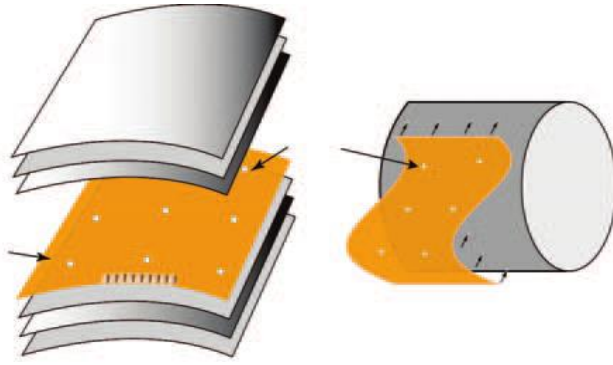


Figure 1.2 A schematic of piezoelectric sensor network integrated within the composite structure ⁵.

Smart structures and materials can bring significant performance improvements in various applications. In recent years, the revolutionary development of information technology and material science and engineering has further promoted the development of reliability and efficiency of intelligent structures and systems. ⁶In fact, the terms of multi-functional structure, intelligent structure, adaptive structure, active structure and so on all belong to the same research concept ⁷. Since 1979-1980, NASA Langley Space Center first used embedded optical fiber sensors to measure strain in composite materials, researchers have made extensive research on embedded smart structures.

Traditional smart composite structures are generated by embedding heterogeneous components such as foil sensors, optical fibers and bulky connectors. This kind of implanted material often does not match the matrix material, which can easily lead to stress concentration and even induce microcracks. Mechanical properties of composites, especially interlaminar shear strength (ILSS), may also be damaged to varying degrees ¹. Advanced smart structure adopts system integration, realizes higher efficiency, reduces volume and weight, and saves cost. It is superior to traditional circuit board and other components⁶. Several papers were found in literature^{8,9} dealing with electronic assemblies and other smart components integrated with composite structures. The most common method to implement intelligent systems is to embed functional elements in composite structures or attach functional elements to structures. Functional elements refer to sensors and actuators, as shown in Figure 1.3. Embedding methods usually use optical fibers, piezoelectric ceramics and polymers. Attachment and installation usually belong to controllers, including shape memory alloy (SMA), piezoelectric and electrostrictive ceramics,

electrorheological fluids, elastomers etc¹⁰.

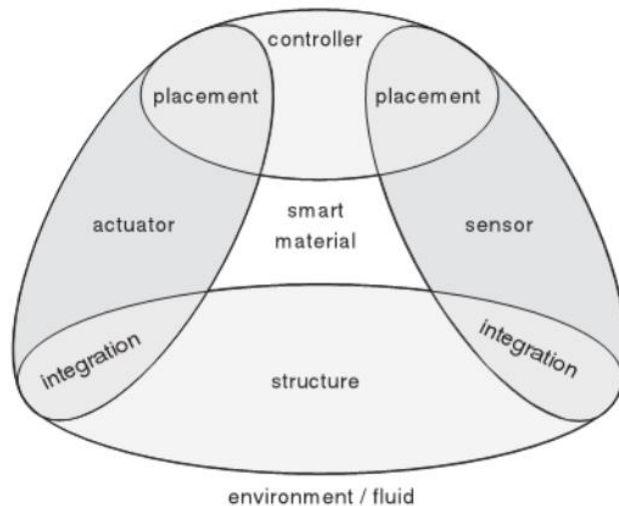


Figure 1.3 The intelligent system and its relationship with the smart materials and composite structures ¹¹.

1.2.2. The effects of embedded sensor/actuator on the integrity of the structures

As mentioned earlier, multifunctional composites can save volume and weight by combining functional components with reinforcing materials, but we also discussed that embedded components can affect the integrity of composite structures to some extent and may damage the mechanical properties of composites¹². At present, composite structures are mainly used in aerospace, marine and military applications. These platforms cannot afford too much extra weight or volume. In addition, the reduction of mechanical integrity of composite structures by intelligent systems must be taken into consideration. Therefore, the goal of intelligent composites is to create multiple functions without affecting the original properties of composites. In order to achieve this goal, the new generation of smart composite materials should become an organic whole, just like the human body. It integrates functional objects into intrinsic parts of the structure, which are no longer regarded as heterogeneous structures, so that their impact on structural integrity is minimized.

Direct embedment of sensors into the composites to form smart structures faced many limitations regarding structure integrity. Most developed sensors (e.g. temperature and strain sensors, fiber optics) required significant additional expenditures with respect to embedding, cabling and signaling, which possibly outweigh any benefits. Many of commercial sensors had their thickness like or larger than that of a few composite layers. The poor interlaminar bonding between sensors and laminates destroys the mechanical integrity to a great extent. These sensors are considered as intrusive inclusions in composite structures. Therefore, simply embedding sensors in composite laminates will lead to non-flat and non-uniform structure. In the use process, the non-uniform combination of sensor and matrix will be the dangerous area of stress concentration, which will significantly reduce the strength of the structure. In most cases, this risk is difficult to control. Especially in aerospace and military applications, we cannot accept such risks. In addition, the current intelligent structure integration technology has not found a reliable way to place sensors and their precise patterns in thick and complex geometric composite structures.

Currently, optical fibers are most widely used in sensing and health monitoring composite structures. Through a series of static and cyclic fatigue load tests, Li et. al¹² tested the mechanical properties of the composites when embedded in optical fibers. He observed that the fatigue life of the composite structure decreased significantly at this time. Especially in the interlayer position, it shows very low fatigue resistance, as shown in Figure 1.4. The decrease of mechanical properties of optical fiber embedded composites is mainly due to the poor interfacial bonding between the matrix and the optical fiber. Because the diameter of the optical fiber is about several hundred microns, and the diameter of the single optical fiber is 10 microns. Therefore, the larger size of optical fibers can produce resin-rich regions, which eventually lead to stress concentration in composite materials.

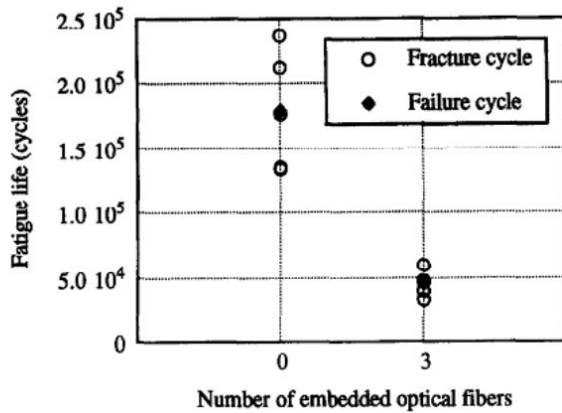


Figure 1.4 The influence of optical fibers on the fatigue lives for the embedded composite material¹².

Piezoelectric thin film structure is another widely used embedded component, such as PVDF sensor, PZT and so on. Piezoelectric thin film structures can bring various functions to structures, but interlaminar bonding is still a major problem¹³. As shown in Figure 1.5, when copper foil was embedded in the matrix structure, serious delamination will occur. The strain and static mechanical properties of glass fiber-vinyl ester composites containing interlaminar copper foil in tension, compression and bending were related to blade size and copper surface treatment. Its compressive properties were strongly influenced by the size of the insert and its bonding strength to the polymer in the composite. Compression performance decreased significantly with the increase of copper foil size (up to 20% and 6-8). The poor adhesion between copper surface and composite materials led to debonding, delamination and subsequent buckling failure in the samples.¹⁴.

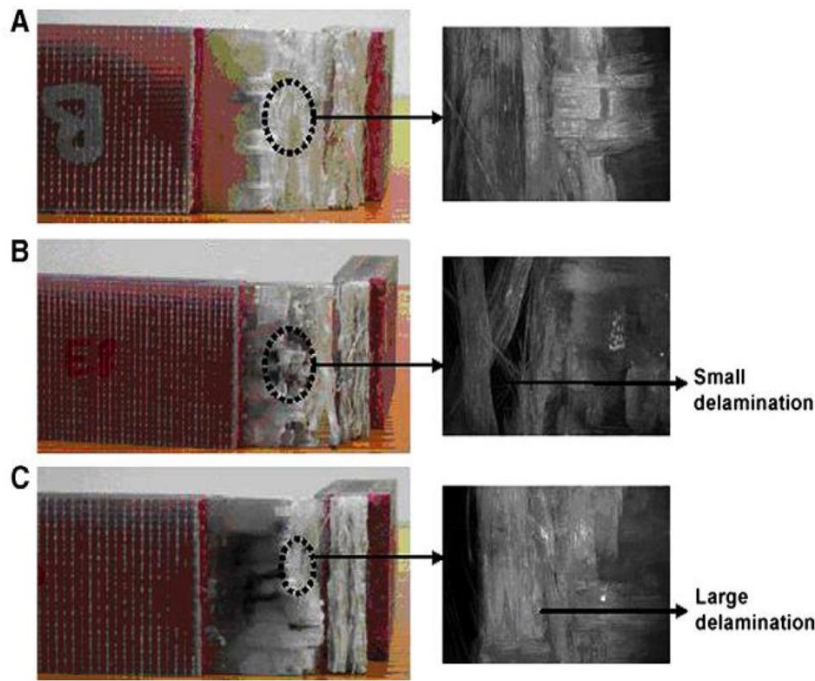


Figure 1.5 The influence of embedded Copper foil on the compression properties of the structure: (A) baseline, (B) Copper-AS with 57.1% area ratio and (C) Copper-T with 57.1% area ratio¹⁴.

1.2.3. The fabrication methods for the embedded smart composite structures

At present, the intelligent layer can be embedded in composite structures by two different methods: (1) the performance of dry fibers: this method is usually achieved by implanting fibers. In the implantation process, optical fiber¹⁵ and copper wire¹⁶ can be made into dry fiber prefabricated parts, and then through 3D braiding or braiding technology, it can become sensors and antennas; (2) Laminating process: In this process, the embedded functional components are cured together with the matrix during the pressing process, and the integrated structure¹⁷ is established. The second method is relatively easy; however, structural integrity, especially interlaminar shear strength, will be destroyed during preparation and may lead to structural delamination. In addition, the embedded object can act as a blocker in the process of resin injection, adding to the homogeneity in the matrix¹⁸. The first method has little effect on the structural integrity, but the size of the integrated elements is at least several dozen times larger than that of a single fiber, which results in a resin-rich area of¹⁹, resulting in a stress concentration of¹². In addition, because the processing is based on braiding or manual insertion,

it will inevitably lead to a reduction in efficiency and accuracy. Detailed descriptions of each method are as follows:

Dry Fiber Performs: Dry fibers are usually made of yarns or rovings, which are then assembled into two-dimensional sheets or three-dimensional multi-layer structures. In this way, several two-dimensional layers are cut into desired shapes and assembled into prefabricated parts. Smart materials such as sensors and actuators can be placed between layers. Glisic and Inaudi²⁰ developed sensing bands by clamping optical fibers between two thermoplastic films. The sensor tape can be placed between layers in any preferred direction and in the stack of layers. The University of Manchester has developed an interlaced scanning technology that incorporates sensing components directly into woven fabrics to improve interlaminar strength. As shown in Figure 1.6 (a)²¹, the PVDF bars are co-woven and fixed on the loom. Because the sensing strip is locked in position and covered with reinforcing fibers, the interlaminar strength is significantly improved compared with the traditional method of placing sensors between layers. As shown in Fig. 1.6 (b), the fabric structure is mounted on a cantilever beam and the frequency response function of the beam is measured by an embedded PVDF film and a laser probe focusing on the free end of the cantilever (Fig. 1.6 (b)).

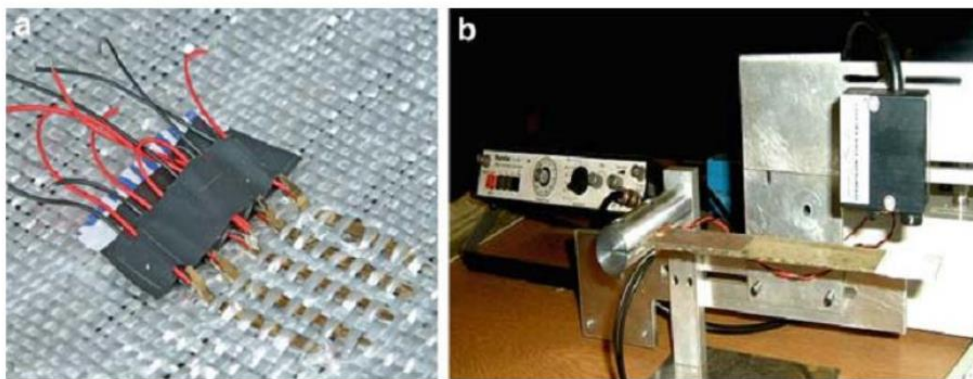


Figure 1.6 (a) Integration of PVDF sensors into 2D fabrics using dry fiber performs, (b) frequency response test by the cantilever beam with built-in PVDF 2D fabrics sensor²¹.

Lamination process (SMART Layer): This is a new design and related manufacturing technology that integrates piezoelectric sensor networks into composite structures. Strictly speaking, only when this method is used, can we call embedded intelligent structure intelligent layer. Lin and hang²² describe the manufacturing and initial validation test of the (SMART) layer prototype (Fig. 1.7). In order to realize this concept, a thin flexible dielectric film, including a series of interconnected piezoelectric actuators and sensors, needs to be produced by using printed circuit technology. In this intelligent system, sensors are embedded in traditional composite laminates. The results show that the mechanical properties of carbon/epoxy composite laminates containing SMART layer prepared by curing cycle have not been significantly reduced.

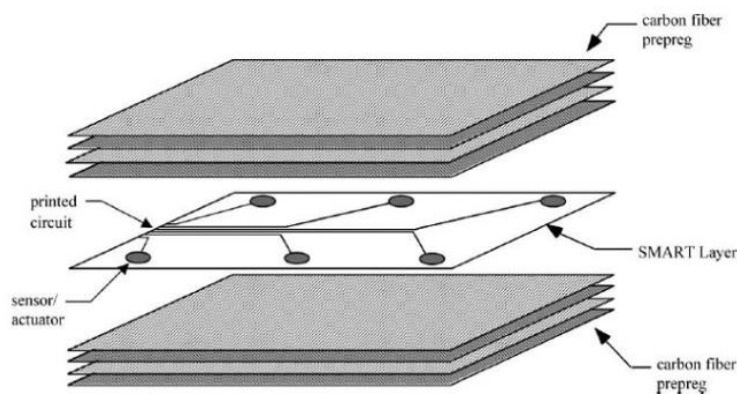


Figure 1.7 The concept and structure of SMART layer which include the integrated sensor/actuator network in a composite laminate²².

In order to combine sensor networks with different geometric structures, Qing et.al⁵ established a three-dimensional (3D) intelligent layer. The results showed that many sensors supporting thin flexible dielectric film can support such a simple and effective method: as shown in Figure 1.8, smart layer and laminate were shared by resin transfer molding (RTM) process, and large sensor networks were integrated into complex three-dimensional structures.

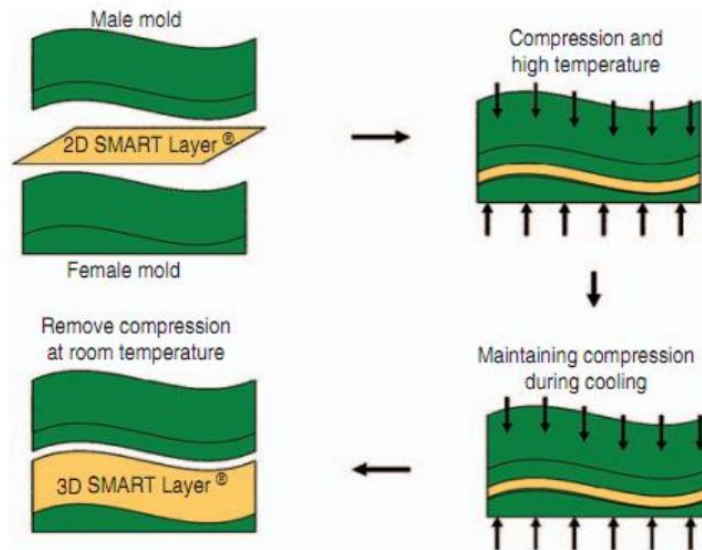


Figure 1.8 A simple 2D to 3D conversion process of a smart layer ⁵.

Acellent Technologies, inc. is currently the first company to develop smart layer manufacturing technologies of various sizes, shapes and complexities. Figure 1.9 ²³ showed examples of SMART layers of various shapes produced by Acellent, inc. The provided SMART layers varied in size from inches to feet. The complexity of SMART layer varied from a simple 2-sensor flat strip to a complex 30-sensor three-dimensional shell. They can be manufactured in different shapes to integrate different structural contours. The basic shapes include rectangular, slender strip, circular and three-dimensional shells.

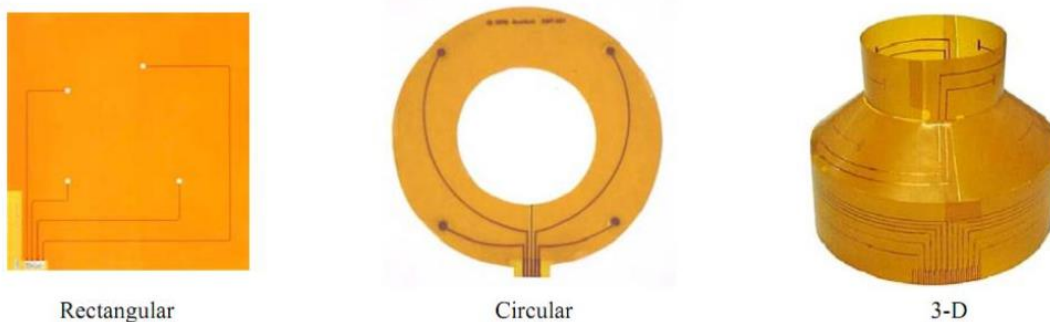


Figure 1.9 Examples of SMART Layers in basic shapes produced by Acellent, inc. ²³.

1.3. Additive manufacturing (AM) technology

The state-of-art SMART Layer had built-in sensors in a thin dielectric film. However, its thickness was still much larger than that of the composite laminates, which made it difficult to be embedded in composite structures, and mostly mounted on the structural surface. It impelled people to look for better methods to address this problem. Additive manufacturing (AM) technique, showed a huge potential for realizing the smart structure by seamlessly integrating multi-functionalities directly into the structure. Using AM, the fabrication of the structure and the sensors can be flexibly tailored and seamlessly integrated. AM process is flexible and highly accurate, because computers are an important part of the process. Even in the very advanced manufacturing field, AM has brought about changes because of its unique low-cost advantages. For example, it is a very time-consuming and expensive process to use traditional lithographic printing technology to manufacture sub-micron electronic circuits. In the future, AM technology, which combines thermal spraying, laser transmission and other technologies, will even bring new breakthroughs in the high-end field of integrated circuits.

The widely used composite materials in aerospace industry were thermoplastic polymer matrix with reinforcing fibers. And These composite polymers can be produced by phase change printing layer-by-layer, while the sensing systems including the piezoelectric materials for the sensor element and electrical interconnects can be printed onto the surface of any desired locations and layers. Without a doubt, the time when we can directly print the end use products (eg. smart phones, fuel cells, engines...), is approaching.

1.3.1. Basic definition and development history of AM technology

Additive Manufacturing (AM) is one of the most discussed emerging technologies in the industry and has potential revolutionary power. After about 30 years of manufacturing, it is about to change from industrial rapid prototyping technology to the mainstream manufacturing process used by industry and consumers. In essence, AM technology is a method of converting three-dimensional computer aided design (CAD) documents into useful physical objects. It uses sequential applications of materials and energy (such as light, ultrasonic vibration, laser or

electron beam) to bond or connect materials in varied methods. These bonds vary in strength and type depending on the technology and materials used to create the final components. It is a key step for process reliability and quality control to evaluate these bonds as a function of process parameters and materials. The major milestones of research development in this industry were list as below²⁴:

Table 1.1 3D printing chronology and milestones²⁴.

Year	Event
1991	Stratasys produces the first FDM 3D printer.
1992	The first 3D printer based on stereolithography is produced by 3D Systems.
1992	DTM produces the first selective laser sintering machine
1999	A group of researchers of the Wake Forest Institute for Regenerative Medicine use 3D printing technology to create scaffolds from living cells.
2000	Object geometries produces the first 3D inkjet printer.
2000	Z Corp produces the first multicolor 3D printer.
2001	Solidimension produces the first desktop 3D printer.
2005	Dr Adrian Bowyer founds the RepRap project at the University of Bath based on open-source collaboration.
2006	The first SLS machine becomes viable and opens the door for mass customization.
2008	The RepRap Darwin printer is released as the first self-replicating 3D printer that can produce most of its own components.
2008	Stratasys produces the first biocompatible FDM material.
2008	Shapeways launches the first 3D printing online market place.
2008	MakerBot launches Thingiverse as another file sharing platform.
2008	The first 3D printed prosthetic leg including all relevant joints is produced.
2009	The bioprinting company Organovo produces the first 3D printed blood vessel.
2011	Kor Ecologic unveils the first 3D-printed car called Urbcc that consists of a fully 3D printed body.
2011	iMaterialise becomes the first 3D printing service that offers gold and silver as printing materials.
2012	The Dutch company LayerWise produces the first customized 3D-printed prosthetic lower jaw.

In AM, materials are added layer by layer to create the final geometry, thus realizing complex internal features, such as embedding of fibers and sensors. The integration of these internal

structures and the high dynamic characteristics of these processes will lead to residual stress and dimensional warpage, and lead to failure in manufacturing or premature failure in use. This requires the assessment of residual stress and dimensional warpage as a function of process parameters, materials and geometry. In addition, the surface finish and geometric accuracy of parts manufactured by AM are not necessarily sufficient for precision applications, so post-processing operations are often required.

With the development of AM technology, more and more kinds of ink materials have been developed and applied in recent years. Among them, polymer ink is the earliest and most widely used material. In general, the plastic filaments used in desktop 3D printers can be divided into two categories: thermoplastic and thermosetting polymers. The difference between the two ink materials is that the thermoplastic melts when heated, but does not change its internal composition, so it can be melted and remelted many times. In contrast, thermosetting polymers change their internal composition once heated; this means they cannot melt back into reusable liquid forms.

Metals was also widely used material as ink material. There are many kinds of metals that can be printed in 3D, and they are still growing. At present, the hot research fields include tool steel, stainless steel, titanium, titanium alloy, aluminum casting alloy, nickel-based alloy, gold and silver, which have been successfully used in AM manufacturing. Especially in recent years, more and more materials have been developed as ink materials of AM technology. Some of these materials may even break our traditional definition of materials. In addition, a trend of material development is the emergence of digital materials. Digital material is a composite material sprayed by two different materials at the same time. The resulting materials can simulate the properties of various advanced materials, including the toughness and temperature resistance of Engineering plastics. The flexibility and accuracy of AM technology are also considered as potential technologies for manufacturing specific advanced materials, especially advanced materials that require precise control of composition and structure, such as supermaterials and high-entropy alloys.

From the above introduction, AM is not a single technology, in fact it is a general term of a lot of

processing methods. One common place of all AM technology is that the physical procedure of forming is completed on the surface of printed material. Different types of methods applied different kind of energy to bind the ink material to form the bulk layer by layer. Because the ink/or energy flow is controlled by the needle tip, and motion of tip can be accurately controlled by the computer, which could bring a great accuracy and freedom for the processing of materials. Because of those characteristics of AM technology, more and more materials are produced by AM.

1.3.2. Application of AM technology in sensors and other electronic devices

Various traditional printing methods (such as screen printing) produce sensors, which have the advantages of small size, low price, easy development and manufacture. These sensors include biosensors and gas, temperature, position, humidity and light sensors, but the traditional method has a great limitation that only two-dimensional (2D) and planar structures can be manufactured²⁵. Now, with the emergence of AM technology, more and more groups are studying its potential as a means of manufacturing sensors. Many different kinds of AM technology have been successfully applied to the manufacture of sensors. Many of the printed sensors show good performance, and some have very unique characteristics. A key advantage of manufacturing sensors with AM is that the limitations of traditional manufacturing techniques can be overcome by creating complex shapes from various sensing materials. Therefore, this method also makes it one of the most promising methods for the experimental study of topology optimization²⁶.

The main difference between AM technology and traditional methods is that AM can produce very small and complex shapes, and it is possible to produce printed electronic devices²⁷ at medium, micro or nano scales. Therefore, with the further development in the future, AM process is very likely to replace mask lithography process²⁸ in electronic products. All these AM technologies have roughly the same goals; however, the approaches to achieving this major design goal vary widely. For example, Extrusion technology extrudes fluid materials through a small nozzle and extrudes them onto the substrate. Direct Writing technology injects droplets of material directly into the substrate. The Aerosol Injection system atomizes a material to form a gas flow, which is aerodynamically concentrated and deposited on the substrate. Laser-based

systems use laser energy to transfer materials to the substrate surface.

The commonly used AM technology is mainly used to manufacture specific materials with relatively simple properties. Until recently, researchers began to develop more complex printing materials and apply them to more complex systems, including (1) implanting components (sensors, batteries, etc.) into specific cavities in manufacturing structures, (2) developing different materials for specific functions (thermal conductivity and conductivity, radiation shielding, optics, flame retardant, etc.), (3) embedding them in polymer substrates by ultrasound or ultrasound. Solid conductor to provide high performance electrical interconnection. Together, these technologies enable us to automate the production of complex multi-functional electronic and electromechanical systems ²⁴.

Therefore, as a fabrication method of sensors, AM is still in a very primitive stage, and its potential is just beginning to be demonstrated. Although reported applications were in limited area, this technology has demonstrated the ability to manufacture products that are difficult to obtain by other methods. Not limited to sensors, many new applications of mechanical electronics will use AM technology to make devices with unique and complex geometries - such as wearable mobile phones, or special chips that can be implanted into human tissues. With the improvement of process control, and the interpenetration of AM technology with material science and computer science, these complex preparation processes can ultimately be purchased and downloaded from the Internet and then produced, just like customized mobile phones. The profound transformation of manufacturing mode from remote factory to local 3D printing will not only reduce transportation costs, but also realize new functions of unit-level customization, which will eventually lead to profound changes in the whole manufacturing industry towards intelligent manufacturing.

In recent years, AM technique provided a promising solution for the integration of the composite structures and the embedded sensor systems. The three-dimensional solid objects were fabricated by laying down successive layers of functional materials from digital models, until the final structure was produced. Using AM approach, the fabrication of the structure and the sensing systems can be flexibly and seamlessly integrated together. The most state-of-art composite

materials in aerospace industry were thermoplastic polymer matrix (epoxy resin) with reinforcing fibers. The composite matrix structures can be produced by thermal extrusion deposition method, such as phase change 3D printing and fusing deposition modeling. During the manufacturing of the composite matrix structures, sensing systems including the smart materials for the sensors and electrical interconnects can be printed in demand at the desire locations. The resin structures with embedded sensors and interconnects can be used as the prepregs and readily plugged in the in-service composite structure for in-situ sensing²⁵.

There may be a question like this: why we need the sensor network that will be all printed. In order to answer this question, people just need to consider our body. The SHM technology is just like the nervous system in our human body. The sensor is like the nerve ending to detect any stimulus of the environment or damages in our body. When our body is subject to any disease or damages, the nerve ending can detect the change. It can also transfer this stimulus into electrical signal just like what happen in the sensors. And then nervous fiber delivers those signals to brain to collect, process, and analyze the signal which correspond to the computer. At last our brain make the final decision and do the response just like what the SHM software to treat those data. Thus, it is reasonable to deduce that the best integrate technology is just like human body: the nervous system is not integrated with any foreign component from outside. All those nerve endings, and nervous fibers are grown as parts of our body. As the development of 3d printing technology. More and more regular structural material can be directly produced by AM with high accuracy and controlling. So why not think about growing sensor system in the printing process of those structural materials and at the same time make them smart? Thus, the concept of all-printed sensor not only indicate the fabrication of every component of sensor by printing. It can also include the integrating of this smart layers during the processing of the whole structure in printing process.

1.4. Introduction to polyvinylidene fluoride (PVDF)

It was introduced previously the concept of all-printed smart layers, and the promising method to

realize this concept. The smart layer with built-in piezoelectric actuators and sensor networks can be used to monitor the structure status and detect damage during the use of the structure. The advantages of using smart layer include easy installation, signal consistency, sensor reliability and high signal-to-noise ratio. The materials selected for manufacturing intelligent layers need to meet the following requirements: (1) small thickness to avoid affecting the integrity of the structure; (2) easy operation and processing of materials; (3) good compatibility between materials and matrix parts is easy to use in the composite manufacturing process; (4) good sensitivity; (5) durability. So, what is the ideal choice of core functional materials used in sensors, and how to develop printing, processing and integration technology of this sensor material?

There is no doubt that we will all witness the date when everything in our daily life be connected by the sensor network to form the internet of things. At that time, the smart layers and sensors will really play a critical role in this world. And Polyvinylidene fluoride (PVDF) is considered as the most promising sensor material in the future all-printed smart material and structure. Firstly, PVDF is not only piezoelectric, it also has excellent pyroelectric, flexoelectric, dielectric, electrostrictive properties. Thus, if properly processed and integrated, PVDF smart layers can meet the requirement in varied applications. The PVDF film and fibers are very flexible, it can be compatible with every kinds of matrix materials. This characterize will prevent the embedded layer to impair the integrity and mechanical property of the structure. Of course, the sensitivity the most important consideration for our sensor material. PVDF is one of the best piezoelectric polymers, it is also the most widely used piezopolymers. It also has a low acoustic impedance which can largely broaden its application. At last, since the sensor material in smart layer would become indispensable in our daily life. So, it should be fitful for massive production. Thus, the economic and health consideration is becoming more and more important. In this study, although PVDF copolymer is much easier to process, we still chose PVDF because of the much lower price. To replace PZT with non-lead piezoelectric is a progress, but it is not enough. In order to make our product really environment-friendly. We need to prevent the pollution during the whole process, which include reducing the usage of toxic organic solvent. We also have done some effort in this respect. Some of its more important properties were listed as below²⁹⁻³¹:

- High rigidity, resists deformation

- Low glass transition temperature (no transitions between -45° and 170° C)
- Wide range of processing temperatures (185° - 250° C)
- Resistance to heat and combustion
- Resistance to ageing
- Resistance to abrasion
- Chemically inert.
- Non-toxic
- Chemically resistant (highly polar solvents will cause slight swelling)
- Stability to radiation (UV, X-ray, Gamma)
- Excellent electrical insulator
- High Curie point (103° C, valuable for high temp piezoelectric applications)

1.4.1. The basics of piezoelectricity and ferroelectricity

Smart materials have one or more properties that can change in response to external stimuli such as heat, electric or magnetic field, stress, light and pH. They are commonly categorized into several classes based on the type of driving input and its corresponding response: piezoelectric, electrostrictive, electroactive, magnetostrictive, electrorheological and magnetorheological, shape memory, ferromagnetic shape memory, pH sensitive, temperature responsive and chromogenic. In general, all of these smart materials are essentially transducers and thus the applications based on smart materials can be classified into two fundamental behaviors: sensing and actuation.

Among these smart materials, ferroelectric materials contain a class of smart materials that generate spontaneous polarization. If this spontaneous polarization can be reversed by an external (sufficiently high) electric field, the crystal is called ferroelectricity. In homogeneous non-linear dielectrics, the evolution of spontaneous polarization and ferroelectricity is caused by the spontaneous displacement of atoms relative to each other at a certain temperature, resulting in permanent dipole moments. The density of this dipole moment is called polarization (P), which is a vector. The direction of this vector, in turn, is determined by the pole group, which is formed after the quasi-electric phase transition. Above a certain temperature T_c (usually called

Curie point), spontaneous polarization disappears and ferroelectric crystals are transformed into quasi-electric state ³².

Another important material in technology is piezoelectric material. Piezoelectricity is defined as the ability of certain materials to generate charges due to mechanical deformation. In general, piezoelectric materials consist of randomly oriented grains (grains) separated from each other by grain boundaries. The working principle of piezoelectric materials is charge separation, in which the basic crystal structure of piezoelectric materials is asymmetric. According to the definition of piezoelectric effect, all components of piezoelectric tensors should be cancelled out in crystals with symmetrical centers. The piezoelectric properties of crystals are produced by the structure of their atomic arrangement. As shown in Figure 1.10 ³², only 21 of the 32 crystallographic point groups are non-centrosymmetric. In the central symmetric structure, piezoelectricity is eliminated. Similarly, in point group 432, the combination of symmetric elements eliminates piezoelectricity. The other 20 point groups have potential piezoelectric properties. Ten of these 20 point groups are polar, that is to say, they have a vector direction on materials that are asymmetric with other directions. Such materials can be spontaneously polarized, and the polarization vector is usually a function of temperature. Therefore, these materials are pyroelectric. Ferroelectrics are a subset of pyroelectric materials in which spontaneous polarization produces a rearrangement through an applied electric field. In summary, all ferroelectric materials are piezoelectric and thermoelectric. Although symmetry does not necessarily reflect the piezoelectric properties of materials.

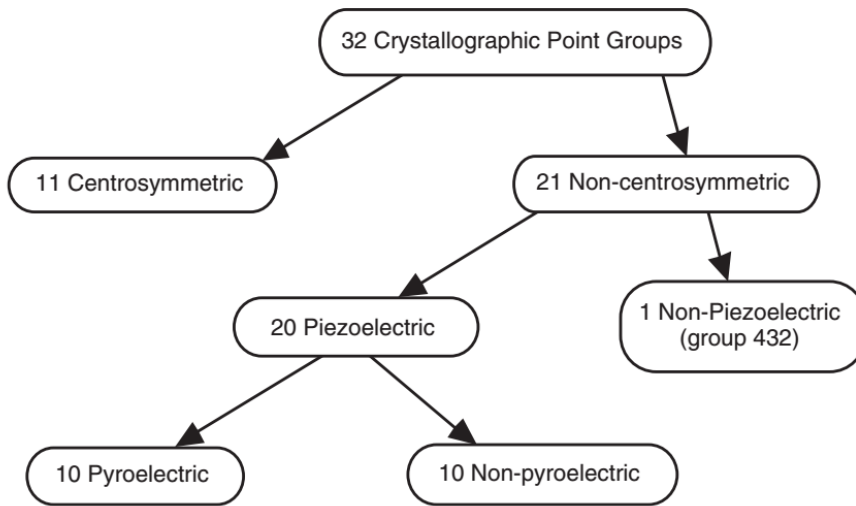


Figure 1.10 The relationship between Piezoelectricity and Crystallographic structure³².

Table 1.2 lists the point groups that permit piezoelectricity for all crystallographic systems ³².

Table 1.2 Centrosymmetric in crystals with different symmetries

Crystal system	Symmetry elements	Centro-symmetric	Noncentro-symmetric
Triclinic	Center	$\bar{1}$	1
Monoclinic	Center, axis, plane	$2/m$	2, m
Orthorhombic	Center, axis, plane	mmm	222, $mm2$
Tetragonal	Center, axis, plane	$4/m, 4/mmm$	4, $\bar{4}, 422, 4mm, \bar{4}2m$
Trigonal	Center, axis, plane	$\bar{3}, \bar{3}m$	3, 32, $3m$
Hexagonal	Center, axis, plane	$6/m, 6/mmm$	6, $\bar{6}, 622, 6mm, \bar{6}m2$
Cubic	Center, axis, plane	$m\bar{3}, m\bar{3}m$	23, $\bar{4}3m, 432$

The general piezoelectric effect is called direct effect. This means that when a force is applied to the surface of the crystal, a voltage will be generated between the surface of the crystal. In addition, there is an inverse piezoelectric effect. This means that when applied voltage to a piezoelectric crystal, the shape of the crystal will change. The details of the positive piezoelectric effect and the inverse piezoelectric effect are as follows:

Direct effect:

$$D = dT + \epsilon E$$

Converse Effect:

$$X = sT + dE$$

Where

E: Electric field

T: Stress

E: Permittivity of the material

X: strain

s: compliance

D: charge density

d: piezoelectric constant

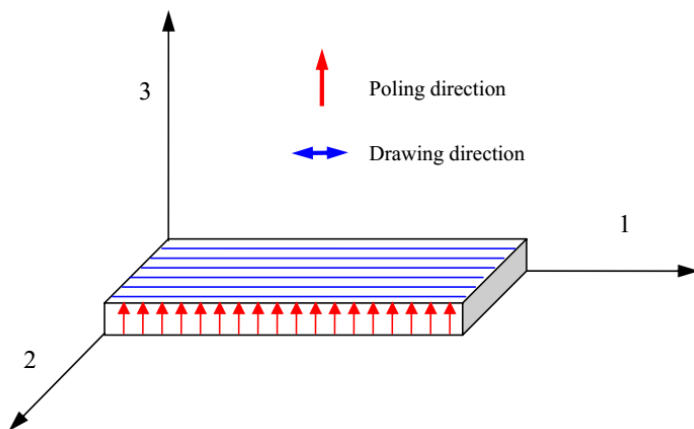


Figure 1.11 Tensor directions for constitutive relation definitions³³.

As shown in Figure 1.13, the direction of mechanical stretching is marked as "1". The "2" axis is the transverse direction on the working plane. The direction perpendicular to the surface is expressed as "3". The following labels "4", "5", "6" are shear plane that are perpendicular to the direction of "1", "2" and "3". Piezoelectricity can be described by four constants d_{ij} , e_{ij} , G_{ij} and h_{ij} . These constants are related to elastic coefficients (mechanical stress \mathbf{T} and strain \mathbf{S}) and dielectric coefficients (electric displacement \mathbf{D} and electric field \mathbf{E}). These relationships are defined by the following formulas: ³³

$$d_{ij} = \left(\frac{\partial D_i}{\partial T_j} \right)^E = \left(\frac{\partial S_i}{\partial E_j} \right)^T \quad (1.1)$$

$$e_{ij} = \left(\frac{\partial D_i}{\partial S_j} \right)^E = - \left(\frac{\partial T_i}{\partial E_j} \right)^S \quad (1.2)$$

$$g_{ij} = - \left(\frac{\partial E_i}{\partial T_j} \right)^D = \left(\frac{\partial S_i}{\partial D_j} \right)^T \quad (1.3)$$

$$h_{ij} = \left(\frac{\partial E_i}{\partial S_j} \right)^D = \left(\frac{\partial T_i}{\partial D_j} \right)^S \quad (1.4)$$

The first two equations (1.1, 1.2) correspond to the direct piezoelectric effect, while the last two (1.3, 1.4) refer to the inverse piezoelectric effect. The superscripts describe the experimental conditions: E denotes zero electric field (a closed circuit), D stands for zero electric induction (an open circuit), T corresponds to zero mechanical stress (a free sample), and S indicates zero strain (a fixed sample). The subscripts are $i = 1-3$ and $j = 1-6$. The above piezoelectric constants are related to each other through the elastic constant (c) and dielectric constant (ϵ), can be calculated as:

$$c = \frac{e}{d} = \frac{h}{g} \quad (1.5)$$

$$\epsilon \epsilon_0 = \frac{d}{g} = \frac{e}{h} \quad (1.6)$$

where, $\epsilon_0 = 8.854 \times 10^{-12}$ (F/m) is the permittivity of vacuum. The dielectric constant of piezoelectric materials also depends on the boundary conditions. The above dependence defines the electromechanical coupling coefficient k as:

$$\frac{\epsilon^S}{\epsilon^T} = \frac{c^E}{c^D} = 1 - k^2 \quad (1.7)$$

where k^2 , which is always less than 1, reflects the conversion efficiency between electrical energy and mechanical energy due to piezoelectricity.

$$k^2 = \frac{\text{electrical energy converted to mechanical energy}}{\text{input electrical energy}} \quad (1.8)$$

$$k^2 = \frac{\text{mechanical energy converted to electrical energy}}{\text{input mechanical energy}}$$

Different piezoelectric coefficients in different materials make them applicable in different fields. High voltage electrical strain coefficient enables these materials to be detected at a high sensitivity level or driven at a high power level. However, materials with high piezoelectric strain coefficients tend to have limited flexibility and coverage. The piezoelectric materials with higher flexibility are especially suitable for sensor³⁴. The key parameter of the sensor is g (piezoelectric stress constant), and the parameters of the piezoelectric polymer are usually higher than those of the piezoelectric ceramics³⁵. In addition, polymers can usually work at higher voltages than ceramics and have the ability to selectively polarize, which may be applicable to some special fields.

It should be pointed out that in non-ferroelectric ceramics, the piezoelectric effect of the whole sample is offset by the average effect of grain orientation at micro-scale. Therefore, at the macro level, polycrystals have symmetry and negligible piezoelectric properties. In contrast, ferroelectric materials can produce piezoelectric properties by polarization. This characteristic is due to the existence of so-called ferroelectric domains (regions with different spontaneous polarization directions) in sintered ferroelectric ceramics. The boundary between ferroelectric domains (usually called domain boundary) can be moved by an applied electric field to redirect spontaneous polarization in the crystallographic direction closest to the field direction. Because of this rotation process, the original macro-centrosymmetric structure lost its inversion center and became a piezoelectric structure. Many researchers have made great efforts to fabricate materials with piezoelectric properties. This goal can be achieved by using crystals close to the phase transition conditions, in which case the increase of dielectric constant will produce higher piezoelectric coefficients. The observation of the maximum piezoelectric response in PZT solid solutions of compositions close to the morphotropic phase boundary (MPB) provides a strong

support for this idea.

At last, we'll make a brief introduction on a nonlinear electromechanical phenomenon - the electrostrictive effect, which originates from the change in the dipole density in the material and occurs in all substances, whether crystalline or amorphous, solid or liquid. This effect not only play an important role in sensor/actuator application, it also interconnect with the piezoelectric performance of the material. The electrostrictive strain can be written as:

$$x_{ij} = Q_{ijkl} P_k P_l = M_{ijkl} E_k E_l \quad (i,j,k,l=1-3),$$

where Q_{ijkl} and M_{ijkl} are the charge- and field-related electrostrictive coefficient, respectively. It is also known that³²:

$$Q_{ijkl} = -\frac{1}{2} \frac{\partial(1/\epsilon_{ij})}{\partial X_{kl}}$$

That is to say, the electrostrictive coefficient reflects the change of dielectric constant caused by mechanical stress. It should be noted that most polymers exhibit non-linear dielectric behavior. Therefore, $x \sim E$ graphs do not exhibit quadratic relation. For electrostrictive polymers, if a DC bias field with small superimposed AC field is applied, obvious piezoelectric effect can be observed, as shown in Figure 1.13.

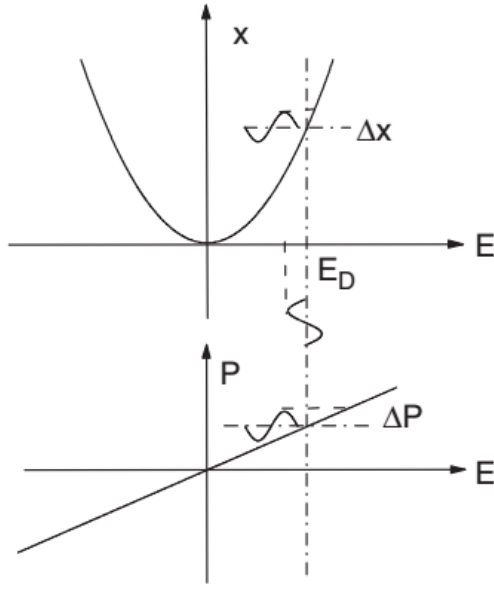


Figure 1.12 A schematic view of an electrostrictive polymer, with a small AC electric field superimposed on a dc bias field³²

1.4.2. The piezoelectricity of PVDF and its application in sensors/actuators

PVDF and its copolymer PVDF-TrFE films are usually used for SHM and damage detection as part of sensor and actuator networks. The piezoelectric effect of PVDF was first observed by Kawai in 1969. It has polymer properties that enable it to embed in complex structural surfaces and cover large areas. Generally, it has high mechanical resistance, size and temperature-related stability, high dielectric constant, chemical inertia, easy to handle, and relatively cheap³⁶. Using PVDF-TrFE copolymer, piezoelectric phase can be easily prepared without stretching³⁵. It also has higher residual polarization and requires lower stress field, which means it is easier to polarize and control. Unfortunately, the piezoelectric coefficient of TrFE copolymers is lower than that of PVDF, but the advantages mentioned above can usually compensate for this deficiency. So far, PVDF has been widely used in sensors and sensors because of its extraordinary piezoelectric characteristics. Some of its most important characteristics include high purity, weatherability and chemical resistance, light weight, mechanical strength and wear resistance. Its main advantages in these applications include high voltage sensitivity, flexibility,

toughness and manufacturability. Its advantages also include strong biocompatibility and its low acoustic impedance is close to water, so it is very useful for fluid sensors and biomedical applications. A complete list of commercial and research applications includes strain and strain rate measurements; potential active biomedical materials; switches, shock and vibration sensors, accelerometers; flow detectors; equipment in acoustic, ultrasonic and vibration control. However, the requirement of mechanical treatment and polarization hinders its further application. The material properties of PVDF films are shown in Table 1.3.

Table 1.3: Some material Properties of PVDF Film³⁷.

E	Young's Modulus	$2 - 4 \times 10^9 N/m^2$
d_{31}	Transverse Coefficient	$23 \times 10^{-12} \frac{C/m^2}{N/m^2}$
d_{33}	Compressive Coefficient	$-33 \times 10^{-12} \frac{C/m^2}{N/m^2}$
p	Pyroelectric Coefficient	$30 \times 10^{-6} \frac{C}{m^2K}$

The piezoelectric and dielectric properties of PVDF are similar to those of many piezoelectric ceramics. In terms of mechanical properties, polymer PVDF materials have significant advantages over piezoelectric ceramics. The small modulus of elasticity and extremely low mass of sensor materials have opened up many new applications. Compared with brittle piezoelectric ceramics, PVDF can combine mechanically and chemically with polymers and integrate them into fiber reinforced laminates. The intelligent layer with high flexibility can be obtained by simple gluing, so that it can be integrated into the structure of various applications. The temperature range of PVDF film as actuator or sensor is between -70°C and $+90^\circ\text{C}$. PVDF exhibits strong pyroelectric properties, which can not be ignored in application.

Typical values of the piezoelectric and pyroelectric coefficients, as well as of other physical properties, of materials that have been used as transducers are given in Table 1.4. The three-dimensional anisotropy of the piezoelectric effect is seen clearly for oriented PVDF. The d constant associated with the molecular direction (d_{31}) is an order of magnitude greater than that transverse to the polymer chains (d_{32}); both are positive because a stress in the film plane reduces

the specimen thickness, thus increasing the surface charge, whereas d_{33} is negative because a stress normal to the film increases its thickness³⁸. In comparing the piezoelectric and pyroelectric strengths of the various materials in Table 1.4, it was shown that although PVDF and its copolymers stand out among other polymeric materials, their activity is an order of magnitude lower than that of the traditional piezoelectric ceramics. However, if calculating the electromechanical coupling coefficient k_{31} , (a quantity reflecting the transducing capability of a material) from $k_{31} = d_{31} \sqrt{c/\epsilon}$ (where c is the stiffness and ϵ the permittivity), it was exhibited that, as a result of their very low dielectric constant, PVDF and its copolymers appeared comparably efficient to ceramics. Moreover, PVDF films can sustain about 100 times higher fields than ceramics, so that their power output per unit volume and their maximum elongation per unit field strength (quantities that are proportional to d^2cE^2) are about four to five times greater than in ceramics. Nevertheless, PVDF and other polymers are inferior to ceramics regarding to highest temperature of use: piezoelectric constants in PVDF reach a maximum at $\sim 80^\circ\text{C}$, where activity begins to fall as a result of increased molecular motions and consequent depolarization; this can be retarded to $\sim 11^\circ\text{C}$ by cross-linking the molecules with about 40 megarads of γ -radiation. However, at even higher temperatures, chemical degradation sets in with loss of HF that increases from α - to γ - to β -PVDF as a result of greater steric and electrostatic intramolecular repulsions within trans-segments.

Table 1.4 shows the piezoelectric and pyroelectric coefficients and other physical properties of several commonly used sensor materials. The three-dimensional anisotropy of the piezoelectric effect of PVDF is obvious. The d constant associated with the direction of tension (d_{31}) is an order of magnitude larger than the transverse piezoelectric coefficient (d_{32}). Both are positive. The d_{33} value of PVDF is always negative³⁸ because the stress on the film plane will decrease the thickness of the sample and increase the surface charge. Comparing the piezoelectric and pyroelectric strengths of various materials in Table 1.4, we find that although PVDF and its copolymers are excellent in other polymer materials, their sensitivity is lower than that of traditional piezoelectric ceramics. Considering the electromechanical coupling coefficient K_{31} (which reflects the amount of transduction capacity of materials), it can be seen that the energy conversion efficiency of PVDF and its copolymers is relatively high. In addition, the energy field of PVDF films is about 100 times higher than that of ceramics, so their power output per unit

volume and maximum elongation per unit field strength are about four to five times higher than that of piezoelectric ceramics. However, PVDF and other polymers are not as good as ceramics in terms of maximum service temperature: the piezoelectric constant in PVDF reaches a maximum at $\sim 80^{\circ}\text{C}$, and when the temperature is further increased, the depolarization effect will occur due to the increase of molecular motion and the piezoelectric coefficient will begin to decrease. This can be hindered by crosslinking molecules. However, at higher temperatures, due to the release of HF, the molecular chains begin to degrade and the piezoelectric ability of materials will gradually lose.

Table 1.4 Typical electroactive properties of various piezoelectric materials³⁸.

Material	Piezoelectric coefficient, d (pC/N)	Pyroelectric coefficient, p ($\mu\text{C}/\text{K}\cdot\text{m}^2$)	Density, ρ (g/cm^3)	Elastic modulus, c (GN/m^2)	Dielectric constant, ϵ/ϵ_0	Electro-mechanical coupling coefficient, k (%)	Acoustic impedance ($\text{Gg}/\text{m}^2\cdot\text{s}$)
PVDF (β -phase)	$d_{31} = 20-30$ $d_{32} = 2-3$ $d_{33} = -30$	30-40	1.8	1-3	10-15	11	2-3
PVDF (δ -phase)	$d_{31} = 10-17$ $d_{32} = 2-3$ $d_{33} = -10--15$	10-15					
VF ₂ -trifluoroethylene copolymers	$d_{31} = 15-30$	30-40	~ 1.9		15-20	~ 20	
Poly(vinyl fluoride)	$d_{31} = 1$	10	1.4	~ 1			
Poly(vinyl chloride)	$d_{31} = 1$	1-3	1.5	~ 4	3		
Nylon 11 (γ -phase)	$d_{31} = 3$	3	1.1	1.5	4		
Lead zirconate titanate	$d_{31} = 100-300$	50-300	7.5	80	1200	30	25
Barium titanate	$d_{31} = 80$	200	5.7	110	1700	21	25
Quartz	$d_{11} = 2$		2.7	80	5	10	14

1.4.3. Structure and phase conformation in PVDF

Large polymer chain is built by the repeating of basic atom groups. We call this basic unit in polymer chain as monomer. As we all know, PVDF is composed of $-(\text{CH}_2-\text{CF}_2)-$ monomers. And it looks that there is only one monomer in PVDF. However when considering the spatial distribution of atoms, there are 3 types of monomer $-(\text{CH}_2-\text{CF}_2)-$: trans bond (T), left and right gauche bonds (G^+ and G^-). As shown in Figure 1.14, the trans bond (T) has a dihedral angle of approximately $\sim 180^\circ$ and the left and right gauche bonds (G^+ and G^-) have dihedral angles of approximately $\pm 60^\circ$. Projecting from right side, we can look at the atom arranged on one plane. If the Carbon atom is located on the opposite direction, it is called T. If it has angle of 60° , it is G^+ , and if rotate -60° , it is G^- .

Any polymer chain is constructed repeatedly by basic atomic units. We call this basic unit in the polymer chain monomer. It is well known that PVDF is composed of $-(\text{CH}_2-\text{CF}_2)-$ monomer. When considering the spatial distribution of atoms, there are three types of monomers - $(\text{CH}_2-\text{CF}_2)-$: trans bond (T), left and right gauche bond (G^+ , G^-). As shown in Figure 1.14, the dihedral angle of trans-bonding (T) is about ~ 180 degrees, and the dihedral angle of measuring bonds (G^+ , G^-) is about < 60 degrees. Projected from the right, we can see atoms arranged in a plane. If the carbon atom is in the opposite direction, it is called T. If its angle is 60 degrees, then G^+ and if it rotates - 60 degrees, then G^- .

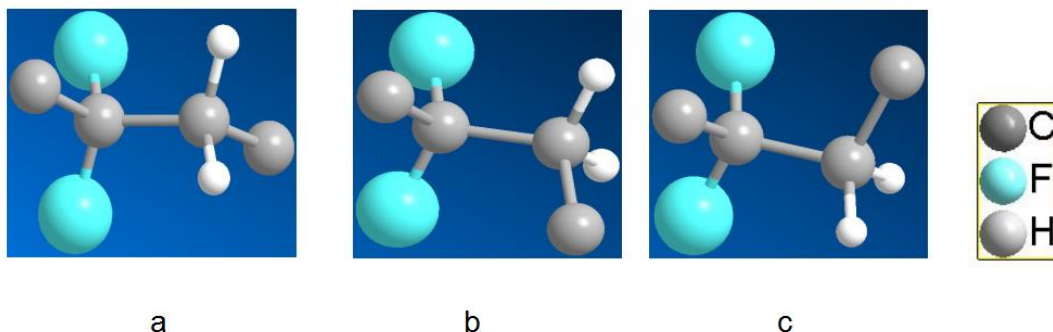


Figure 1.13 Three monomer types in PVDF: a, Trans (T); b, left Gauche (G^+); and c, right Gauche (G^-)

Different combinations of monomers on the carbon chain form different PVDF conformations.

Then different polymer chain conformations can crystallize to form different crystalline phases. For example, the beta crystal phase is constructed by all reverse chains (TTTT), while the alpha crystal phase is formed by alternating left and right trans (TG + TG-) chain conformations.

Figure 1.15 showed the molecular conformations and crystalline forms of PVDF^{39, 40}. In summary, the most common conformations are all-trans (TTTT) (figure 1.15a), and alternating left-right trans-gauche (TG⁺TG⁻) (figure 1.15b). The β phase is polar and uniaxial ferroelectric, as the polarization can be repeatably switched between opposite but energetically equivalent directions along the b-axis. The β phase unit cell nominally consists of two $-(\text{CH}_2\text{-CF}_2)-$ formula units, one along the c-axis parallel to the chains. The unit cell dimension in β crystal phase is approximately: $c=0.256\text{nm}$ along the chain axis, $b=0.491\text{nm}$ along the polarization direction which is the 2-fold axis and $a=0.858\text{nm}$ perpendicular to the chain axis and to the polarization. It is possible that the unit cell is twice as big, containing two monomers along the chain, because a ± 70 dihedral tilt-ordering would make the c-axis period two monomers long or $c \approx 0.512\text{ nm}$. The complete crystalline α phase structure shown in figure 1.2 (d) consist of opposing polar sublattices of the trans-gauche chains, resulting no net polarization in both parallel and perpendicular to the chain axis. The α crystal phase unit cell nominally consists of four $-(\text{CH}_2\text{-CF}_2)-$ units, two along the c-axis parallel to the chains and two in the plane perpendicular to the c axis. The unit cell dimensions are approximately: $a=0.964\text{nm}$, $b=0.496\text{nm}$, $c=0.462\text{nm}$ ⁴¹.

Figure 1.15 showed the molecular conformation and crystalline structure of PVDF^{40, 41}. In conclusion, the most common conformation is the alternating left-right-trans (TG + TG-) (Fig. 1.15b), followed by the all-trans conformation (TTTT) (Fig. 1.15a). The α crystalline alpha phase structure shown in Fig. 1.15 (d). The cell of α crystalline phase is nominally composed of four units $-(\text{CH}_2\text{-CF}_2)-$ - two parallel to the chain along the c axis and two on the plane perpendicular to the C axis. The crystalline α phase structure shown in Fig. 1.15 (d) consists of an anti-pole structure without net polarization in parallel or perpendicular to the chain axis. α phase crystal cell is about: $a = 0.96\text{ nm}$, $b= 0.496\text{ nm}$, $C = 0.462\text{ nm}$ ⁴¹. The β crystalline phase is polar and uniaxial ferroelectric, because the polarization can be reversed into each other along the two directions of the b axis. The β -phase crystal cell consists of two units of the formula $\text{CH}_2\text{-CF}_2$, which are parallel to the carbon chain along the c-axis. The unit cell size of the β crystal phase is

about: $a = 0.858$ nm, perpendicular to the chain axis; $b = 491$ nm along the polarization direction; $c = 0.256$ nm along the chain axis.

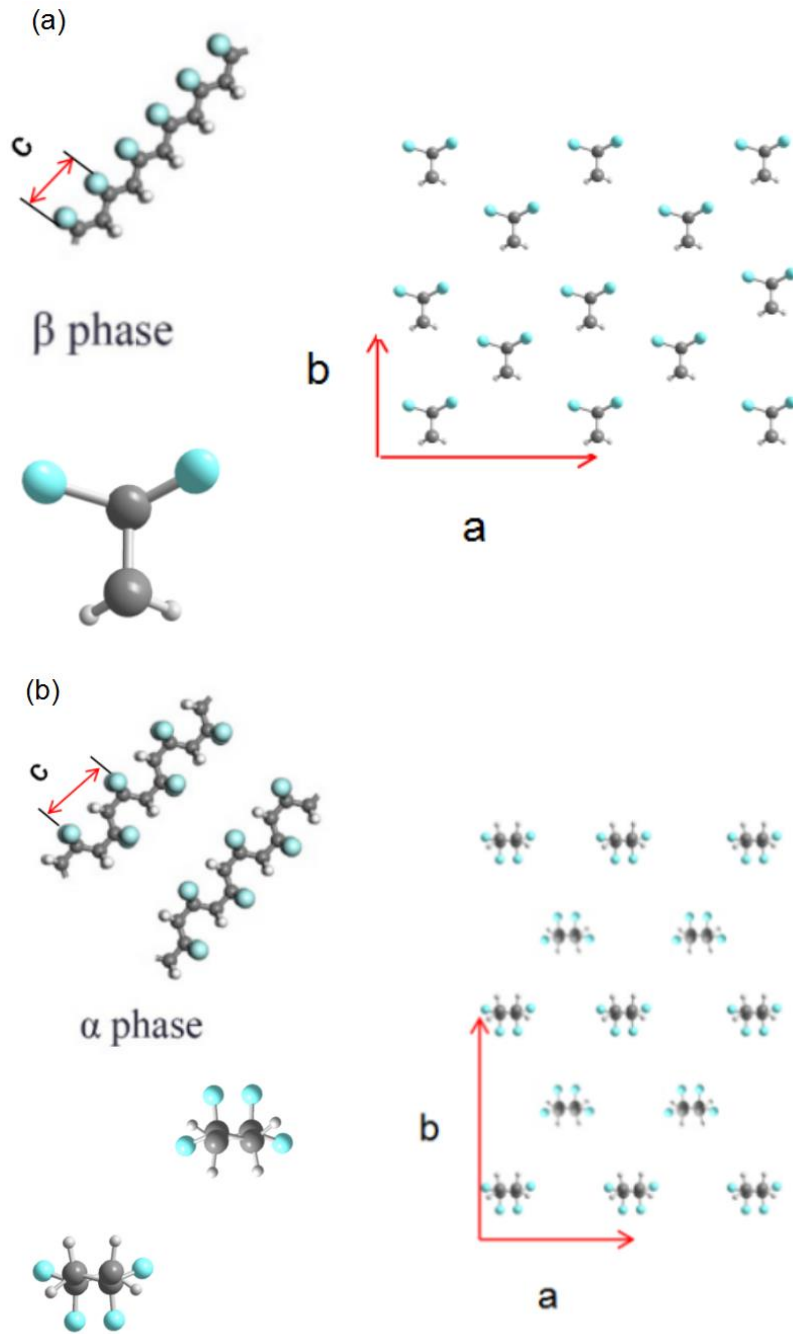


Figure 1.14 Structure of conformation and crystal phases in PVDF (a) the all-trans TTTT conformation and the cell of β crystal phase; (b) the alternating trans-gauche TG+TG- conformation and the cell of α crystal phase.

It should be noted that in all trans (TTTTTT) conformation, the net dipole moment is generated

because F and H atoms are located on both sides of the cell respectively. The dipole of the beta cell can reach 2.1 D ($=7 \times 10^{-30} \text{C}\cdot\text{m}$), resulting in the spontaneous polarization of $130 \text{mC}/\text{m}^2$. In (TG + TG-) conformation, a pair of units with opposite directions of adjacent chains form a cell, so the dipole moments of a single carbon-fluorine bond cancel each other in the cell. However, as discussed earlier, there is a ferroelectric domain in β crystals. Although a single grain is polar, due to the randomness of the orientation of the grain arrangement in the crystal, piezoelectric properties will not be generated in the whole crystal unless the sample is polarized. In order to obtain piezoelectricity, a strong electric field must be applied to the sample, which will be introduced in detail in the following section³².

In addition to the α and β phases, researchers also found the γ phase and δ phase in PVDF. But these phases are not common, and they are not very important for the practical application of PVDF. As space is limited, we will not discuss these issues in detail here. The unit cell dimension of phase is very similar to that of alpha, which is expected because the structure of these phases is also semi-helical. Table 1.5 shows unit cell size and space group⁴² for all four PVDF phases.

Table 1.5 Lattice constant of different phases in PVDF.⁴²

X-tal Structure	Space Group	a (Å)	b (Å)	c (Å)
α	$P2_1/C$	5.02	9.63	4.62
β	C_m2_m	8.58	4.91	2.56
γ	$C_2C_m, \beta = 90^\circ$	4.97	9.66	9.18
	$C_cC_m, \beta = 90^\circ$	4.96	9.58	9.23
δ	P_{2cn}	4.96	9.64	4.62

In addition, there are some important PVDF copolymers. For example, when a fluorine atom is substituted for a hydrogen atom in the monomer ($\text{CH}_2\text{-CF}_2$), a TrFE monomer will be produced. By blending the TrFE monomer with the ($\text{CH}_2\text{-CF}_2$) monomer in PVDF, the PVDF copolymer of P (VDF-TrFE) will be obtained. It is estimated that the application of P (VDF-TrFE) parameters in sensor field has better piezoelectric performance than that of homologues⁴³. Like PVDF, P (VDF-TrFE) copolymers can be crystallized into various crystalline forms, depending on the proportion of their different monomers and the crystallization conditions of⁴⁴. Under general

conditions, the alpha crystal of PVDF consisting of TG+TG- chain is more stable than the piezoelectric beta phase. In P(VDF-TrFE) copolymers, however, the internal energy of beta phase decreases and becomes more stable than that of alpha phase due to the introduction of TrFE, so it can be easily obtained. The main advantage of P(VDF-TrFE) over PVDF is that it has a wider available temperature range. In addition, the piezoelectricity of copolymer thin film can be obtained without mechanical stretching. In addition, it has a larger response bandwidth.

The structure of PVDF can be reviewed as followed. The basic unite, monomer, which has Trans, or Gauche type. The different arrangement of monomer in the carbon chain, can result in different chain conformations. Which include TTTT, TG+TG-, TTTG, etc... I reality, there could be infinite types of chain conformation. The major chain conformations correspond to the different crystal structures, alpha, beta, gamma, and delta. The major goal in this study is to achieve high production of beta crystal phase in PVDF which has the highest dipoles. And as a result, would have the best piezoelectric performance.

1.4.4. Piezoelectric mechanism for PVDF

Figure 1.16 showed the crystalline lamellar structure of PVDF. It is generally believed that the piezoelectricity of PVDF originates from the dipole in the phase structure of beta crystal. Most piezoelectric PVDF polymers are semi-crystalline and usually require an advantageous phase (usually beta phase) to polarize effectively in the electric field. This requires extensive mechanical stretching to reach an ideal phase before poling. After polarization, aligned dipoles in these semicrystalline polymers are prone to mechanical relaxation at temperatures far below their Curie temperature ⁴⁵. Polarization also results in a slight increase in dielectric constant, which is attributed not only to the rearrangement of dipoles in the beta phase material, but also to the transformation of alpha to beta resulting from the application of electricity ⁴³. However, there still exists some controversial about the piezoelectricity mechanism of PVDF which will be discussed as followed.

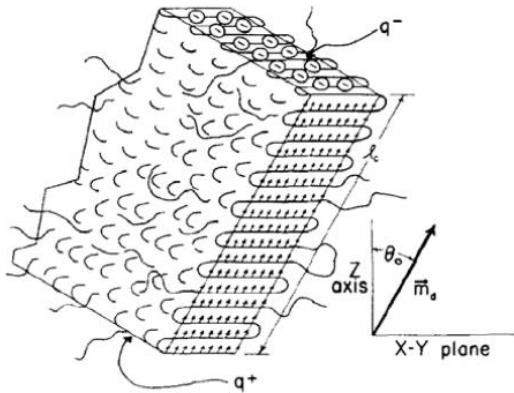


Figure 1.15 The lamellar crystal of PVDF crystal and its dipole orientation³³.

For many years, there have been different mechanisms for the piezoelectric effect of PVDF. After a preliminary debate on the effects of trapped space charges, most researchers agree that although space charges do affect piezoelectric properties, their effects can be neglected, because more than 90% of piezoelectric responses occur due to the polarization of dipoles in crystals³³. Some researchers have suggested that due to the dipole arrangement and high compressibility of PVDF, a large polarity change may occur through volume change, especially thickness change (also known as size effect). In addition, the theoretical mechanism is based on the change of dipole moment, including the increase of dipole moment due to mechanical stress proposed by Ohigashi⁴⁶. Most researchers believe that PVDF should be considered as a crystalline and amorphous biphasic material with different mechanical and dielectric properties. Therefore, the piezoelectric effect is attributed to the mechanical and electrical interaction between crystalline and amorphous phases. The specific reasons for the origin of piezoelectricity in two-phase materials can be summarized as follows: (1) intrinsic piezoelectric properties of crystal parts; (2) the difference between dielectric constant and strain between crystalline and amorphous phases increases the piezoelectric effect in materials; (c) the elastic constants in crystalline and amorphous regions are also different, and the different strains produced during polarization also contribute to the piezoelectric effect.

1.4.5. The conventional manufacturing processes for β phase PVDF

This section outlines the manufacturing process of piezoelectric PVDF. The polymer can be synthesized from gaseous ethylene fluoride (VDF) monomer by free radical polymerization. It can also form sheets by melt casting or by processing from solution (e.g. solution casting, rotary coating and thin film casting). Different PVDF film chains may be produced according to different processing methods. For PVDF, the alpha phase is the most energy stable, but it has very weak piezoelectric characteristics compared with the high polarity beta phase. Therefore, no matter which process can be applied, it usually produces a sample of alpha phase (or at least a high percentage of alpha phase). Then we need to consider how to convert the alpha phase into the beta phase for the application of electroactivity. By mechanical deformation and polarization, the structure of alpha phase can be transformed into polar beta phase to achieve piezoelectric characteristics. Although there are various methods for preparing beta-phase PVDF, most conventional processes include two steps: obtaining alpha phase and transforming alpha phase into beta phase. Here, we call these conventional processes a two-step process.

Those methods of creating piezoelectric β phase PVDF included hot pressing⁴⁷, stretching, Langmuir-deposition methods⁴⁸, and electro-spraying⁴⁹. When fabricating PVDF sheets in the thin film regime ($<10 \mu\text{m}$) through gel casting, β phase content can be controlled by solvent type, spin speed, drying temperature, humidity, pressure, and annealing temperature/atmosphere⁵⁰. Typically, the commercial production of PVDF film sensors began with the melting and extrusion of PVDF resin pellets into the form of a sheet. This process was followed by further stretching of the sheet, at a temperature that is well below the melting point, to obtain a β phase polymer to achieve the desired piezoelectric properties. When the PVDF melt was first subjected to mechanical drawing, it will break the spherulite formations into polymer crystallites aligned in the direction of the force. Since this deformation took place at low temperatures (below 90°C), the polymer chains were not able to move freely and become distorted, achieving most extended molecular form, which was the desired β phase conformation. Both uniaxial and biaxial drawing techniques may be applied with various elongation ratios (up to 700%). At this point, the molecular dipoles were still randomly oriented, resulting in zero net polarization. An electric field normal to the material surface was applied to align the dipoles and create uniform material

polarization. This can be accomplished through plasma or corona poling or the use of electrodes evaporated onto the film. Poling conditions such as field strength, temperature and poling time can vary, although increased values didn't necessarily guarantee higher resulting piezoelectricity. This completed the process and gave PVDF piezoelectric properties, making into a useful electroactive polymer. The microstructure changes in PVDF during drawing and poling processes were further illustrated as below³³.

Specifically, the methods to generate piezoelectric beta-phase PVDF include hot pressing⁴⁷, stretching, Langmuir deposition⁴⁸ and electrospray⁴⁹ etc. The beta phase content of PVDF piezoelectric thin films can be easily controlled by solvent type, rotation speed, drying temperature, humidity, pressure and annealing temperature⁵⁰. In industry, the production of PVDF thin film sensors generally adopts melting and extrusion of resin particles. Subsequently, the sheet is further stretched at temperatures far below the melting point to obtain the desired piezoelectric properties of the beta-phase polymer. When the PVDF melt is first mechanically stretched, it will split the spherulites into polymer crystals arranged along the direction of force. Various elongation (up to 700%) can be obtained in both uniaxial and biaxial drawing technology. Finally, a strong electric field perpendicular to the tensile direction is applied to rearrange the dipoles to form uniform material polarization. This step can also be achieved by plasma or corona polarization or by using electrodes evaporated onto thin films. Polarization conditions such as field strength, temperature and time may vary. When this process is completed, PVDF will be endowed with piezoelectric properties and become a useful electroactive polymer. The microstructural changes of PVDF during stretching and polarization will be further introduced as follow.

Figure 1.17 shows a typical two-step process. Firstly, random oriented crystalline and amorphous structures were found in polymer melts. Mechanical stretching converts the polymer into a polar beta phase conformation and orientates it, as shown in Figure 1.18 (b). Finally, by polarization, the dipole orientation of the grains tends to be the same. As shown in Figure 1.18 (c), a uniform polar material with piezoelectric properties is formed. For these two-step processes, the focus of the study is the second step, that is, how to effectively transform the alpha phase sample into the beta phase. In general, the conformational changes of PVDF can occur through mechanical

stretching and/or polarization processes. Increasing the drawing temperature will enhance the formation of alpha phase. The content of beta phase and piezoelectric activity increase with the increase of flattening ratio, balling voltage, voting temperature and polarization time. The results show that the optimal piezoelectric performance of 55% is achieved at high drawing ratio (> 1), applied voltage ($> 75\text{MV/m}$), polarization temperature ($80\text{-}95\text{ }^\circ\text{C}$) and polarization time (15 minutes to 30 minutes). Transformation of the polymer chain conformation, along with a conversion to crystalline β phase, can be achieved by stretching at low temperatures⁵¹. Some studies also show that the inhomogeneous stress distribution in the sample plays an important role in the crystal transformation from alpha to beta phase, because the transformation only occurs in the region where the local stress is higher than the critical stress⁵². In addition, some authors have also studied the kinetic factors of the formation of beta phase, Gregorio et.al⁵³. From the experimental results, it is inferred that the maximum crystallization rate of beta phase occurs at 60°C or slightly lower.

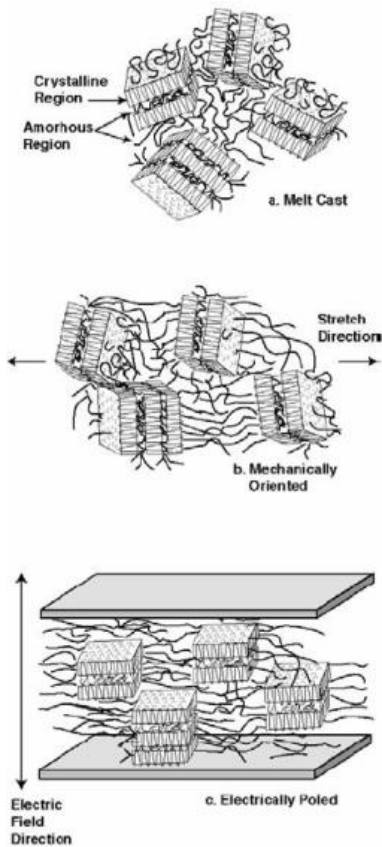


Figure 1.16 The stretching and polarization process in PVDF: (a) melt cast samples; (b) grain alignment through mechanical stretching; (c) dipole oriented due to the applied electrical field³³.

Although great progresses have been made, the application of piezoelectric PVDF is still limited by the complexity of two-step process, especially the lack of continuous production. In recent years, many researchers have done a lot of research on the production of fibre PVDF by electrospinning⁵⁴. This is because PVDF fabrics can be produced by electrospinning, while controlling the ferroelectric and piezoelectric beta phases of PVDF, thus combining tension and polarization into a step. Beta-phase PVDF can also be grown directly on KBr crystals²⁹. In this study, these methods of directly obtaining beta-phase PVDF can be called one-step process.

In addition, the doping of TrFE or other monomers in PVDF copolymers is considered to be the key reason for the formation of beta phase, which is also the reason why piezoelectric properties are easily obtained. Therefore, using trifluoroethylene (TrFE) and other monomers to introduce defects into PVDF is a very popular method to obtain piezoelectric PVDF. It has been reported that if the TrFE content is higher than 18%, the pvdfn-trfe copolymer will form the same chain conformation with the beta phase PVDF⁴³. By means of annealing, simultaneous stretching and polarization, the content of beta phase in the copolymer can be further increased. Although the dipole moment of TrFE monomer unit is less than that of PVDF, the polarizability of copolymer is usually higher than that of pure PVDF due to the higher crystallinity of copolymer, which leads to better piezoelectric properties. Another way to form the structure of PVDF copolymer is to evaporate in vacuum on a suitable substrate. At this moment, film thickness, substrate temperature, deposition rate, electric field strength and substrate type have great influence on the generation of beta phase. In conclusion, most of the ferroelectric phases of the copolymer P(VDF-TrFE) (similar to the beta phase in PVDF), can be prepared directly. This brings flexibility in design and processing, making copolymers a better choice than PVDF in sensor actuator applications.

After PVDF is fabricated, some post-processing is usually needed to further improve the microstructure and piezoelectric properties. At present, three post-processing methods can be used to enhance the formation of beta-phase crystals. (1) Annealing and cooling: Temperature plays a significant role in the crystallization of PVDF. High temperature cooling rate⁴ has an effect on the relative content of alpha and beta phases. (2) Polarization: It has been discussed many times before that in order to produce functional piezoelectric materials, it is necessary to be

exposed to a strong external electric field up to 80 MV/m in order to rearrange the domains⁵⁵. Polarization is usually carried out in an oven at 80 °C. After polarization treatment, the sample needs to be cooled and maintained at room temperature (25 degree C) for a period (3 hours). (3) Pressing and stretching: the beta phase⁴ of PVDF can be enhanced under high pressure. In order to apply uniform pressure, it is optional to clamp the film between the rubber pads. Different pressure and time are applied under different temperature conditions, and then cooled and maintained at room temperature for about 3 hours.

1.4.6. Material characterization methods for PVDF

X-Ray Diffraction.

In this study, the phase of PVDF films was identified by X-ray diffraction (XRD). Here is a brief introduction to the working principle of XRD: the atomic spacing of most crystal materials is close to the wavelength of X-ray (0.5 Å -2.5 Å). When the sample is irradiated by the incident X-ray, the incident X-ray will be diffracted. Different lattice spacing, lattice shape and atomic type will produce different characteristic diffraction peaks. Thus, a diffraction pattern based on different crystal types can be established. The phase analysis of the material is carried out according to different characteristic diffraction peaks. When the monochrome X-ray beam partially reflects from the sample, i.e. the lattice plane, the interference of the reflected beam can only be reflected in a specific direction. When the path difference of BAB + BC (see Figure 1.17) is an integral multiple of the X-ray wavelength, the intensity of reflected light will be greatly enhanced. This relationship is given in detail by the Bragg equation as below:

$$n\lambda = 2d \sin\theta$$

where λ is the incident wavelength, θ is the angle of incidence, d is the interplanar spacing of lattice planes.

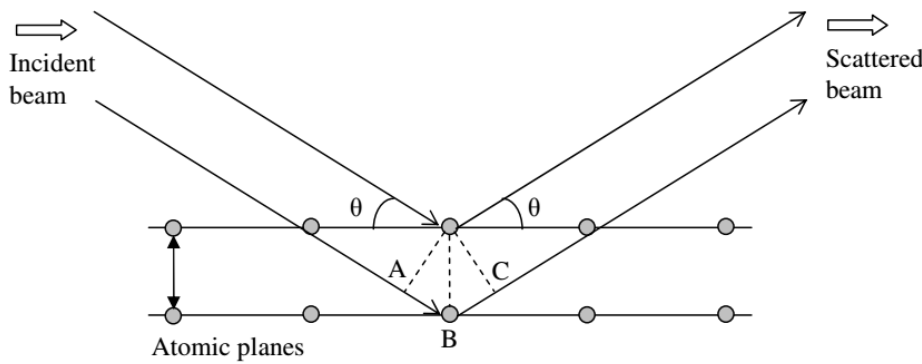


Figure 1.17 X-ray diffraction of Bragg's law⁵⁶.

The XRD devices are generally equipped with a Rigaku d/max Ultima 2200 X-ray diffractometer with a Cu K alpha radiation and a graphite monochromator⁴⁷. The beta phase in the sample can be confirmed by the existence of X-ray diffraction pattern. Because of the influence of beta phase, this reflection is produced at $2\theta = 20.78^\circ$. The strong single peak at this position is an important feature of the beta phase PVDF in the XRD spectrum. Figure 1.19 shows the X-ray diffraction patterns of general alpha-and beta-phase PVDF films. It was observed that the strongest peak of beta phase (110) occurred at $2\theta = 20.78^\circ$, which was close to the value calculated by Hasegawa et al. from unit cell size (20.8°). On the contrary, the strongest peak of alpha phase appears near 20.15° .

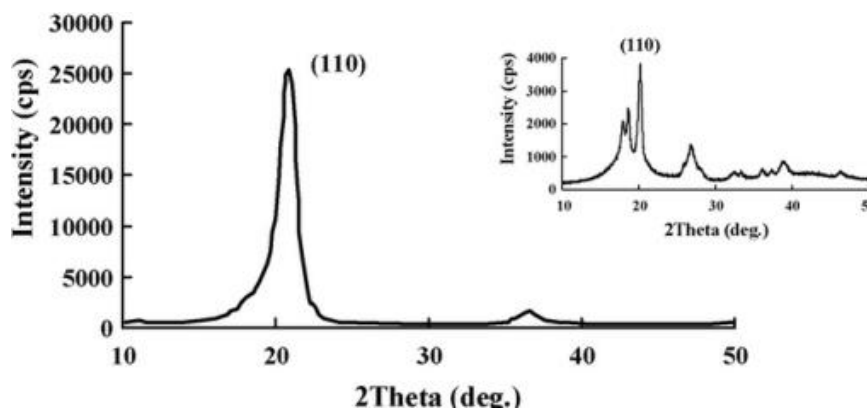


Figure 1.18 The typical XRD patterns in PVDF (inset is the α phase)⁴⁷.

XRD can also be used to calculate the crystallinity of crystals in materials. Crystallinity can be defined ⁴ as the weight fraction of the crystalline region of the sample divided by the sum of the amorphous and crystalline regions and 4. As shown in the following formula:

$$\alpha(\%) = \frac{A_c}{A_a + A_c} \times 100$$

where A_a and A_c are the area of the amorphous and crystalline in the samples, respectively. And the Scherrer equation⁵⁷, was used to calculate the crystallite size of the PVDF.

$$\tau = \frac{K\lambda}{L\cos\theta}$$

where L is the line broadening at half the maximum intensity, K is a constant which vary between 0.89 and 1.39.

Fourier Transformed Infra-Red Spectroscopy (FTIR)

Infrared spectroscopy is another important material characterization method. FTIR collects spectra based on measuring the temporal coherence of radiation sources and uses time-domain measurements of electromagnetic radiation or other types of radiation for measurement. Fourier transform spectrometer is a Michelson interferometer with a movable mirror. By scanning a movable mirror at a certain distance, an interference mode is generated, which encodes the spectrum of the source. Simply put, the Fourier transform spectrometer consists of two rectangular beams positioned each other. A beam splitter is placed at the right-angle vertex, which is oriented at 45° relative to the two mirrors. Then the radiation event on the beam splitter with one of the two ports is divided into two parts, each part propagates downward from one of the two arms and reflects from one of the mirrors. Then the two beams are reconstructed and the other port is transmitted. The simplified optical layout of the FTIR interferometer is shown in Figure 1.20.

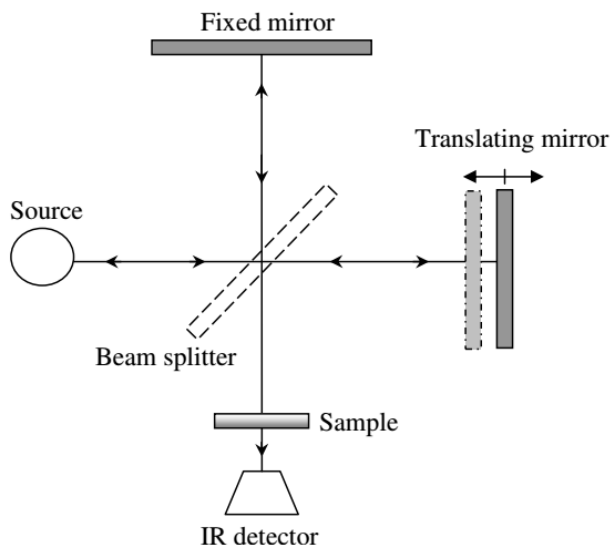


Figure 1.19 Schematic setup of a typical FTIR interferometer⁵⁸

Infrared spectroscopy utilizes the characteristic that molecules have specific frequencies, i.e. they correspond to their discrete energy levels when they rotate or vibrate. In the vibration mode, due to the change of the permanent dipole, the molecule has infrared activity. A simple diatomic molecule has only one bond, which may stretch. More complex molecules have many bonds and produce conjugated vibrations, which results in the existence of characteristic frequencies associated with chemical groups in infrared absorption of materials. Because each molecule has its own unique level of quantized vibration and rotational energy. Therefore, this technique is based on the principle that a molecule absorbs infrared radiation at an appropriate frequency and excites it from one vibration or rotation level to another, so different functional maps correspond to different energy absorption states.

It's worth noting that although we applied FTIR to detect different crystal phases in material, this method cannot directly characterize the crystal structure. It can detect different structures by observing the featured atom group in that structure. In most cases, we use this method to characterize crystal structures just like XRD, and it make no difference. In other cases, it will lead to serious misunderstandings. Take the case in this study for example: from the structural point of view, we have made some attempt to investigate the existence of different phases of

PVDF film. FTIR spectra was used to characterize the structure of PVDF polymer chains as part of the measurement. Infrared spectroscopy can accurately determine the local structure, that is, the short-range ordered structure, and can be used to accurately determine the different chemical groups. However, it is impossible to distinguish between crystals and amorphous crystals produced by the same carbon chain configuration, i.e. long-range ordered structures.

In practice, however, FTIR is still used to distinguish the composition of different phases in PVDF or its copolymers. This is because some vibration modes exist only in one carbon chain configuration of PVDF, either in the total all-trans of ferroelectric phase or in alternating TG TG conformations⁵⁹. In this study, FTIR spectroscopy was used to successfully distinguish the different existing phases of PVDF and P (VDF-TrFE) films, i.e. ferroelectric and paraelectric phases. As shown in Figure 1.22⁴³, the infrared transmission spectra of PVDF and P (VDF-TrFE) (80/20) films show many absorption peaks at 1402, 1286, 1186, 11224, 1077, 883, 844 and 476 cm⁻¹, and many weak absorption peaks are 1402, 943, 678 and 505 cm⁻¹.

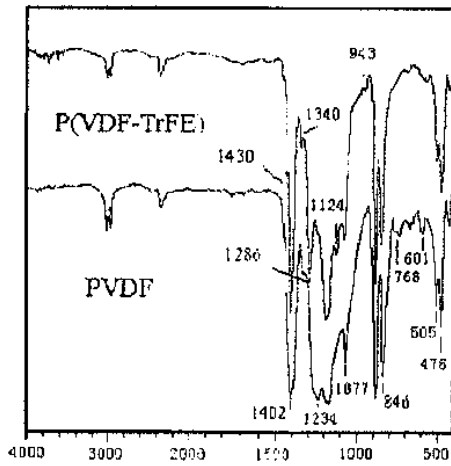


Figure 1.20 The ferroelectric and paraelectric phases adsorb peak in FTIR spectrum of PVDF and P(VDF-TrFE)⁴³

The fraction of β -phase crystals $F(\beta)$ in the samples can be calculated by⁶⁰:

$$F(\beta) = \frac{A_{\beta}}{(k_{\beta}/k_{\alpha})A_{\alpha} + A_{\beta}} = \frac{A_{\beta}}{(1.26)A_{\alpha} + A_{\beta}}$$

In the wavenumber range of 650-1100 cm^{-1} shown in Figure 1.21, the values of A_α and A_β were estimated by FTIR result. According to Lambert-Beer Law, the absorption bands of A_α and A_β correspond to the peaks of 763 and 840 cm^{-1} , respectively. The absorption coefficients of K_α and K_β are 6.1×10^4 and $7.7 \times 10^4 \text{ cm}^2/\text{mol}^{-1}$, respectively.

Atomic Force Microscopy

Atomic force microscopy (AFM) is sometimes used to characterize the surface morphology of PVDF films. It belongs to the scanning probe technology, which detects the surface morphology of samples by scanning the tip of the surface. It will use one with a length of 100 to 200 microns and a tip at the free end of the cantilever. Cantilever is usually made of silicon and has a very low elastic coefficient. The force between the tip and the sample surface causes the cantilever to bend or deflect - this deflection can be measured when scanning the sample surface. These deflections enable the computer to generate the surface topography of the sample. Several forces can deflect the AFM cantilever. The most common is Van der Waals. It is very important to discuss the dependence of van der Waals force on the distance between the tip and the sample, because it determines the choice of the mode of operation of the AFM. There are two different ways: (1) contact system; (2) non-contact system. In contact type AFM system, the cantilever keeps less than a few angles from the sample surface, and the inter-atomic force between the cantilevers keeps tens to hundreds of angles and inter-atomic forces from the sample surface. In contact mode, also known as repulsion mode, the tip of the AFM is in soft "physical contact" with the sample. In our experimental research, we mainly use non-contact AFM mode, because we study the soft polymer surface, contact mode will affect or damage the sample surface.

Most of the AFMs use optical technology to detect the position of the tip of the cantilever. In the most common settings, as shown in Figure 1.22, the laser beam bounces from the back of the cantilever to a position sensitive photodetector (SPD). When the cantilever bends, the position of the laser beam on the detector changes. The PSPD itself can measure light displacements as small as 10 Å. Once the cantilever deflection is detected, the surface topography can be generated by running in one of the two motion constant height or force modes. In constant height mode, the spatial variation of cantilever deflection can be directly used to generate terrain data

sets, because the height of scanner is fixed when scanning. In the constant force mode, the total force applied to the sample is constant while the cantilever deflection remains unchanged. The deflection of the cantilever beam can be used as input of the feedback circuit, which moves the scanner up and down in z axis, and responds to the different heights of the surface by keeping the deflection constant of the cantilever beam. This mode is usually used to photograph the atomic scale image of the atomic plane, in which the cantilever deflection and applied force change little. This mode is also essential for recording real-time images of changing surfaces, where high scanning speed is essential.

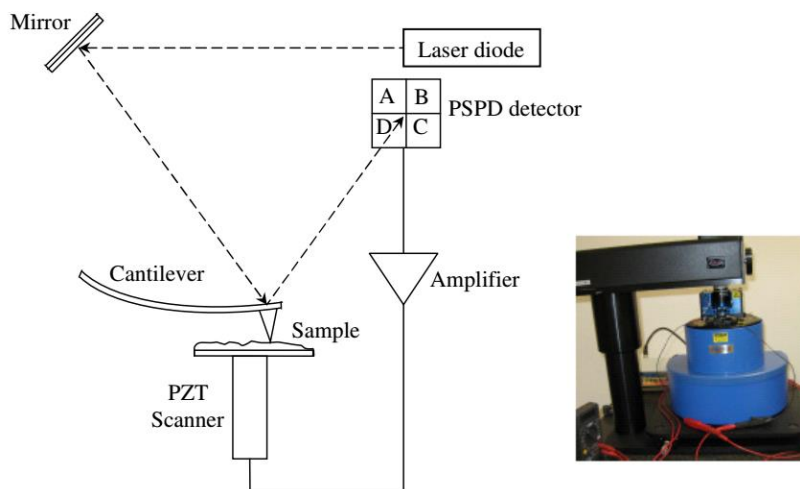


Figure 1.21 The typical schematic of AFM ⁵⁶.

Scanning electron microscopy

Scanning electron microscopy (SEM) is the most commonly used method to observe the surface and cross-section morphology of PVDF. The instrument used for imaging is SI-SX-40 scanning electron microscope. All samples need to be first coated on the Edwards S150B sputtering coating machine with a layer of gold about 300 Å thick. We use the resolution of 1000x and 8000x to view all the film samples. The grain size and the size of some voids and micro-particles can also be estimated by scanning electron microscopy.

Capacitance Measurement

The permittivity of a material is determined by the ability of a material to become polarized

when exposed to an external electric field. In other words, permittivity serves to relate a material's ability to transmit an electric field. Permittivity has units of F/m (or more commonly pF/m). The relative permittivity of a material, on the other hand, is simply the ratio of the amount of energy stored within a material when an external voltage is applied, to that stored by a vacuum. The relative permittivity is a unitless value. The samples of the thin film for capacitance, relative permittivity, and hysteresis loop analysis, were treated on each side with a small, rectangular shaped amount of colloidal silver electrode. The sample was then connected to an LCR Meter. The capacitance measurements were conducted at a frequency of 100Hz and a drive voltage of 0.10V. Accompanying each capacitance value was the tangent loss which is simply a measure of how much the thin film sample has aged (a higher tangent loss corresponds to a higher degree of aging). The complete set up for the capacitance measurement is pictured below in Figure 1.23.

The permittivity of the material is determined by the ability of the material to polarize under the applied electric field, which means permittivity reflects the ability of material to propagate electric field. It generally uses F/m (or pF/m) as the unit. On the other hand, we usually use relative permittivity to express the ratio of energy stored in material to that stored in vacuum when applied external voltage. The relative permittivity is a non-unit value. In the detection, a small amount of rectangular colloidal silver electrodes are usually used to pretreat the capacitance, relative dielectric constant and hysteresis ring analysis samples of the films, and then the samples are connected to the LCR meter. The frequency of capacitance measurement is generally 100 Hz, and the driving voltage is 0.10 v. The dielectric loss is also measured with each capacitance value, which is an index to measure the aging degree of thin film samples (higher dielectric loss corresponds to higher aging degree). The arrangement of the dielectric constant measuring device is shown in Figure 1.23 below.

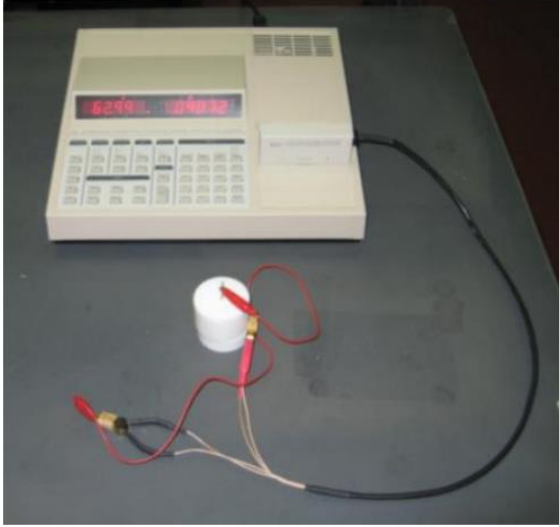


Figure 1.22 The setup of Capacitance Measurement with LCR Meter

In order to calculate the permittivity and relative permittivity of the PVDF samples the following equation was used:

$$C = \epsilon_r \epsilon_0 \frac{A}{t} \quad \text{and thus:} \quad \epsilon_r = \frac{Ct}{\epsilon_0 A}$$

where: C = the capacitance of the thin film (F)

ϵ_r = the relative permittivity of the thin film

ϵ_0 = the permittivity of free space in a vacuum = 8.854×10^{-12} F/m

A = the area of the electrode (m²)

t = the thickness of the film (m)

Ferroelectric characterization

Ferroelectric analyzer uses high voltage AC signal combined with Sawyer-to tower circuit to test the ferroelectric characteristics of thin film samples and uses mixed signal digital oscilloscope to measure the response signal of thin film. The piezoelectric potential of PVDF films was characterized by measuring the potential shift or polarization (D) of PVDF films at high AC electric field⁶². The most commonly used tester are Agilent 33210A Arbitrary Waveform Generator and Ultravolt 5HVA24 High Voltage Module (Amplifier), which apply 10 Hz AC

signal in the direction of film thickness. This experiment also needs to use Dektak IIA profiler to measure the thickness of each film and calculate the voltage required for each sample to apply an appropriate electric field. Finally, the D-E hysteretic response of PVDF films will be obtained, and the remnant polarization of PVDF films will be determined by using this curve⁶³. Both the schematic and actual picture of the ferroelectric analyzer are shown as below.

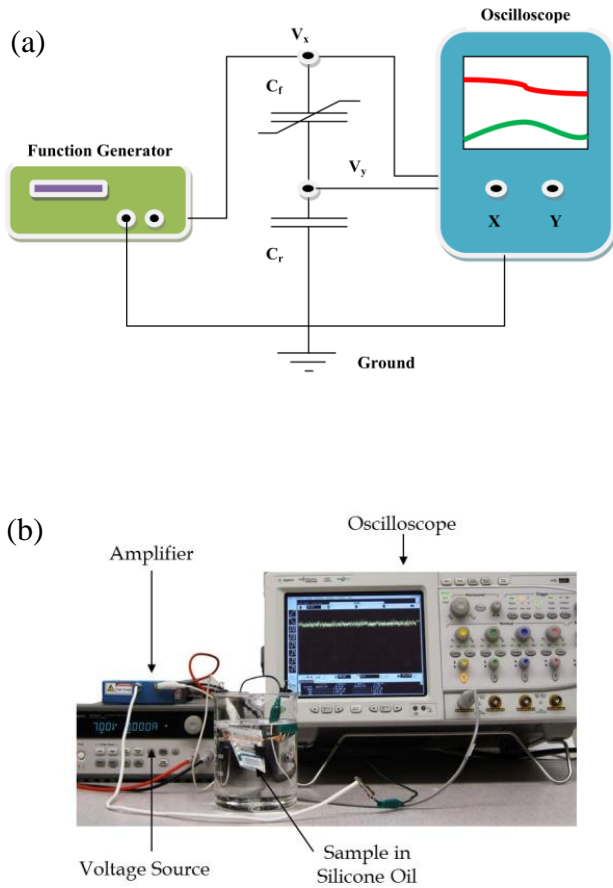


Figure 1.23 (a) The schematic of Sawyer-Tower circuit diagram, and (b) The setup of ferroelectric testing instrument

As shown in Figure 1.25, ferroelectric hysteresis loops were constructed, from which the values of remnant polarization P_r and the coercive field E_c may be determined⁶⁴. A function generator and a charge amplifier were used to provide a voltage with suitable shape, amplitude and frequency. This voltage was applied to the sample, and hysteresis measurements were made using bipolar and unipolar currents sequentially⁶⁵. In a hysteresis measurement, the measured

current was a combination of the current due to the polarization reversal, and the resistive and the capacitive components⁶⁵.

As shown in Figure 1.25, the values of residual polarization P_r and coercive force E_c ⁶⁴ can be determined from the hysteresis D-E curve. However, in actual measurement, the situation is complex. Functional generators and charge amplifiers are needed to provide voltage with appropriate shape, amplitude and frequency. At the same time, in the hysteresis measurement, the actual measured current is the combination of current caused by polarization inversion, resistance and capacitance component⁶⁵ as below.

$$I_t = A \frac{dP}{dt} + \frac{V}{R} + C \frac{dV}{dt}$$

where I_t is the total current through the thickness direction, A the electrode area, P is the polarization, V is the voltage, R is the resistance, C is the capacitance and t is the time. In order to obtain accurate D-E curves, it is necessary to eliminate unwanted resistance and capacitance components in ferroelectric analyzer in order to determine the true value of polarization current.

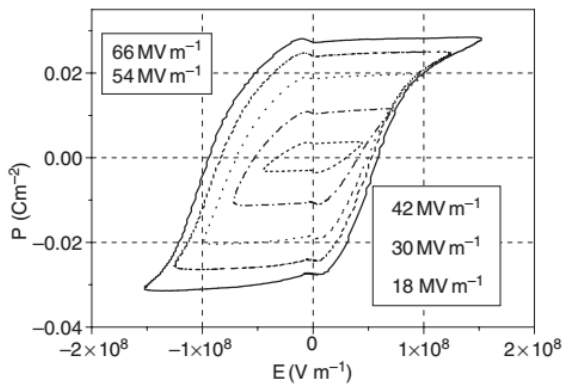


Figure 1.24 D-E loops at 1Hz under different electric fields for PVDF thin films⁶⁴.

1.5. Description of the fundamental problems

1.5.1. Basic design of the PVDF sensors

Instrumented piezoelectric sensors and actuators as part of an SHM system can provide quantitative measurements of structural performance and can even detect damage initiation and propagation. Reviews of SHM have included piezoelectric transducer fabrication and use in many SHM applications⁶⁶. This section provides an overview of select studies which use piezoelectric materials for SHM as are most appropriate for the purposes of this research. One of the simplest and most common applications of piezoelectric materials in SHM is to use them as piezoelectric sensors. The advantage of these materials is that they can be directly used as sensors in the structure, without consuming any energy of their own, and require only a few external circuits. As mentioned earlier, these piezoelectric sensors can measure the signals generated by structural vibration to monitor the occurrence of damage in the structure.

Piezoelectric sensors can also be used in combination with actuators to achieve more complex SHM applications.

Two types of PVDF-based piezoelectric sensors can be obtained, which are PVDF thin film d_{31} sensors and PVDF fiber d_{33} sensors. In PVDF thin film d_{31} sensor, it was poled between two electrodes where the electric field was perpendicular to the thickness direction (called d_{31} effect). After proper post processing of the PVDF film, the sensor can be used to sense the transient in-plane strains for the composite structure. The second sensor type was based on the PVDF micro-fibers. The sensor was poled along the fiber direction, like the poling of the macro-fiber composites made in Smart Materials, Co. (called d_{33} effect). Both types of sensors can be designed to optimize the sensing performance. The thickness of the PVDF film, the arrangement of the PVDF fibers will be selected to provide the optimal sensitivity. For the fiber d_{33} sensor design, the local geometry was governed by three parameters: (1) electrode finger spacing (p), (2) electrode finger thickness (h_e), and (3) finger width (w). The effective excitation frequencies from the fiber d_{33} sensor depended on the spacing of electrode fingers, since the excitation from each finger pair need to be synchronized in phase to produce a constructive signal. The freedom in controlling the geometry and structure of sensors will be critical for further modifying the

geometry design and processing conditions for optimal sensor performance.

The output signal of PVDF piezoelectric sensor can be designed to be proportional to the change of parameters such as curvature of structure. Cracks or delaminations in structures such as plates and beams may be directly related to local stiffness disturbances. The local stiffness loss or disturbance, in turn, can cause local changes in the curvature of the structure. The PVDF flexible sensor can detect the structural dynamic response related to these changes in curvature without damaging the structural integrity or surface finish. This function makes PVDF sensor one of the most ideal sensors in SHM applications.

A typical piezoelectric film with metal electrodes was shown in the following figure. Its main body consisted of a 28-micron thick PVDF film with silver-ink coatings (5-7 μm) deposited on both sides to provide electromechanical coupling. Very small insulating copper/silver wires (0.12 mm in diameter) were connected to both ends of the electrode. The sensor was also packaged with standard translucent tape. In addition, tools such as fine sandpaper (320 grains) for removing wire insulation and scalpel knife blades for cutting sensor materials were used.

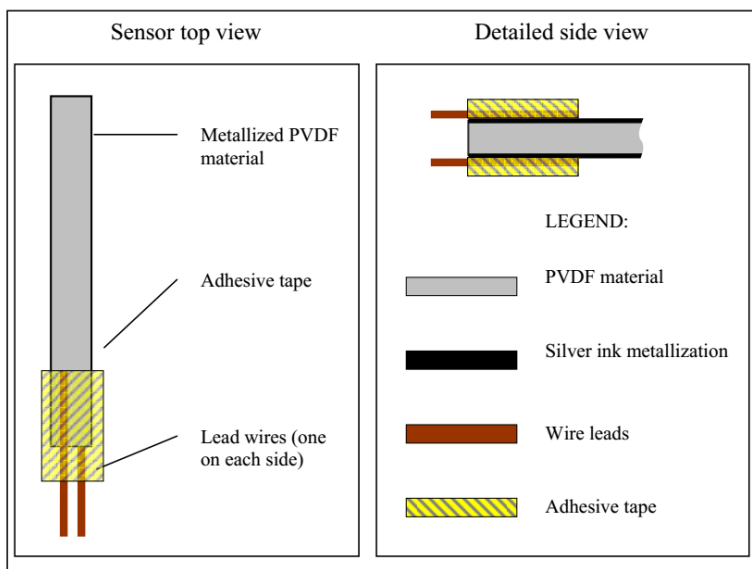


Figure 1.25 Schematic of a typical PVDF piezoelectric sensor³³.

1.5.2. Wiring and metallic electrodes

Although we know that the sensitivity of the sensor does not simply depend on the single factor of electrode conductivity, especially in low frequency operation ⁶⁷. (In high frequency applications, the conductivity of electrodes has a greater impact than in low frequency applications). Conductivity is still a priority factor in the selection of electrode materials. The low conductivity of the electrodes results in signal loss, and the signal-to-noise ratio (SNR) decreases at higher frequencies. In designing intelligent structures, the conductance of wiring and electrodes must be carefully considered.

Evaporated metal electrodes were the most common option because the metals usually had higher conductivity. We can also fabricate highly conductive electrodes by metal ink or paste. Two important factors predominately determined the conductivity of the resulting electrodes and interconnects, which were the thickness and the curing condition of the silver/copper film. To obtain good electrical conductivity of the electrodes and interconnects, a good thickness of the conductive film was critical. Proper curing condition was critical to obtain the minimum resistivity of the conductive traces. The curing temperature and the ramp rate both need to be carefully selected. A proper curing temperature will be able to achieve the small resistivity, and at the same time, will affect the properties of the PVDF film and composite structures. In AM technology, silver nanoinks with a low curing temperature are usually selected for electrodes and interconnects printing to prevent the adverse effect on the piezoelectric performance in PVDF. We need to determine the best curing temperature and speed of conductive silver ink through experiments to achieve the best conductivity of the electrode. Tuukkanen et al. ⁶⁷ fabricated flexible piezoelectric sensor elements by direct printing method. His research shows that flexible printable electrode materials can be compatible with temperature sensitive functional substrates. The low temperature solidified electrode is printed on both sides of the nonmetallic polyvinylidene fluoride film. It can measure the DC resistance of electrodes and the sensitivity of sensor elements. The measured resistance and sensor sensitivity are 10^{-1} to $10^6 \Omega/\square$, and 23 to 29 pC/N, respectively.

Although metal-electrode fabrication on PVDF film using ink-jet printing was previously

demonstrated, the required high-temperature sintering step caused limitations in the sensor functionality⁶⁸. The polarization direction in the crystalline film can be controlled with the simultaneous application of an electric field. Due to the delicate fabrication procedure, the piezoelectric properties of the PVDF film were degraded when heated above 80°C. Carbon-based nanomaterials such as carbon nanotubes (CNT)⁶⁹, and conducting polymers such as PEDOT:PSS⁷⁰, were suitable materials for printed electronics since they were solution processible and compatible with flexible films. These materials can also provide both high conductivity and optical transparency, which were required in several applications. Further, these electrode materials can be used on temperature-sensitive films such as PVDF since they did not require subsequent heating treatments as do most metal particle-based printing inks. Lee et al.⁷¹ fabricated flexible organic film speakers with an ion-assisted reaction (IAR) treated PVDF as the active layer and poly(3,4-ethylenedioxythiophene):poly(styrene sulfonate) (PEDOT:PSS) materials with various organic solvents, indium tin oxide (ITO) or copper (Cu) as the electrodes. IAR was used to improve the adhesion since the highly hydrophobic surface of PVDF showed poor adhesion with other materials. Schmidt et al. fabricated PVDF sensors containing printed PEDOT:PSS electrodes using airbrush and ink-jet techniques⁶⁷. They found a even better response than for actuators constructed from sheets with metal electrodes.

Although the method of fabricating metal electrodes on PVDF films by inkjet printing has been successful, the required high temperature sintering steps may affect the performance of sensor functional components 68. The direction of polarization in piezoelectric thin films can be controlled by simultaneously applying electric field. The piezoelectric properties of PVDF films decrease when heated above 80 °C. Carbon-based nanomaterials (such as carbon nanotubes (CNT)⁶⁹ and conductive polymers (such as PEDOT: PSS)⁷⁰ may be more suitable electrode materials for printing sensors because they are flexible and compatible with flexible thin films. More importantly, because they do not require subsequent heat treatment, these electrode materials can be used in temperature-sensitive films (such as PVDF). Lee et al.⁷¹ manufactured a flexible organic film loudspeaker for ion-assisted reaction (IAR). PVDF was used as a functional layer, poly (3,4-ethyldioxythiobenzoic acid methyl ester): P (styrene sulfonate) (PSS) material and various organic solvents, zirconia (or copper) were used as electrodes, and good sensitivity was obtained. Schmidt et al.⁶⁷ made PVDF sensors using spray guns and inkjet technology,

which contained printed PEDOT: PSS PSS electrode, and obtained better energy conversion efficiency than the actuators made of metal electrode plates.

1.5.3. Post-printing heat treatment and poling

In order to optimize the performance of PVDF piezoelectric sensor, it is necessary to carefully study and select the post-processing method of printing in order to achieve the maximum piezoelectric constant and obtain the best sensitivity. In addition, after the single-layer piezoelectric sensor is obtained, the corresponding composite polymer can be studied and deposited to control the thickness and build a three-dimensional intelligent structure.

As mentioned earlier, in the process of obtaining beta phase PVDF, especially when we use the so-called "two-step" process, poling should be considered as part of the process for obtaining beta phase. In order to obtain the beta phase, it is necessary to stretch the alpha PVDF film, and apply a very high electric field to the sample at high temperature. Finally, in the presence of electric field, the temperature is lowered and the grain is locked in the polarized state. Therefore, polarization is included in the second step of the "two-step" process. Strictly speaking, we cannot call this process true polarization, because the real polarization process can only occur when the sample has dipoles. In fact, in this "polarization" process, two different physical processes occur: one is to complete phase transition, producing dipoles in the material; the other is to align those dipoles along the direction of the external electric field. Only the latter is a real polarization process, which is required by the two-step and one-step processes. And this 'real' polarization process is the main topic of this section.

Poling processes in PVDF were still quite empirical because a thorough understanding of the physical processes involved in poling had not been fully established. There were typically two common techniques for polarization induction of PVDF films: electrode and corona poling. Figure 1.27 showed the schematic diagram of the electrode poling system. The conducting electrodes (top and bottom), which were either evaporated, sputtered, or painted on the PVDF film surfaces, were required for poling process. An electric field was produced across the sample when the voltage potential was applied to the electrodes. The poling can be done in air without arcing provided that the electrodes did not reach the edge of the film. Otherwise the PVDF film

might need to be placed in a vacuum or submerged in an insulating fluid such as Silicone oil, which can prevent arcing that will damage the material. Either static or sinusoidal electric fields at low frequency (mHz) can be applied to the sample during electrode poling. A constant electric field was hold on the sample from 10-30 minutes up to 2 hours. A variable field could reduce the probability of dielectric breakdown caused by high voltages for a prolonged period of time.

The study of polarization process in PVDF is still quite empirical, because a thorough understanding of the physical processes involved in this process has not yet been fully established. There are two most commonly used polarization techniques for PVDF films: electrode polarization and corona polarization. Figure 1.27 shows the process of conventional electrode polarization. In this process, it is necessary to sputter or paint a layer of conductive electrodes on the upper and lower surfaces of PVDF films. When the applied voltage is applied on the electrode, an electric field is generated in the direction of the sample thickness. In general, PVDF films may need to be placed in insulating fluids, such as silicone oil, to prevent arcs that damage the material. In the process of polarization, the static or sinusoidal electric field of low frequency (mHz) can also be applied to the sample. At this moment, a constant electric field is applied to the sample, ranging from 10-30 MV/m (and polarization time of about 2 hours). This kind of AC electric field can reduce the possibility of dielectric breakdown caused by high voltage for a long time.

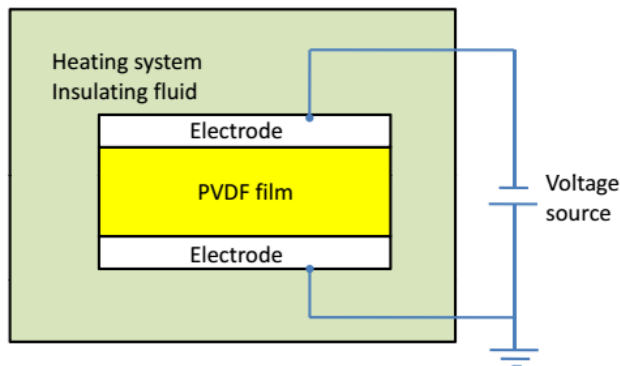


Figure 1.26 Schematic of the electrode poling system

The process of corona polarization is shown in Figure 1.28. At first, the bottom of the film with electrodes is placed on the heating plate and grounded. The corona tip is suspended above the

sample and applied up to (8-10 kV) voltage. Metal grids are usually placed at a distance of 3-4 mm above the sample to control the electric field near the sample surface. When the corona discharge mechanism is stimulated, the ionized particles emit from the corona tip downward and deposit on the top surface of the sample, forming an electric field between the top surface and the ground. Corona polarization can be effectively applied to large area surface polarization. The disadvantage is that it is more difficult to set up and optimize equipment than direct electrode polarization, and more in-depth research is needed.

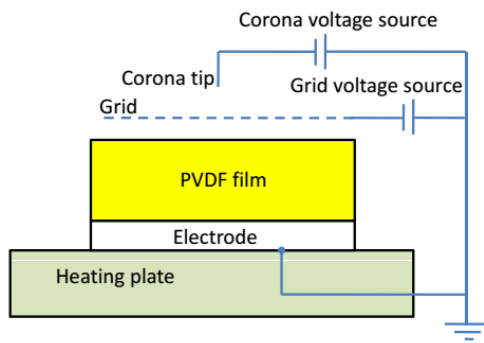


Figure 1.27 Schematic of the corona poling system

The magnitude of the electric field and sample temperature were the key for the poling process. Generally speaking, the higher the applied electric field, the higher the induced polarization provided that the poling field was larger than the coercive field of PVDF. The coercive field for PVDF and its copolymers was generally between 50 and 120 MV/m. An elevated temperature in the range of 85-130°C improved dipole mobility and hence increased the material polarizability. In order to allow polymer chains to align and reorganize, the polymer is held at high temperature during stretching and poling⁷². It should be noted that, although the high temperature can promote the polarization, it will also reduce the $\beta\%$, and eventually weaken the piezoelectric performance of PVDF.

The electric field and sample temperature are the main parameters in the polarization process. Generally speaking, the higher the applied electric field, the higher the degree of induced polarization. The coercive force of PVDF and its copolymers is generally between 50 and 120

MV/m. The increase of temperature in the range of 85-130 °C⁷² improves the fluidity of dipole and the polarizability of material. In order to align and reorganize polymer chains, polymers are kept at high temperatures during stretching and stretching, and after polarization, the temperature needs to be rapidly lowered to lock the orientation of domains. It should be noted that although high temperature can promote polarization, it will also reduce the piezoelectric properties of PVDF, and ultimately reduce its piezoelectric properties.

1.5.4. The state of art in printed PVDF sensors/actuators

Basically, the current printing technology used for PVDF can be divided into two categories.

Melt process

Melt printing usually includes FDM and FFF. With these methods, fibers and films are produced. In the printing process, the PVDF material is first melted and then extruded from the nozzle. In most cases, in situ poling is also used to induce beta phase. Even so, samples printed in melt usually have lower piezoelectric properties. As far as the author knows, the samples produced by these methods have not obtained any useful applications of sensors.

For instance, Lee et al.⁷¹ studied the manufacture of Electro-poling assistant additives (EPAM) using PVDF. By applying a voltage to the hot end of a 3D printer during extrusion, Lee's team was able to obtain individual piezoelectric PVDF stretching fibers that measured piezoelectric properties when bent.

Chang et al.⁷³ demonstrated the fabrication of piezoelectric polyvinyl fluoride (PVDF) nanogenerators by near field electrospinning (NFES) direct writing. In this study, when the external strain on a single electrospun PVDF nanofiber of 0.092% was applied, a repeatable and uniform output voltage of up to 8.5 mV is generated.

In the work of Porter et al.⁷⁴, the effects of fused filament fabrication (FFF) routine parameters on printed PVDF film properties were investigated using a variety of experimental methods.

While all 'as printed' films demonstrated little to no measurable piezoelectricity, PVDF films printed with a high β -phase content and subjected to a post-printing corona poling procedure showed a small, but consistent piezoelectric response. Based on a static deflection cantilever beam experiment, the d_{31} coefficient of the poled specimens was estimated at 1.19 pm/V.

In the work of Porter et al. ⁷⁴, the effects of conventional parameters on the properties of printed PVDF films in melt filament fabrication (FFF) were studied by various experimental methods. Although "all printed" films exhibit little or no measurable piezoelectric properties, printed PVDF films exhibit high beta phase content and showed a small but repeatable piezoelectric response after corona polarization. The piezoelectric coefficient of d_{31} can be estimated to be 1.19 pm/V by static deflection cantilever beam test.

Solution process

Among all these AM technologies, inkjet printing has the best application prospects due to its low cost and easy operation ⁷⁵. Electrospinning is a very important inkjet printing process. Its basic physical process is to produce polymer fibers with diameters ranging from nanometer to micrometer from melt or polymer solution. When the applied electric field is applied to the ink solution, the charged polymer solution will form conical droplets at the tip of the nozzle. If the electrostatic force of the electric field is sufficient to overcome the surface tension of the solution droplets, the droplets will eject onto the grounded metal plate. The solvent then evaporates and solidifies on the substrate to form a dry superfine fiber.

This technology has been so versatile in material selection and ease of processing that it can also provide a unique way to improve the performance of various materials. In addition, electrospinning technology has great applications in various fields such as filtration, biological scaffolds and medical implants. In recent years, electrospinning technology has also been applied to the fabrication of sensors, actuators and other micro-devices. According to its physical process, electrospinning can be divided into far-field and near-field processes. The latter is used more in the manufacture of sensor actuators ⁷⁶. PVDF produced by inkjet method usually has high piezoelectric coefficient and has been applied to sensors and energy collectors ⁷⁷.

Yee et al. demonstrated the feasibility of using far-field electrospinning (FFES) and a rotating disk to collect aligned electrospun PVDF fibers⁷⁸. Fennessey⁷⁹ investigated different techniques to align electrospun fibers using a rotating collector. Wang⁸⁰ modified the electric field for better alignments and the application of fundamental physics and chemistry for better process controls⁸¹.

Yee et al. demonstrated the use of far field electrospinning (FFES) and rotating disc to collect and align PVDF fibers⁷⁸. Fennessey et al.⁷⁹ studied different techniques for aligning electrospun fibers with rotary collectors. In order to achieve better alignment and basic physical and chemical properties, the electric field distribution was modified to achieve better process control in this study.

Unlike FFES, NFES can continuously produce fine fibers with only a small bias voltage⁸². Under in-situ electrochemical process, PVDF polymer can be converted from non-polar α phase to polar β -phase⁷⁷. However, the breakdown voltage of air is $\sim 106 \text{ V m}^{-1}$, which is too low for the polarization process - and if a layer of polymer film is used instead of air, a higher electric field can be applied to achieve better polarization process. In order to prevent the possible short circuit in the process of electrospinning⁸³, it was considered to deposited on the glass tube. The rotating tangential velocity is 400 mm s^{-1} , and the mechanical stretching effect can also be realized on the glass tube collector. Compared with commercial PVDF films, the PVDF fibers produced by this method are even better than commercial PVDF films in terms of expansibility, flexibility and piezoelectricity (for fibers: $d_{33} \sim -57.6 \text{ pm V}^{-1}$; $g_{33} \sim -400 \times 10^{-3} \text{ V m N}^{-1}$; for thin films: $d_{33} \sim -15 \text{ pm V}^{-1}$; $g_{33} \sim -308 \times 10^{-3} \text{ V m N}^{-1}$)⁸⁴.

Progresses on all-printed sensors

Zirkl et al.⁸⁵ manufactured a full print sensor consisting of various electronic components. In this study, pressure and temperature sensitive sensors, organic transistors and electrochromic displays were printed respectively and integrated on a flexible substrate. Only five printing inks were used: PEDOT: PEDDS, carbon, P (VDF-TrFE) solution, electrolyte and SU-8. The printed device has been demonstrated to be practical and can be used in touch keyboards, projection

screens controlled by laser waves, electronic skin and etc.

It is undoubtedly an attractive goal to develop a printable material system with piezoelectric characteristics and to fabricate and implant sensors in one-step printing process without polarization, which is of great significance for the creation of various intelligent structures. Barium titanate doped PVDF films were prepared by solvent evaporation assisted 3D printing at room temperature by Bodkhe et al ⁸⁶. In this work, without polarization and tension, a 3D contact sensor with d_{31} up to 18pC/N was obtained. Subsequently, through printing technology, a fully functional 3D printing sensor was obtained, which can produce up to 4 V maximum voltage output when finger tapping.

1.5.5. Motivation and challenges

The development in situ health monitoring technology require the fabrication of better embedded smart sensor system. As ‘all-printed’ sensors come up, the AM technology is becoming a powerful tool to address this problem. One critical issue is to find the appropriate material and design the process accordingly. The large piezoelectric effect, high flexibility, low price etc... reported for PVDF suggested that it be a leading candidate for the issue.

However, the complicated phases and microstructures in PVDF set a very hard demand in procedure control to obtain the piezoelectric β phase. For the PVDF used as the polymeric piezoelectric material, the processing condition may not only affect the resulting sensitivity of the embedded sensor, it will even produce the phases that have no piezoelectricity. Also, a comprehensible post-printing process need to be carefully developed to achieve the functionally integrated smart structure with the optimal sensing performance and sensitivity.

The objective of this research, therefore, was to investigate the phase transformation mechanism and enable the direct printing of β phase PVDF with high sensitivity. To improve the performance of PVDF-based piezoelectric sensor, the processing procedures needed to be carefully identified and selected to achieve the optimized piezoelectric constant for the best sensitivity in structural health monitoring. This research will incorporate novel additive

manufacturing process, sensor fabrication, and microstructure control into a new framework that enables smart embedded sensor networks for on-line diagnosis/prognosis of the integrity of in-service structures.

Quenching of the sample should help to form more beta phases, but it may also cause warpage of the film due to the expansion value of high thermal coefficient. The stretching required for phase transformation is also a difficult problem for printing process, because it needs to be integrated into a multi-component system with different materials, which will vary greatly in geometry and performance. It should be noted that the copolymer P (VDF-TrFe) has a high beta phase stability during solidification, and piezoelectric phase can be formed without the help of tensile effect. It has been successfully applied to inkjet printing⁸⁷ and spin casting⁸⁸ sensors/actuators. The greatest disadvantage of this copolymer is its high cost, which is currently about \$4,600 (Piezo Tech, Arkema). In contrast, the 10-pound Kynar 740 from Trident Plastics in Pennsylvania costs just \$300 (or \$66). The high cost limits the material in larger and more widespread applications.

At the very beginning we found it extremely difficult to duplicate the published results in other labs. Then we found the β phase in the sample was very sensitive to any minor change of experiment conditions. In order to obtain the beta phase in PVDF, the experimental conditions should be highly controlled. Even the change in the relative humidity can influence the results. And because previous methods to fabricate the β phase PVDF are based on the empirical results, we don't know what effect is decisive, which lead to a low repeatability in our experiment. It may be helpful to take full advantage of previous result to advance our current processing. But how? If we're not able to find the real cause which can induce the β phase. What the researchers faced was a massive amount of parameter work to conduct, because it is difficult to tell which factor is valid one. And because the goal is to create the all printed smart structure. We are also going to study how to maintain its piezoelectric performance during the post step including the post printing process and the curing process of both matrix material and conductive materials. We should know the influence of this post printing process on the stability of beta phase. And in order to realize the all printed smart layer structure, we also want to integrate those process into the printing platform. All these challenges demand a new fundamental understanding on the

formation and the stability of β phase PVDF.

Based on the discussion above, the fundamental questions thereby, to be answered are:

- (1) How can we control the conformation of PVDF film in AM processing to obtain optimized piezoelectric and to promote the sensitivity of PVDF sensors?
- (2) How can we maintain the β phase and piezoelectric property during the following steps in printing of other components of the smart structures? And is it possible to incorporate the post printing process (including heat treatment and poling etc...) into the printing platform?
- (3) And how to design, model and fabricate the sensor system for in-situ SHM application?

1.6. Scope of thesis

The goal of this study is to characterize the piezoelectric sensing and actuation performance of printed PVDF thin films for eventual use in SHM. This piezoelectric thin film acts as a transducer with enhanced piezoelectricity. Those enhanced properties come from the integration of printing process and the polarization. Sensing properties are validated, and guided wave-based SHM is also demonstrated.

The main purpose of this study was to investigate the different parameters of AM process and to evaluate and balance the different effects of different technologies and materials on performance. A new multi-material and multi-scale additive manufacturing method was used to develop an embedded polymer piezoelectric sensor and an intelligent structure based on the sensor, which can be used for on-site structural health monitoring. In the Chapter 2, the basic principle of beta phase transition in PVDF was systematically discussed, and a new mechanism was proposed. It will be validated from a theoretical point of view and previous results of other groups. In the Chapter 3, the parameters of PVDF films were introduced in detail. The basic piezoelectric properties of different process fibers were characterized by X-ray diffraction (XRD) and Fourier transform infrared (FTIR) characterization tools etc. The effects of temperature, voltage and solvent on the $\beta\%$ and crystallinity of the films were discussed in detail. Chapter 4 discussed the

polarization process, the special electret structure brought about by EHD printing and the high electrostrictive coefficient of printed PVDF films. Chapter 5 introduced the theoretical design and analysis of sensor based on PVDF. The concept verification of PVDF sensor manufacturing was proposed. It also illustrated the potential application of this printed PVDF in SHM. Chapter 6 summarized the results and puts forward the future work.

2. Mechanisms of PVDF α to β phase transformation in printing process

The key for the fabrication of PVDF piezoelectric thin film was to control the formation of β phase. There were two major barriers for us to apply the AM technology in this area:

Firstly, it was almost impossible to finish the α to β transformation without stretching for the pure PVDF. And this transformation was so sensitive to the processing conditions that any minor adjustment on processing parameters could lead to the reverse of the transformation. However, the greatest advantage for AM technology was its flexibility and AM technology usually need to face some changes (substrate, temperature, humidity, etc...) in varied occasions. Traditionally, the PVDF sensors were firstly processed in a clean room, and then were cut and mounted on the structure. The processing condition can be easily controlled. But if the task was to directly embed the sensor structure, the processing condition cannot be precisely controlled. It was difficult to apply the stretching and poling in printing. The heat treatment required for silver traces could also bring about detrimental influence on the β phase that need to be evaluated.

Secondly, the goal for this study was not to produce the PVDF piezoelectric materials in a well-controlled, constant condition, instead it was needed to develop the manufacturing technology in every kinds of complicated conditions, combined with different matrix and electrodes. It was also needed to integrate several kinds of conventional technologies into our printing platform. The poling process was required for any piezoelectric materials. In order to print the piezoelectric sensor into the embedded structure, and obtain the enough sensitivity for SHM, the poling process need to be considered. So far, it had never been reported that the poling process can be completed on the AM platform. The poling, as well as other post printing process could lead to the change of phase composition and microstructure of PVDF. These all required us to know more about this material.

Before the specifics of the experiment can be presented, a brief introduction of a new mechanism

for the α to β transformation was given. This chapter presented a theoretic model, a simple model with electromechanical coupling based on Gibbs free energy. At the beginning, this mechanism was proposed specifically for the manufacturing by solvent methods. Additionally, a general explanation of the current processing with respect to the various types of manufacturing methods was also provided. a general explanation of the current processing for piezoelectric PVDF material was given. Finally, the strategy for how to promote the β phase content and crystallinity based on this mechanism was discussed.

2.1.The structural foundation of the proposed mechanism

The structure of the material can be observed at many levels. First, as discussed earlier, PVDF is composed of many identical monomers. Each monomer unit is a CF_2CH_2 fragment, as shown in Figure 2.1. These monomers are the basic repetitive units of PVDF. The molecular weight of PVDF is about 100,000 g/mol, which is equivalent to 2,000 monomers. The average chain length of PVDF is 0.5×10^{-4} cm ($0.5 \mu\text{m}$)⁸⁹. The dipole moment of each monomer unit is 7.56×10^{-30} C-m⁹⁰.

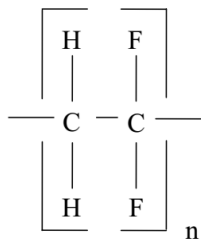


Figure 2.1 The monomer of Polyvinylidene fluoride molecule.

2.1.1. Monomers

The structure of materials can be observed from multiple levels of perspective. Firstly, as discussed before, PVDF was composed by many identical monomers. Each monomer unit is a CF_2CH_2 molecule shown in Figure 2.1. These monomers was the elementary repeat units of PVDF and they were chemically linked to create chains during the polymerization process. The

molecular weight of PVDF was about 100,000 g/mol corresponding to 2,000 monomers or an extended length of 0.5×10^{-4} cm ($0.5 \mu\text{m}$)⁸⁹. Each monomer unit had a dipole moment of 7.56×10^{-30} C-m or 2.27 D⁹⁰.

From the monomer point of view, there are two basic types of units in PVDF and its copolymers: G (Gauche) and T (Trans), as discussed in section 1.4.3. G represents an oblique angle between the chemical bond and the backbone plane of the carbon chain. Each G + or G - bond represents an angle of 60° or -60° degrees between the plane and the plane, respectively. The repetitive structure containing G + or G - will produce a right or left helix. The structure with alternating G + and G - creates an incomplete helical structure, and changes the helical direction with alternating G bond ⁹¹.

2.1.2. Chain Conformations

Carbon chain conformation represents another level of perspective, which represents the different arrangement of monomers on a single carbon chain. In melt or solution, polymer chains are randomly coiled in shape (configuration), in which disordered macromolecules remain solid; however, chains without configuration defects can also crystallize into regular conformations and maintain this conformation by cooling from the melt. This is achieved by rotating around a single chemical bond by minimizing the potential energy of the chain generated by the internal steric hindrance and electrostatic interaction. The preferred rotation angle in energy is 180° to each other (T monomer) or at 60° (G monomer); of course, the actual torsion angle usually deviates from these values to some extent. Strictly speaking, we can find numerous carbon chain configurations because there are numerous ways to arrange thousands of monomers in PVDF composed of a chain of 'G' and 'T'.

The three best known and most important conformations of PVDF are All-Trans, TG+TG- and TTTG+TTTG-. The first two conformations are the most common and discussed in this study, as detailed in Figure 2.2. Because all dipoles are aligned in the same direction as the normal of carbon chain axis, total inversion is the highest polar configuration in PVDF, resulting in the highest piezoelectric structure ^{38, 90}. The arrangement of TG + TG - is also polar, but due to the

dipole tilt to the molecular axis, it has a net dipole moment perpendicular to and parallel to the chain. When the TG+TG- configuration is combined into alpha phase, the polarity will disappear completely because the dipoles of adjacent carbon chains cancel each other out. Other conformations, such as TTTG, also have slight polarity, but their piezoelectric properties are much lower, so their applications are limited. The process conditions for obtaining specific configurations depend to a large extent on the processing, thermal and mechanical treatments that the polymer undergoes, and the relationship between these treatments and the formation mechanism of carbon chain configurations will be discussed in detail in the following parts of this Chapter.

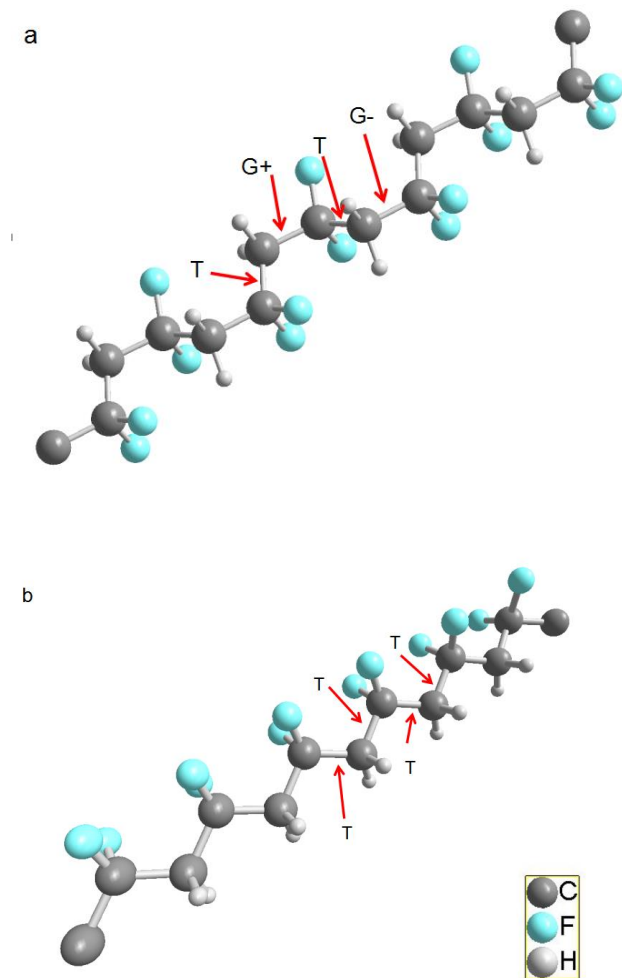


Figure 2.2 Diagrams of (a) α -phase and (b) β -phase chain conformations in PVDF

It was also shown in Figure 2.3 that the fluorine atoms are always on the same side of an carbon

bone chain, and in the meantime, all of the hydrogen bonding on the other side. Due to the great difference on electronegativity between fluorine atoms and hydrogen atoms, electrical dipoles are produced perpendicular to the chain direction. This is the origin of piezoelectricity in beta phase PVDF. The production of dipoles in TTTT chain conformation were shown clearer in Figure 2.3 below. In fact, depending solely on the polarity in the polar configuration of PVDF is not enough to ensure the polarity of the crystal as a whole, because the dipole moments of the carbon chains in these lattices can cancel each other out according to their arrangement. Although the chain conformation provides the possibility of piezoelectricity in PVDF, the real performance is ultimately decided by its crystal phase structure that will be discussed in the following subsection.

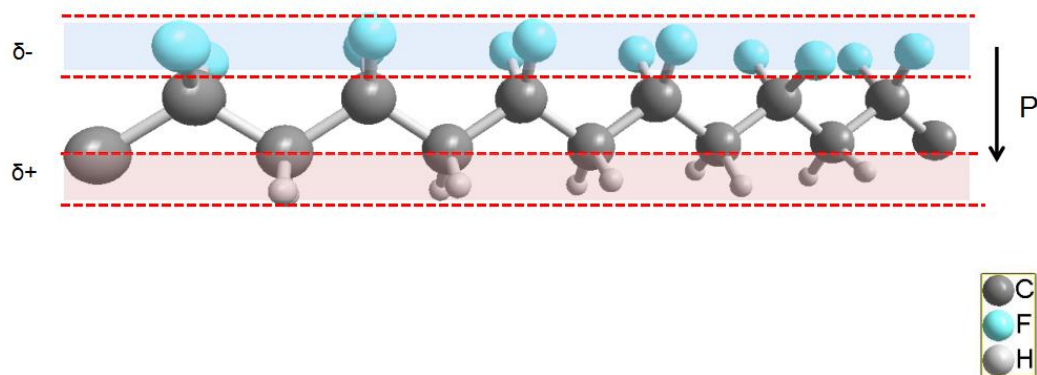


Figure 2.3 The introduction of dipole perpendicular to the chain direction of PVDF in TTTT conformation

2.1.3. Phases

From this level of perspective, there are two basic states of existence for PVDF: the amorphous state and crystal state. In amorphous state, the chain may exist in any conformations. In crystal state, there are four phases that are most frequently reported: α , β , γ , δ . As shown in Figure 2.4 below, each phase corresponds to one specific chain conformations.

Among all of the phases, α phase with alternative (TG^+TG^-) conformation is the most energetic favorable and constant. Strictly speaking, the TG^+TG^- conformation of α phase is also polar, but

because of the inclination of dipoles to the molecular axis, it has components of the net moment both perpendicular and parallel to the chain³⁸. We have introduced previously that the ability of molecules of PVDF to adopt polar conformations is not enough to ensure polarity of the whole crystals, for these molecules may be crystallographically packed in a lattice canceling each other's moment. For instance, the most common PVDF conformation, the TG+TG- conformation in the alpha phase, is exactly the case. As shown in Figure 2.4 (c), the unit units of the alpha-phase lattice consist of two chains arranged parallel in TG+TG- and their dipole moment components are inversely parallel to the normal of the chain axis, thus canceling each other out. Although the dipole moment of the TG+TG- chain in the alpha unit cancels in the crystal, the second chain can be rotated 180 degrees around its axis to obtain the polar phase by applying a high electric field to the sample. At this point, the crystal is actually transformed into a polar δ phase.

A simple close stacking of all trans TTTT configurations results in the formation of beta phase. As mentioned above, the beta phase of PVDF has the best piezoelectric properties, which can be obtained at specific temperature and polarization conditions. The crystal structure has the largest dipole moment arrangement, which makes the polymer have strong piezoelectric properties. In beta-phase PVDF, the packing of chains makes the fluorine and hydrogen atoms of adjacent chains roughly at the same level as the a-axis in the lattice cell, and this intermolecular force, which is very beneficial to the potential energy, plays an important role in the stability of the crystal structure.

The carbon chains of TTTG + TTTG - configuration are stacked in polar manner, resulting in the gamma phase crystalline state of PVDF. Its lattice cell has almost the same lattice constant as its alpha cell (Fig. 3a). This fact makes the transition from alpha PVDF to a more stable γ phase require only a limited intramolecular movement. Nonpolar morphology of γ phase PVDF has also been reported in some literatures, but this morphology may only exist in phase mixtures obtained at very high temperatures.

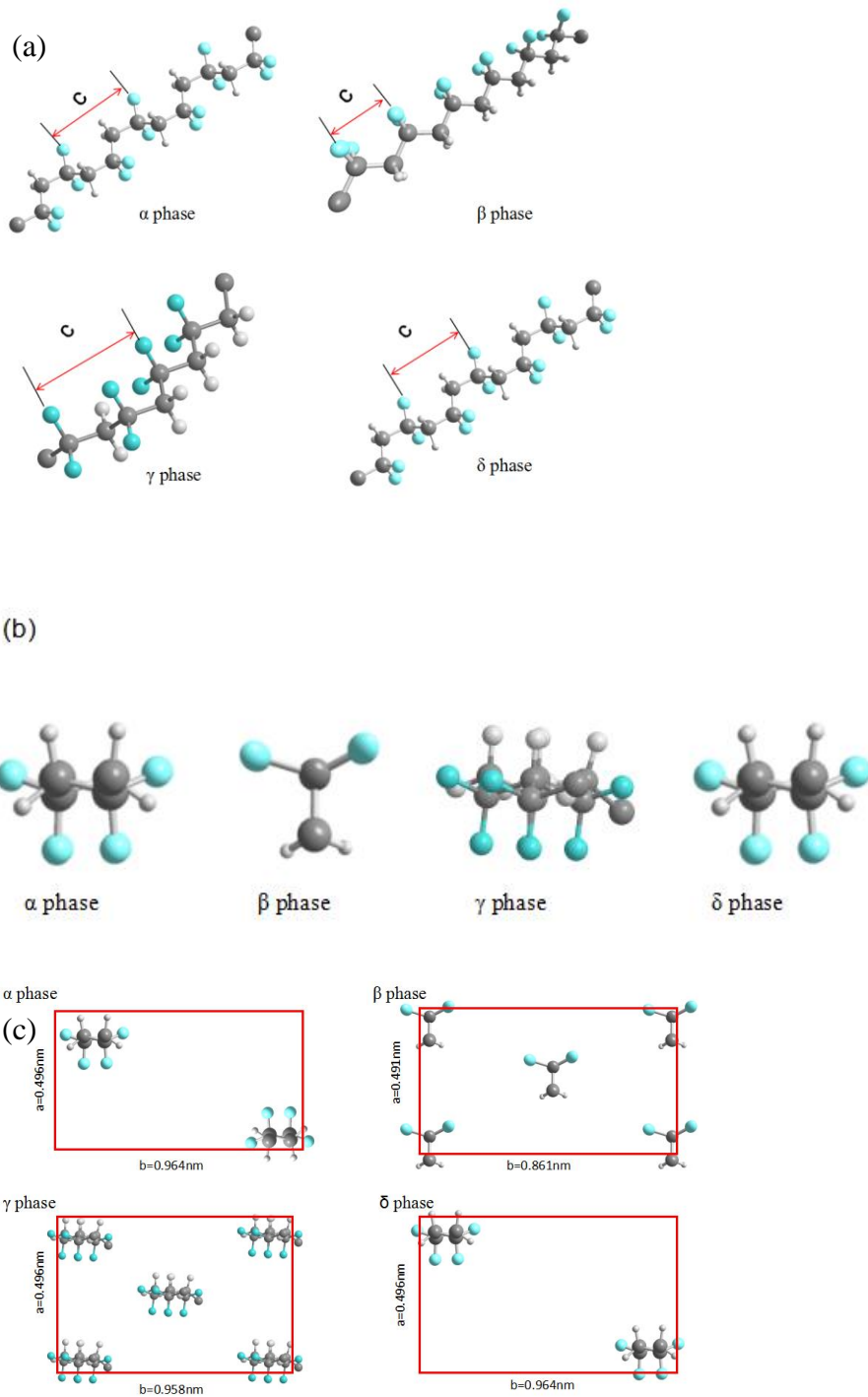


Figure 2.4 (a) The conformation structure of $\alpha, \beta, \gamma, \delta$ phases in PVDF respectively; (b) the atom arrangement of $\alpha, \beta, \gamma, \delta$ conformation along the view of chain direction; (c) the lattice plane of $\alpha, \beta, \gamma, \delta$ phase perpendicular to the chain direction.

So far, we have seen that single polar crystals can be produced by stacking polar carbon chains.

Dipoles in carbon chains can be accumulated in some way until macro polarity is generated in the crystals and grains. However, polymer crystals are very small. When crystals start to grow and grow from the melt and form spherically symmetrical polycrystalline aggregates, there is generally no net dipole moment in this process. These aggregates, known as pellets, are products of the nucleation of primary crystals in the melt and the radial outward growth of the nuclei. PVDF melts at ~170 to 200°C. When it is cooled from the melt, it usually crystallizes in the form of non-polar alpha-phase pellets. At higher crystallization temperature, gamma spherulites are also obtained. The β phase is usually obtained by mechanical deformation combined with polarization rather than by direct melt cooling (which requires high pressure or by epitaxial growth technology), as described earlier. Figure 2.5 shows the microstructures of typical spherulites of PVDF. The microstructures show radial stacking in the optical microscope. In fact, the stacks that are called laminates are very thin (about 10 nanometers thick and several microns in transverse dimensions). These lamellae are composed of macromolecular carbon chains, and the amorphous region shown in the figure also contains carbon chains in disordered conformations; this solid two-phase structure is a typical form of crystallizable polymers. In PVDF, the spherulites formed by the crystalline lamellae account for about 50% of the total mass, and the other half are molecular chains in amorphous form. In conclusion, our research on the structure of PVDF shows that even though some polymers can form polar crystals, the three-dimensional arrangement of spherulites in macroscopic samples will lead to macroscopic polarity offset. In order to overcome this, the spherulite rearrangement must be induced by polarization, so that the whole crystal will obtain its polarity.

In a word, different carbon chain configurations can form specific crystalline phases corresponding to them. We have never obtained a complete PVDF crystal. Instead, as shown in the figure below, the spherical layered crystal structure coexists with the amorphous part of the two-phase structure. Within the spherulite, the radial fibrous crystal structure of PVDF has also been observed in early microscopic images, including very thin, lamellar crystalline parts and amorphous regions that separate different lamellae from each other. The crystalline plates are stacked with polymer carbon chains, which are several nanometers thick and several micrometers in transverse dimension. Because of its physical properties and the fact that the laminates are surrounded by an amorphous structure, it is often referred to as supercooled liquid

phase. Each PVDF radial fiber extends outward from the central region through several crystalline and amorphous regions as shown in Figure 2.5.

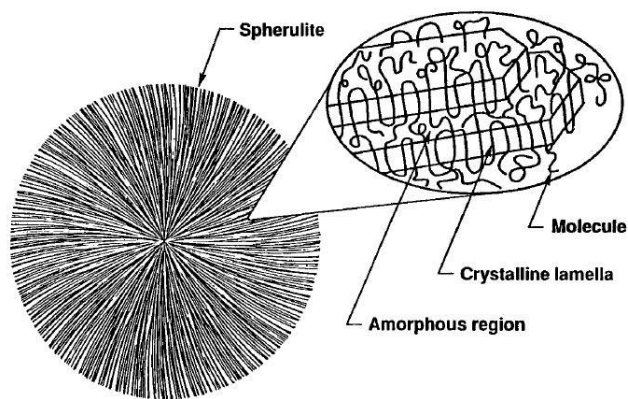


Figure 2.5 The two-phase structure of PVDF³⁸.

In conclusion, the crystal structure must satisfy two conditions in order to obtain the materials with piezoelectric and pyroelectric properties which can be applied in engineering practice: 1. The crystal structure should have non-zero net dipole moment; 2. All crystal dipoles in macroscopic samples should have a certain preferred direction of ⁵³. In order to meet the first requirement, PVDF needs to obtain the polar beta phase microstructures by mechanical deformation, applied electric field, heat treatment ^{92, 93}, and crystal epitaxy growth. In order to meet the second requirement, all materials need to undergo the polarization process of applied electric field.

2.2. The analysis of the basic G→T transition

The whole mechanism was based on the most basic and simple change in monomer structure. It was easy to observe that the G and T status are interchangeable through the rotation of the C-C bonding as shown in the Figure below. Because of the steric hindrance, the Cs (the back atoms on the figure) on the carbon chain backbone tend to stand away from each other's. Thus the T status should have a little lower internal energy compared with the G status. During the procedure of G-T transition, there is an intermediate status that the position of atoms bonding to the adjacent carbons will overlap. This inevitably will produce huge steric hindrance in the structure. As a result, this intermediate status would have a much higher internal energy than both of G and T status. And the energy difference between this intermediate status and G (or T) status is the energy barrier that must be overcome for the transition to occur.

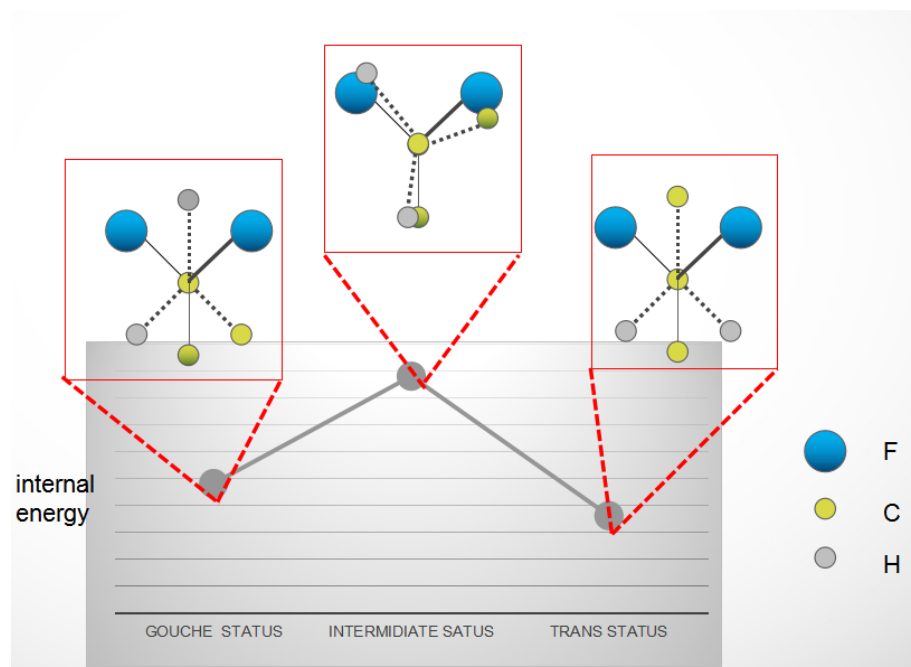


Figure 2.6 The transition procedure of G and T status through the rotation of C-C bonding

It was already discussed about the different arrangement of this monomer on C-C chain can form different conformations (TTTT, TGTG, etc...). Since the individual monomer was interchangeable through the rotation of C-C bond, the whole conformation can also transmit into other configurations through the cooperative rotation of multiple monomers under certain

conditions. In the last section, it has been pointed out that each crystal phase has its corresponding chain conformation. And with the crystallization and close-packing, the conformation formed the crystal phases. Besides, if it is possible to complete the transformation through the simple rotation of C-C bonding, this transformation would not occur through other ways that need the break of the chemical bonding. Because the energy barrier would be several magnitude higher. At last, a preliminary but critical conclusion can be obtained that the crystal phase transformation of PVDF was realized through the simple rotation of C-C bond inside a monomer.

The above analysis was still a pure theoretical description. The effect in real processing was much more complicated. Other possible mechanism and the driving force of this bonding rotation need to be furtherly discussed.

2.3. Central hypothesis: Physical process or Chemical process?

In previous studies, authors realized the critical role of the β phase formation on the piezoelectric performance in PVDF. In order to obtain higher β phase content, researchers have done a lot of work. Some authors have studied the optimum conditions for such conversion, as well as the mechanisms and possible factors affecting these conditions. Firstly, the beta phase transition is induced by the strong stretching effect of the PVDF ejector during the processing. Secondly, the external electric field plays an important role in the formation of beta phase. Thirdly, the rapid evaporation of solvents and the condensation of PVDF fibers may also affect the transition from α -phase to β -phase.

Most of these results were imperial, which meant the focus of those works were to find the optimized experimental conditions to induce the $\alpha \rightarrow \beta$ phase transformation. It was automatically considered this transformation as a common physical process, just like most solid-state transformations in metals and ceramics. In fact, most transformation in metals or ceramics such as martensite transformation was physical process, because there was no change inside

molecular/atoms during the transformation. In physical process, researchers usually applied the models like nuclear formation and growth to describe the procedure of phase transformation: In the form of melt or solvent, the molecular chain of PVDF has no fixed structure and can move or rotate freely. At cooling time, as the melt solidifies, the molecular chain of PVDF crystallizes into spherulites and radiates outward from the nucleation point. Actually, some PVDF was observed to crystallize in this way especially in the α and γ phase conformations. In fact, this view can explain some phenomenon and looked reasonable at first glance. However, it ignored the relationship of chain conformation and crystal phase. And if treated in this way, it was still difficult to find the decisive effect on the β phase formation mechanism and build the theoretical connection between the processing parameters and the driving force of the phase transformation from this model.

The proposed mechanism didn't deny the occurrence of physical procedure during the phase transformation, it just pointed out that the physical procedure was not a dominant effect for the phase transformation. On the contrary, a mediate state of free chain conformation was introduced, and the real decisive effect was considered as the rotation inside this chain conformation. And since the whole Carbon chain can be consider as a huge molecule, the change inside this "molecule" was consequently denoted as a chemical process. Obviously, the distinction of α and β phase of PVDF did not only exist in their crystal state but also in their amorphous and solvent states.

Observing the condition in our ink jet printing process, the proposed chemical procedure will be clearer: the PVDF chain dissolved in liquid solvent, the chain conformation transition can freely occur through the rotation of C-C bonding. After the TG+TG- chain transformed to TTTT chain, the chain packed and formed the β phase. Other effects, especially the crystal lattice energy in solid state, can be ignored in this situation. And considering the whole chain as a huge "molecular", the phase transformation mainly happened inside the molecular, as a result, can be analyzed as a chemical procedure. For the calculation of the driving force for a chemical procedure, the most convenient theoretical tool was the Gibbs-Helmholtz equation. It was easy to find from the previous discussion that the Gauche monomer can transform to Trans monomer by rotation along the C-C bond. So, the whole chain conformation transformation can be understood by the combination all of those rotations. Here one may ask what factors that decide the rotation

direction, and the direction of the transformation. As a chemical process, the answer is clear, the Gibbs free energy difference of the chain conformations. It was necessary to propose the basic hypothesis before the discussion of Gibbs free energy in detail. The major hypothesis for the proposed phase transformation mechanism can be concluded as below:

- 1. In the solution process for this study, the phases of PVDF is decided by its chain conformation.
- 2. Although the β phase is a crystal phase. The fundamental cause of β phase lies in its chain formation transformation (chemical process) instead of its crystallization process (physical process).
- 3. The chain formation transformation is attained by rotating along the C-C bonding of the chain.
- 4. The direction of chain transformation is decided by the thermodynamic state of the material, which can be controlled by the temperature field, stress field and electrical field during the processing.

2.4. Development of Gibbs energy under stress field and electrical field

The extended Gibbs-Helmholtz equation was first proposed by Landau in the 1930s. The purpose of this equation was to study various complex physical problems in solid-state transformation, especially the ordered transformation in metal alloys. Since then, Landau theory had been successfully used to describe and calculate the phase transition processes related to these parameters in various material systems, including ferromagnetic system, martensite (ferroelastomer) and ferroelectric phase transition. For example, appropriate ferroelectric, ferromagnetic and ferroelastic phase transitions can be described and calculated by Landau potential with the order parameters of polarizability P_i , susceptibility M_i or self-strain, respectively. Ginzburg³² completes the extended application of Landau theory to ferroelectric phase transition. In his study, the effects of spatial inhomogeneous thermal fluctuations near phase transition are included. He introduced what was then called correlation length to define the

limited region of polarization fluctuations. In this way, Landau theory was further developed into the so-called Landau-Ginzburg-Devonshire (LGD) thermodynamic theory of ferroelectric phase transformations to study the various physical properties of ferroelectrics.

The Gibbs energy density contribution due to an applied field is simply given by

$$\Delta G(P) = E \cdot P$$

where \mathbf{E} is the electric field along the polarization direction; \mathbf{P} is polarization of the material.

The Gibbs energy contribution due to an applied stress is simply given by

$$\Delta G(\varepsilon) = \sigma \cdot \varepsilon$$

where σ is the applied field, ε is the strain during the solid-state phase transformation.

The chemical energy and the contribution of temperature T were already given in classic Gibbs-Helmholtz equation. With the combination of classic Gibbs-Helmholtz equation, and the energy contribution of applied electrical field and stress field, we proposed an extended Gibbs-Helmholtz equation as below:

$$G(T, \sigma, E) = U - T\eta - \sigma \cdot \varepsilon - E \cdot P, \quad (2.1)$$

in which U is the internal energy, differentiation of Eq. (2.1) yields

$$dG(T, \sigma, E) = -\eta dT - \varepsilon \cdot d\sigma - E \cdot dP, \quad (2.2)$$

U- internal energy (J/mol);

T- temperature (K);

η - entropy (J/K·mol)

σ - applied stress (Pa)

ε - the strain produced by the transformation (1)

E -electrical field (V/m)

P -polarization (C m)

This extended Gibbs-Helmholtz equation was the focus of this chapter. Using this equation, a clear relation can be obtained among the Gibbs free energy with temperature, stress and electrical field, all of which were the critical factors in PVDF processes. Before the detailed discussion of this equation, it was necessary to point out that this equation was different with the classic Gibbs-Helmholtz equation. In most chemical procedure, only the front two terms of equation (2.1) were important, other terms were usually ignored because compared with the chemical bonding energy, the other energy term was much lower. However, in our case, the composition and structure is so close for conformation alpha and beta, and the transformation only need the rotation of the chemical bond instead of break the chemical bond. Thus, the energy of last two term became comparable to the front two terms and became more important.

2.5. Verification and application of the proposed mechanism

In order to simplify the problem, this extended equation was mainly used to analyze the conformation transition $\alpha(\text{TG}^+\text{TG}^-) \rightarrow \beta(\text{TTTT})$, to avoid the analysis the influence of intrachain atoms and lattice energy. The Gibbs free energy (ΔG) represented the driving force for the transformation. When $\Delta G < 0$, the transformation would occur. And the transformed ratio $K = \beta/\alpha$ (wt%) can be calculated by:

$$\Delta G = -RT \ln K \quad (2.3)$$

R- molar gas constant

T- temperature (K)

This equation (2.3) combined with (2.1) can connect the transformation ratio with the critical processing parameters such as the temperature, electrical voltage, applied stress etc. The transformation ratio can be anticipated through the relation showed above. Thus made the quantitative or semi quantitative control of the phase transformation become possible. The lower value of Gibbs free energy obtained, the higher degree of conversion can be achieved.

On the other hand, equation (2.3) can also be used to verify the proposed mechanism via comparing and analyzing the processing condition and $\beta\%$ in reported studies from other groups.

It will be presented as below some case studies to show the basic idea and procedure of this verification.

Strictly speaking, the $\beta\%$ calculated above was the β (TTTT) content in chain conformation which included both amorphous and crystal states. The contents of one conformation were not necessarily the same in different states. And since PVDF's piezoelectric performance is primarily dependent on the percentage of crystalline β -phase in the films^{94, 95}, to enhance the crystallization was another important target for the optimized piezoelectric performance. The key desired outcome also included the polarized dipoles after the printing process. All of these were interconnected with the processing parameters. From here, it was demonstrated again why it was so important to understand the mechanism of β phase formation in the printing process. Parameters investigated included solvent selection, substrate temperature, voltage, and printing speed.

2.5.1. The term of internal energy

From the previous discussion, the structures of Trans (T) and Gauche (G) were demonstrated. In the spatial arrangement, Carbon bone chain is much larger than any single atoms. Thus Carbon atoms tend to stay away from each other. This phenomenon is called steric hindrance effect. It was pointed out previously $U(T) < U(G)$. From this point of view, U (TTTT) is lowest in all types of chain conformations. U (TG⁺TG⁻) is also low, its value should be close to U (TTTT) because this chain conformation has the most H-bonding between H and F atoms, which can dramatically reduce the internal energy of the chain. Only considering the internal energy, the transformation should automatically occur under any conditions. However, the internal energy of two conformations are quite close, it is very easy to be influenced by other effects.

The internal energy can generally be tailored by changing the chemical composition. Replacing one H atom in monomer with F atom to form the TrFE monomer, and replacing some original monomer with TrFE monomer, the copolymer P(VDF-TrFE) was produced. This replacement has very little influence on U (TTTT) but it will dramatically increase the U (TG⁺TG⁻) because the replacement of H atom with F atom in original monomer will break half of the H-bonding of the

conformation. Thus, it would bring an extra negative value of ΔU . The figure below showed the phase diagram of this copolymer.

In different PVDF copolymers containing trifluoroethylene or tetrafluoroethylene, ferroelectric behavior similar to that of β -PVDF can also be observed; these randomly added copolymers usually contain 60 to 80 mole percentages of VDF. In these copolymers, because they contain a larger proportion of fluorine atoms than PVDF, their molecular chains can not accommodate the alternative TG + TG - configuration, so they are forced to crystallize in an all-trans configuration, thus making the formation of ferroelectricity easier. The difference between PVDF and its copolymers also includes that the Curie temperature can be measured in these copolymers, but not in PVDF. This is because the Curie temperature of β -PVDF can not be measured because it is predicted by thermodynamics that the Curie temperature of β -PVDF is higher than 205 °C of its melting point. In these copolymers of PVDF, the ferroelectric transition phase is given a wide temperature range (30°C or more), so it can be observed below the melting point.

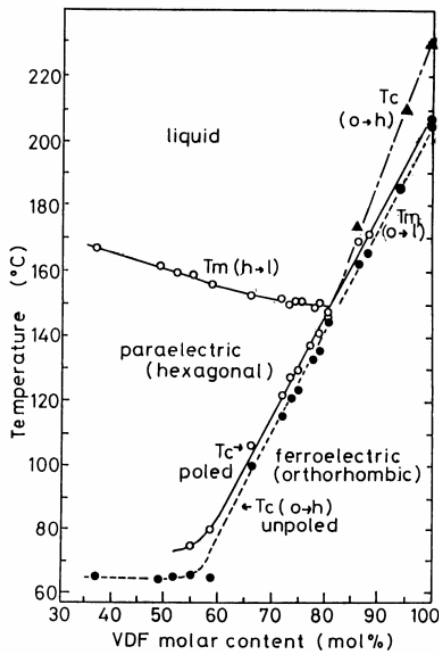


Figure 2.7 Phase diagram with respect to the VDF% of P(VDF-TrFE) at 1bar ⁴⁶.

The paraelectric phase in this diagram indicated the phase similar to α in PVDF, while

ferroelectric indicated β phase in PVDF. It was observed in this figure that the ferroelectric phase is more stable in low temperature. This result furtherly proved the view proposed previously that TTTT conformation had the lowest internal energy. When VDF% was below 60%, the area above 60°C were all paraelectric phase (α phase). With the further increase of the VDF% above 60%, beta start to take charge; when VDF% reached a value higher than 80%, there was only ferroelectric phase (β phase). This phenomenon agreed well with the conclusion in this subsection that replacement of TrFE can increase the internal energy of the TG^+TG^- conformation and thus promote the $\alpha \rightarrow \beta$ transformation. This characteristic made the P(VDF-TrFE) copolymer the most promising material for 3D printing piezoelectric sensors. Because the ferroelectric phase in P(VDF-TrFE) can be conveniently obtained and controlled as long as selecting the proper content of VDF monomer. Why PVDF was still selected as ink material in this study? The main concern is about cost and availability: at present, the price of PVDF (TrFE) is about \$4,600 per kg (PiezoTech, Arkema), whereas Kynar's price is only \$66 per kg (Trident Plastics, PA).⁷⁴ In order to extend the utilization of this 3D printed embed sensor technology, it was necessary to develop the material that is common and cheap. Besides the PVDF has higher dipole within the C-C chain, which could result in better piezoelectric properties than P(VDF-Trfe) with similar crystallinity.

2.5.2. The term of entropy

The second term on the right side of equation (2.3) majorly reflected the influence of entropy on the phase transformation. The entropy(η) is a very complex physical concept. It can be simply expressed by $\eta = k_B \ln \Omega$. In this term, k_B is the Boltzmann constant, Ω represents the microstates. The monomer of PVDF (T or G) indicates the spatial arrangement of atom. It is a basic microstates of C chain. There are more arrangement states in (TG^+TG^-) , so for the transition $TG^+TG^- \rightarrow TTTT$, $\Delta\eta = \eta(TTTT) - \eta(TG^+TG^-) < 0$. Increasing the temperature, the Gibbs free energy difference (ΔG) will increase, it is detrimental for the transformation. Temperature is not only an important factor in thermodynamic. It also plays the most important role in kinetic side, especially considering the crystallization step of the polymer. Controlling the conformation change in amorphous or solvent is only halfway done. At last, the polymer needed to be crystallized and form the crystal β phase. Generally speaking, the lower temperature is beneficial

for the nucleation of crystal, but the grain growth needed a relatively high temperature to obtain enough kinetic energy. For a lower temperature on the substrate, it can lead to a high β content with too much amorphous phase. Increasing the temperature will enhance the crystallinity, but it will also lead to the reduction of β content. The optimized temperature should be decided by experiment.

Basically, the entropy term discussed in this section reflected the difficulty researchers are facing in a solid-state phase transformation. There was a dilemma: in thermodynamic part, as discussed previously, the lower temperature was preferred to acquire a high β phase. It was shown clearly in Figure 2.8, if a high percentage of β phase was needed, the temperature should be controlled lower than 80°C . However, in kinetic part, if the PVDF was already in its α crystal phase, high temperature was required to activate the chains, making the C-C chain activated for rotation. The conventional solution for this problem, was to apply a high temperature in processing, and in the meantime, introducing other factors to reduce the whole ΔG . This was why it was always needed to apply the electrical field and stretching in conventional methods. From here it was also found the most important advantage of solvent process over other processing methods. In solvent process, organic solvent was used to free the carbon chains from α phase crystal. There is no need to apply a very high temperature such as the melt casting. So that the transformation can be conducted under room temperature and the PVDF with high $\beta\%$ can be produced.

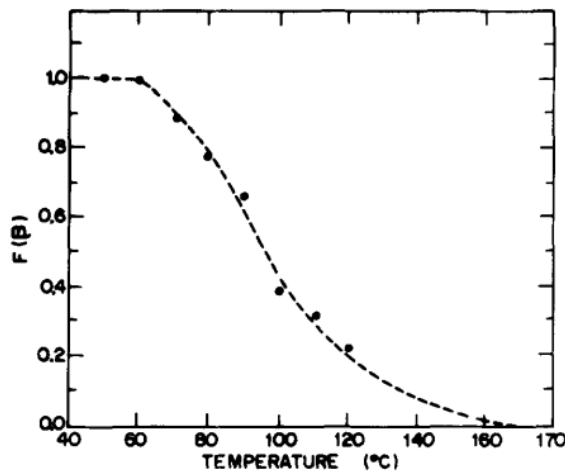


Figure 2.8 The percentage change of phase β , $F(\beta)$ with respect to the crystallization temperature⁹⁶.

Previously, the advantage of solvent process was not fully realized by researchers. That was because most processing methods for obtaining the β phase PVDF were not based on the fundamentally understanding of the β phase formation mechanism. Even if some organic solvents were occasionally selected to fabricate the PVDF fibers or film, researchers usually didn't apply the electrical field to promote the production of TTTT conformation during the solvent or amorphous stage. After the solvent evaporated and PVDF crystallized with high percentage of α phase, the difficulty in solid state phase transformation had to be faced again. Then the advantage of solvent process was almost wasted. on the contrary, in order to take full advantage of the solvent process, the best way is to complete all the process including deposition and conformation transformation, crystallization and even poling in one step. And the electrical assisted printing method applied in this study was the perfect tool for the realization of this methodology.

2.5.3. The term of stress and electrical field

This section discussed the third term and the fourth term on the right side of equation (2.3) together. That is due to a lot of similarities between these two terms.

At first, in most chemical process, both the energy influence of the stress and electrical field were much lower than those of the chemical bonding energy. Thus, the calculation and discussion of a chemical process generally applied the first two terms (internal energy and entropy), which built the classic form of Gibbs-Helmholtz (GH) equation. However, in the conformation transition of PVDF, there was not any break of chemical bonding involved – instead it was only the rotation of the atoms around the C-C bonding, which indicate the energy change produced would not become as great as a regular chemical reaction. This made the magnitude of the third and fourth term comparable with the chemical terms, and also made the extension of the classic Gibbs-Helmholtz equation become meaningful.

Besides, both of the stress field and electric field are vector physical quantities. Much attention should be paid to the directional characteristic in analysis of their influences. In the stress term, σ indicated the applied stress field on the PVDF, ϵ indicated the strain change after the phase

(conformation) transformation. In this expression, both σ and ϵ were vector physical quantities. $\sigma \cdot \epsilon$ notify that the energetic influence of the stress term had directionality. When the applied stress σ and the phase transformation strain ϵ had the same direction, the value of Gibbs free energy change ΔG will reduce and it will promote the phase transformation. On the contrary, if the σ and ϵ had the opposite direction, it will increase the ΔG and hinder the phase transformation. As can be seen from the Figure 2.6 below. Suppose there was a tensile stress along the C-C chain backbone direction, so there was a $\sigma > 0$ in this direction. Then it was found that after the transformation, the length of one unit (include 4 atoms) increased from 4.62Å to 5.16Å which meant an elongation of 11.7% along the C-C chain backbone direction. The elongation strain and the tensile stress had the same direction. Thus, in this case, the applied stress will promote the phase transformation. Similarly, in the fourth term of equation (2.1), \mathbf{E} indicated the applied electrical field, \mathbf{P} indicated the polarization of the dipoles after the phase transformation. $\mathbf{E} \cdot \mathbf{P}$ indicate that the energetic influence of the electrical term had directionality. When the applied electrical field \mathbf{E} and the polarization of dipoles \mathbf{P} induced by phase transformation had the same direction, the value of Gibbs free energy change ΔG will reduce and it will promote the phase transformation. It was also observed in the Figure 2.9. Suppose there was an applied electrical field along the downward direction which is also perpendicular to the carbon chain backbone direction. Before the phase transformation (in α conformation), there was not any dipole and polarization; while after the phase transformation, the dipole perpendicular to the carbon chain backbone appeared because the Fluorine atoms (red circles) had much higher electronegativity than hydrogen atoms (blue circles). As a result, the induced polarization of dipoles by the phase transformation was also in downward direction, which was the same with the applied electrical field. Thus, in this case, the applied electrical field will promote the phase transformation. In conventional solid-state processing of PVDF, the electrical field and tensile stress were usually applied at the same time. It was reported in several literature that the angle of electrical field and stress was optimized at 90°. This result was in good agreement with the theoretical analysis above.

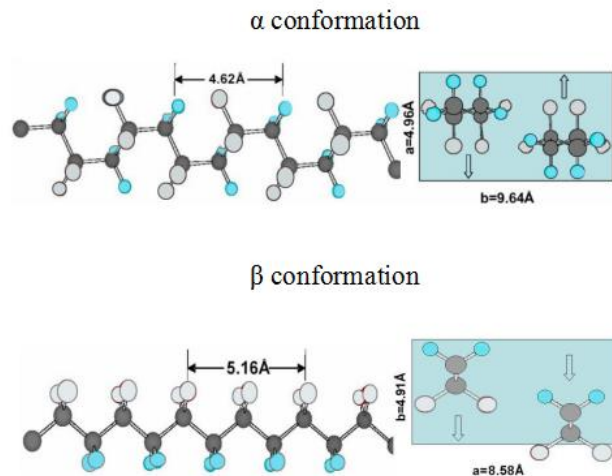


Figure 2.9 The comparison of the chain length between α conformation and β conformation

Previously it was mentioned that the stretching process brought a great difficulty for us to apply the pure PVDF as a functional material for the printed sensor. That was because researcher didn't fully understand the stretching process fundamentally, and the stretching process was always considered as unavoidable for obtaining β phase. In fact, with the help of this proposed mechanism, it was clear that the stretching was nothing but one factor that can reduce the Gibbs free energy change in the phase transformation. It was not that difficult any more to find the alternative methods in further developing of the printing process. For example, one option is to replace some VDF monomer with TrFE to produce P(VDF-TrFE) copolymer to reduce the Gibbs free energy change via decreasing the internal energy; The goal can also be achieved by decreasing the processing temperature to reduce the ΔG by influencing the entropy term in equation (2.1); Otherwise, the additional increase of the applied electrical field can offset the adverse impart for the phase transformation; In addition, the combination of above-mentioned 3 methods can be applied to furtherly enhance the effects; At last, there is no need to restrict to the direct methods just introduced. Any methods, which can influence the related factors in equation (2.1), were potentially helpful in this case.

The most common technique for obtaining macro piezoelectric films in PVDF is mechanical stretching followed by polarization. Mechanical stretching can cause the original symmetrical spherical structure to decompose and rearrange toward a certain orientation. When such deformation takes place at high temperatures (for instance, 140° to 150°C), the influence of

entropy term is two strong, which is favorable for the alpha conformation, so that the resulting structure was still of the nonpolar α -phase. However, when the deformation was conducted below $\sim 90^\circ\text{C}$, the driving force for the beta phase became stronger, the molecular chains were also forced into their most extended possible conformation, which is the all-trans: its monomeric repeat corresponds to 2.56\AA compared to 2.31\AA for the TG^+TG^- . Therefore, mechanical extension at low temperatures had the advantages of producing not only a molecularly oriented morphology, but also one belonging to the polar β -phase. However, the dipole vectors were still not uniquely oriented but lie randomly in planes normal to the molecular chains. The final step was therefore required to produce a macroscopically polar specimen to align these dipoles in the direction of an externally applied field normal to the film. This was usually accomplished by evaporating electrodes on the sample and connecting them to a high-voltage source supplying a field of at least 0.5 megavolt per centimeter, or by using plasma or corona poling. The mechanism of this dipole reorientation in PVDF was beyond the scope of phase transformation, and detailed discussion of poling process was included in Chapter 4.

2.5.4. The comprehensive analysis of the extended Gibbs-Helmholtz equation

A simple introduction and analysis were given respectively for each term in Gibbs-Helmholtz equation above. In order to apply this mechanism in the future study, one should learn how to comprehensively use the basic principle in processing design. Because in the real manufacturing procedure, it usually included multiple factors that collectively decide the result, instead of single factor. Some case studies were shown as below.

It was reported that applying higher temperatures during electrical poling in fused filament fabrication (FFF) could increase β -phase⁷⁴. This result looked in conflict with our above analysis that low temperature was beneficial for the β conformation. In this case, what should be understood first was that the β -phase in literature usually indicated the crystal phase. While our theory mainly analyzed the formation mechanism of β conformation. Obtaining high content of β conformation didn't automatically result in high content of β crystal phase. It was necessary to find a method to promote the crystallization to realize our goal. In this case, because high electrical field was applied to prevent the β conformation transformed back to α conformation, a

higher processing temperature could promote the crystallization without sacrifice too much β conformation content. It can be inferred that the application of higher nozzle voltage in printing system will increase the polarization ability of the system. However, relying solely on the increase of electric field has its limitations. When the applied in-situ electric field reaches the upper limit allowed by the instrument and equipment, the excitation arc between the nozzle and the substrate will influence the stability and safety of the device.

A negative example that must be avoided is shown in ⁹⁷. At the beginning, high beta phase content (about 95%) was obtained by extrusion, quenching and stretching of PVDF monofilaments. However, most of the transformed β -phase is returned to the α -phase by high temperature heat treatment. The reason can be clear find in our theory that high temperature was not only beneficial for the formation of α phase, it can also accelerate this inverse transformation in kinetic part. Conducting the post processing under high temperature without using any methods to offset its adverse impact, all the previous effort came to naught. This example told us that the proposed β phase formation mechanism can not only help us to obtain β phase, it was also of vital importance for maintaining the β phase during the post processing and operations.

2.6. Analysis of melt and solid states processes

From the content of previous sections, it was indicated that this proposed mechanism may not limited to the one-step solvent process. In essential, the major contribution of this mechanism was to introduce the chain conformation as the intermediate states for the phase transformation. And due to the low temperature and high mobility of the chain in solutions, the process of conformation transition became the decisive procedure of the phase transformation. In other processes (melt or solid states), the conformation intermediate state may not play the decisive role as in solvent processes. However, this mechanism can still help us to understand the fundamental of other phase transformations in PVDF, because any phase transformation in PVDF cannot finish without the transition of conformation. Most of the conventional methods are reviewed in the figure 2.10 below. The start points are either PVDF melt or PVDF solution which can be produced by heating the PVDF powders or dissolved it in organic solvents. And we

set the beta phase PVDF as ending point. From this figure, we can see, the conventional method usually uses electrical field, the stretching, the high pressure, the temperature control to obtain the beta phase. The previous research in this area is basically empirical. Researchers depend on the parameter study to obtain the piezoelectric in PVDF. These results are useful, but sometimes separated, and even conflicted. There is not any complete and fundamental understanding for the formation of beta PVDF. But previously researchers and users are quite satisfied with this. Because using those empirical result, the required beta phase PVDF is already fabricated in the factory and labs. But when we are considering applying the PVDF as the critical functional material in the all printed sensor structures, the collection of empirical results is not enough. Because for this time, the goal is no longer to fabricate the beta phase PVDF as final product in controlled conditions. Instead, the goal is to develop the printing technology for PVDF with beta phase in varied conditions and in different structures.

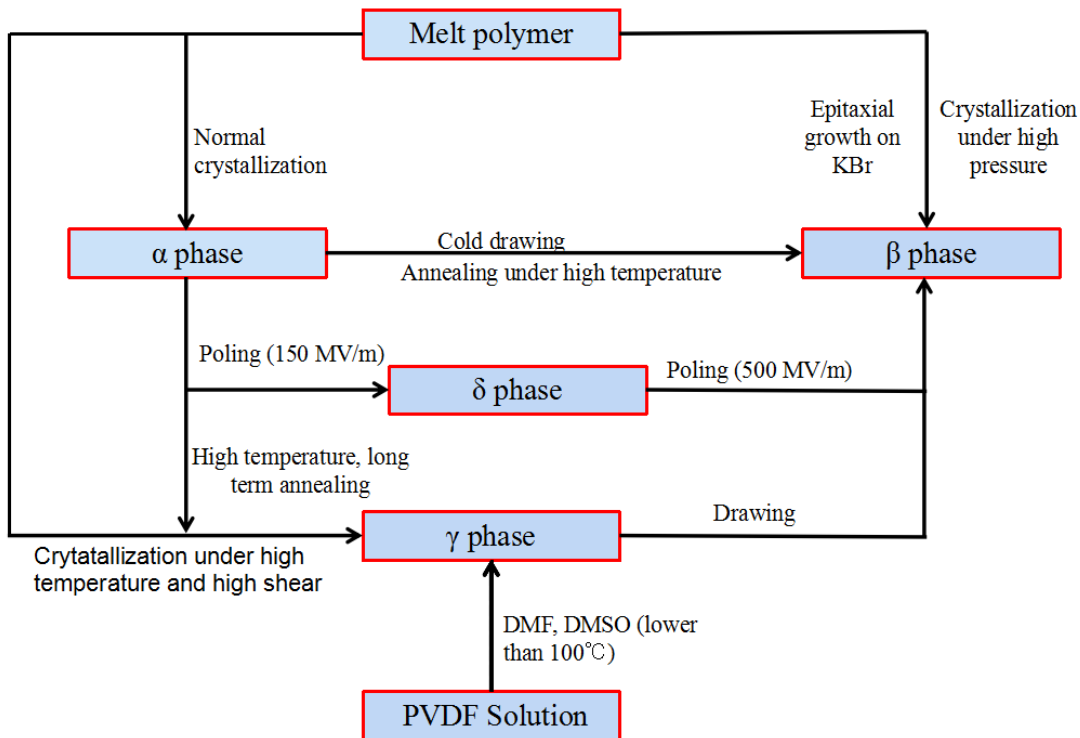


Figure 2.10 Manufacturing chart for the α , β , γ and δ phases in PVDF.

2.6.1. The γ phase conformation

It had already discussed a lot on α phase conformation and β phase conformation. Although the γ phase is not as important as α phase and β phase in PVDF, it is still necessary to have a basic understand of this phase conformation. From its monomer sequential (TTTGTTTG'), this conformation can be considered as transitional conformation between the α phase and β phase conformation. Because this conformation has neither a low steric hindrance as all-trans β phase conformation, nor it possess the high percentage of hydrogen bond as α phase conformation. This transitional conformation has a higher internal energy (U) than both α phase and β phase conformations. It has more microstates than both α phase and β phase conformations, so a higher entropy (η) was expected. With respect to the stress term, the length of chain (l) in γ phases conformation should lie between the value of α phase and β phase conformations. The influence of electrical field was ignored in this chart, so we only analyze the first three term of the GH equation. It can still be found that the dipole polarization of the chain is between the value of α phase and β phase conformations.

For conformation transformation $\alpha \rightarrow \gamma$:

$$\Delta U > 0, \Delta S > 0, \Delta l > 0$$

For conformation transformation $\gamma \rightarrow \beta$:

$$\Delta U > 0, \Delta S > 0, \Delta l < 0$$

2.6.2. The melt processing

In the melt processing, because the high temperature of melt provided enough mobility for the chains, the thermodynamic factor usually plays the decisive role. The α phase conformation has the lowest Gibbs free energy in most temperature range. When PVDF is slowly solidified from melt, given enough time, it will ultimately form the α crystal phase. This is the case denoted as normal crystallization in Figure 2.10.

Because $\Delta U(\alpha \rightarrow \gamma) > 0$, $\Delta S(\alpha \rightarrow \gamma) > 0$, there will be a temperature T_γ that can make

$\Delta G(\alpha \rightarrow \gamma) = \Delta U - T_\gamma \Delta S < 0$. And if $T_\gamma < T_m$, this conformation transformation is meaningful in reality.

This is the case described as crystallization at high temperature in Figure 2.10. As a result, the γ phase will be produced in this process.

It was also mentioned that γ crystal phase can be produced from melt under high shear. This phenomenon was beyond the scope of the proposed mechanism, because in conformation transition, the stress term in GH equation usually only count in the chain length (other direction of chain was considered flexible). In fact, similar with our modal based on conformation, the GH based on the crystal phase can also be built, although it will be much more complicated. The influence on the Gibbs free energy can then be calculated from the lattice strain with respect to the shear stress.

In the previous section, we discussed the situation where stress was inconvenient and found that the stress was alternative by electrical term and other effects. On the contrary, if electrical field was not applied, its influence on the Gibbs free energy should be compensated by the stress. In Figure 2.7, it was shown that β phase can be obtained by crystallization under high pressure. Although any effect of stress other than the stretch cannot directly explained by the proposed mechanism for conformation transformation. It was easy to deduce that the effect of pressure perpendicular to the chain direction was almost equivalent to the effect of stretch along the carbon chain.

The melt processing discussed above were all thermodynamic process because of high motion energy provided by the high temperature in melt. However, there was one exception, which is called Epitaxial growth on KBr. In this process, the melt was quenched to a very low temperature, and thus the kinetic factors dominate the process. This factor was called Heterogeneous nucleation, in which the PVDF crystal grew based on the lattice plane of KBr. Thus, the matching of the close-packed plane of different crystal phase in PVF on the (100) plane of KBr crystal will decide which phase is favorable in this process. The lattice parameter of KBr is 6.598\AA , and its close-packed plane has a dimension of $6.598\text{\AA}\times 6.598\text{\AA}$. The close-packed plane in α , β , and γ phases respectively have the dimension of $5.02\text{\AA}\times 9.63\text{\AA}$, $8.58\text{\AA}\times 4.91\text{\AA}$, $4.97\text{\AA}\times 9.66\text{\AA}$ ⁴². It was clear that the β phase has the lowest mismatching.

2.6.3. The solid state processing

For phase transformation $\alpha \rightarrow \gamma$, as already been discussed, $\Delta G(\alpha \rightarrow \gamma) = \Delta U - T\Delta S$ ($\Delta U > 0$, $\Delta S > 0$). γ phase is more stable under high temperature. Through annealing treatment for a long time, the solid-state phase transformation will occur automatically. In the meantime, the high temperature is also favorable kinetically for the phase transformation. Thus, the process called high-temperature, long term annealing, is quite simple. All we must do was to select a temperature as high as possible (should be lower than T_m), and then to wait for the transformation to complete.

For phase transformation $\alpha \rightarrow \beta$, it was interesting to make a comparison of two similar solid-state processing. One was the cold drawing; the other was through the annealing under high pressure. Both methods took advantage of stress to provide the extra driving force for the phase transformation. Why under compressive stress, high temperature was required, but under stretching stress, the transformation can occur in low temperature?

Lovinger³⁸ pointed out that mechanical drawing caused a break-down of the original spherulitic structure into an array of crystallites whose molecules were oriented in the direction of the force. When the deformation was conducted below $\sim 90^\circ\text{C}$, where the polymer was much stiffer, the molecular chains were also forced into their most extended possible conformation, which was the all-trans (β phase conformation). Therefore, mechanical extension at low temperatures had the advantages of producing the polar β -phase. In other word, the stretching stress not only can provide the thermodynamic driving force for the phase transformation, it can also destroy the original α crystal phase structure, which could activate the carbon chain for the rotation.

However, under compressive stress, the original crystal phase was intact, thus extra energy was required to activate the carbon chain from the crystal state, this was why high temperature was required. Even worse, due to the detrimental effect of high temperature on the thermodynamic part, much higher compressive stress was needed to compensate this effect, which could add more obstacle on the manufacturing. Clearly, the cold drawing is a better method, and it is more commonly used.

For phase transformation $\gamma \rightarrow \beta$, γ phase was more stable in high temperature. The transformation cannot be promoted by increasing the temperature. But the low temperature should also be avoided for all solid-state phase transformation. It was pointed out previously that the chain length change (Δl) is positive during the phase transformation, thus the stretching stress can provide the extra driving force for this phase transformation. It was just discussed the stretching stress can destroy the original crystal structure, that will activate the carbon chain for rotation. As a result, a high temperature was no longer required in this case. The optimized process is to draw the sample under room temperature.

3. Fabrication and optimization of PVDF thin film by AM technology

This chapter presented an Electrohydrodynamic (EHD) printing method to fabricate PVDF thin films with high β phase and high crystallinity using PVDF powders as raw material. This printed piezoelectric film can be either used in smart layers to detect large strain, damages, and delamination in composite structure or used in actuator and energy harvesting and other applications. The objective of this chapter was to present an experimental approach for fabricating piezoelectric PVDF thin films using electrical assisted ink jet printing technology based on the proposed $\alpha \rightarrow \beta$ mechanism. First, printing instruments and solvent preparation were discussed in detail. Next, the piezoelectric thin films were fabricated using solution process and the processing parameters influencing the $\beta\%$ in thin films was studied. In addition, the crystallinity of the printed thin films including the significance advancement in the use of MWCNT and GR additives was studied. And finally, the post printing treatment for enhancing and maintaining the piezoelectric properties of the films was analyzed.

3.1. Processing of PVDF thin films

To achieve smart composite structures, the polymeric piezoelectric PVDF film which acted as the functional materials, need to be carefully studied, to optimize the performance of the piezoelectric sensing system. In this task, we will investigate the optimal procedures, together with the mechanism proposed in Chapter 2, to fabricate the high-performance piezoelectric sensors.

3.1.1. Printing setup and apparatus

The application method in this study was very similar to the so-called near-field electrospinning (NFES). Compared with the remote electrospinning (FFES), the distance between needle and substrate was reduced to improve the position controllability, as shown in Figure 3.1 (a) ⁷⁶. In the

early stage of near-field electrospinning, the dipping method was adopted, as shown in Figure 3.1 (b). In this case, the polymer solution must be repeatedly immersed in order to obtain the source of sediment raw materials. This method of production was discontinuous. Later, continuous near-field electrospinning using syringes (shown in Figure 1.10 (c)) was developed so that printing ink could be continuously supplied to continuously deposit printed fibers. This improvement kept the continuous deposition characteristics of NFES similar to traditional FFES, and at the same time had excellent controllability for printing process.

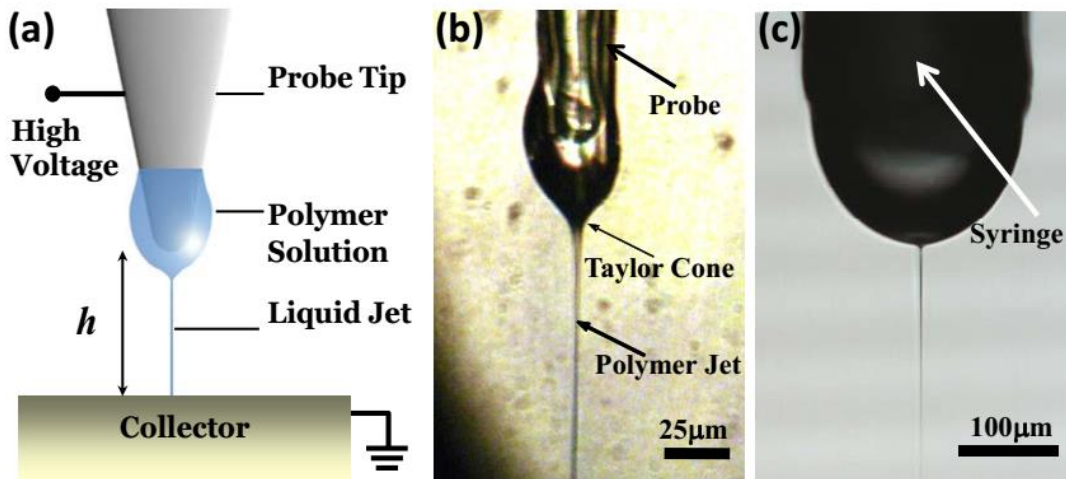


Figure 3.1 (a) The setup of near-field electrospinning (NFES) process. (b) The image showing the NFES with the dipping method. (c) The image showing the continuous NFES method.⁷⁶

The setup of printing system in this study is quite simple. Basically, the printing platform is an FDM printer for the processing, the X, Y stage can be used to control the position of needles on the printing plate. This is the basic type of FDM with the lowest accuracy (with working precision 50 μ m). And the position of needle on Z axis cannot be automatically controlled. But because this study is focused on the material phase and property, it is enough for our task. We replaced the heat extrusion nozzle with a glass/plastic injection whose needle of injection was linked with DC high voltage power supply. At this moment, the simplified EHD printing system is built. With the system, the Taylor cone, and the ink jet can be produced during this process.

Essentially, the printing method used in this study belongs to the electrohydrodynamic (EHD) printing method⁹⁸, in which the polymer solution or melt used as printing material or ink can

form Taylor cone structure because of the high electrostatic field and eject a fine jet or droplet from the cone. This technology has opened up a new field in structural design, and it is possible to achieve material performance design that has not been achieved so far. In EHD printing, the diameter of ejector is obviously smaller than the size of nozzle, which overcomes the limitation of nozzle size and enables the production accuracy to reach micro/nano scale⁹⁹. According to the different processing conditions of EHD, there are printing modes, including widely used electrojet and electrospinning, which belong to the unstable EHD mode.

In the EHD process of this study, the PVDF polymer was first dissolved in organic solvents, and then the solution was transferred into a glass syringe with metal needles. Then a voltage (1-6 kV) was applied between the needle tip and the substrate about 2 mm away from the needle. In the printing process, the substrate was made of glass, and the grounding electrode was made of brass plate. Under the action of high potential, the droplets overcame the surface tension of the solution, spray out from the tip of the needle, and deposited very fine PVDF fiber structure on the collector. The experimental setup details were shown in Figure 3.1, including stainless steel needle (inner diameter: 0.33-0.5 mm), syringe, high voltage power supply (DW-P303-1ACF0) and XY control platform (modified from basic FDM printer). The motion speed of the XY control platform is 2mm^{-1} . Other parameters, such as applied voltage and droplet flow, can be accurately controlled as required. The experiment usually was required to be carried out in a closed room with room temperature (28°C) and relative humidity less than 50%.

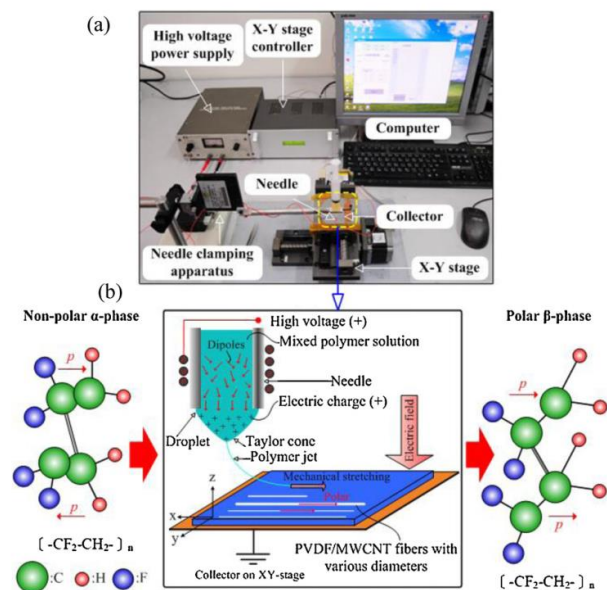


Figure 3.2 (a) The setup of the EHD printing. (b) The schematic of printing process (including the α - β phase transformation induced by the in-situ poling)¹⁰⁰.

The temperature of the substrate was set at 70°C. After 70 layer-by-layer printing, the flexible PVDF film (20mm×20mm×40μm) was printed, as shown in Figure 3.3 (c) - (f). Then a gray layer of electrodes (Au layer) will be coated on both sides of the printed film, as shown in Figure 3.3 (f). It was also exhibited in this figure about how the film were formed. We have mentioned previously that the solution printing was mainly used to produce the PVDF fibers. In this study, what we obtained firstly was also the tiny fiber jets as shown in this figure. In this figure, the printed PVDF looks rather like fiber mat than a thin film. There are a lot of gap between those fibers. When the fiber reached the substrate, it is still in semi solid state. Then it will spread out. And because we can control the tiny fibers extremely close to each other. The spread of the solution will finally fill most of those gaps and form the film structure. We can also find the color of surface strongly influenced by the doped additive. The last figure showed the topography of thin film after the nano silver electrode was painted.

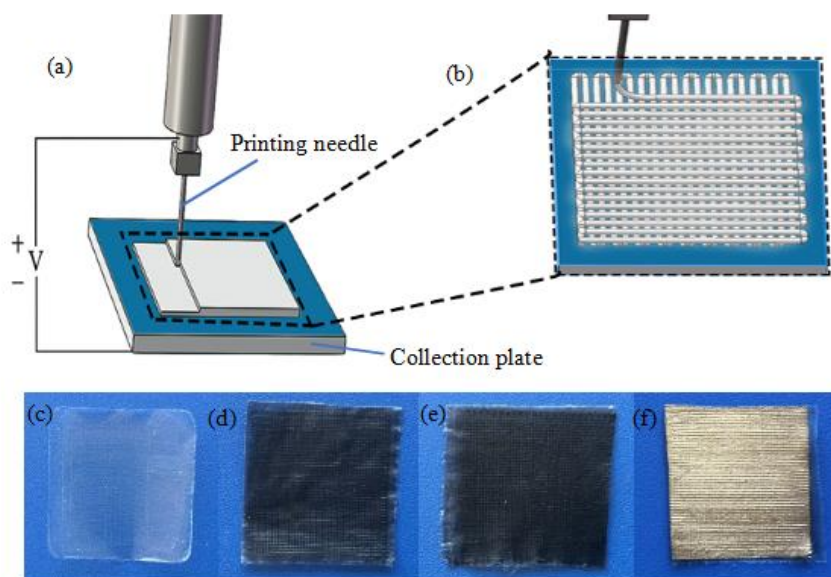


Figure 3.3 (a) 3D printing process for PVDF thin films, (b) layer-by-layer printing films with filamentary semi-liquid flowing. Photograph of (c) pure PVDF thin film (d) PVDF film addition of 0.03 wt% MWCNTs (e) PVDF film addition of 0.03 wt% GR (f) PVDF film with electrode layer.

3.1.2. Preparation of PVDF solvent

PVDF printing ink was prepared by the following steps: first, the solute and solvent are weighed by analytical balance. A clean glass beaker was placed in the balance chamber, and the required PVDF powder ($M_w = 534000 \text{g/mol}$) was added to the beaker with a plastic spoon. Dimethyl sulfide (DMSO), dimethyl acetamide (DMAC) and N-methyl-2-pyrrolidone (nmp) were used as polar organic solvents to prepare various PVDF solutions with different concentration. Table 3.1 listed three different PVDF solutions. Among all these three types of solution, the NMP PVDF solution was majorly used in this study. And beside this, the green solvent γ -Butyrolactone (GBL) was also tried in this study and was discussed in detail in subsection 3.2.1. Other than the mixing of solvent, additive such as Multi-walled CNT (MWCNT) and Graphene (GR) were used to improve the performance of the printed thin films. In order to achieve a homogeneous dispersion solution with those additives, a pre-dispersion step by sonication for 4 hours was applied.

Table 3.1 Conditions for printing solvent

Solvent	Stirring temperature	Stirring time
DMSO	55°C	1h-1h20min
DMAC	40°C	30min-40min
NMP	45°C	1h-1h15min

Following the preparation of the PVDF-solvent mixture in 20 mL batches, the solution was stirred using a magnetic stirring hot plate to completely dissolve the PVDF powder. A magnetic stirring bar was placed in the glass beaker, and the solution was stirred at a constant temperature of 50°C and 700RPM for approximately 20 minutes. Aluminum foil was used to cover the beaker in order to minimize the effects of evaporation during the stirring cycle. The PVDF powder was completely dissolved and a transparent and homogeneous polymer solution was formed. Before this stirring step, the Acetone was added to control the evaporating speed of the solvent. The mixed solution was sealed in a container to prevent evaporation effects at high temperature inside the water bath. Without ultrasonication, the PVDF powder agglomerated and were unsuitable for film fabrication. In this study, 12-18wt% of PVDF solution was used for printing. More specifications in the experiment were exhibited in sequential as below:

- 1. Calculating and weighing strictly according to the mass ratio. (PVDF wt%: 12%, 13%, 14%, 15%, 16%, 17% and 18%)
- 2. Putting PVDF powder in the solvent and stirring the solvent until it turns clear.
- 3. Turning down the stirring rate for 5min, and then keep warm and stand for 10 min to reduce the bubbles in the precursor.
- 4. Adding 2-3mL precursor solvent in syringe and trying the piston to make sure the solvent

drop can be smoothly pushed out.

- 5. Pushing the piston and after 30s starting the printing process.

3.1.3. The process control in printing

The success of printing process depends on the control of process parameters, including material flow rate, printing temperature, printing voltage and so on. In this process, the change of any of these parameters may significantly affect the geometry of the printed filament ¹⁰¹. It can be considered that the shape, accuracy and consistency of profiles of deposited materials are affected by several parameters. These parameters should be carefully adjusted in order to optimize the deposition filaments and obtain uniform geometry. Any filament deformation caused mainly by lag or leading phenomena after deposition should be minimized in order to prevent its accuracy from being affected.

Various patterns can be collected on the collector to demonstrate the controllability of printing technology using a programmable path X-Y stage. The time delay of the X-Y stage made the polymer jet unstable, creating spirals in the corners. The diameter of PVDF nanofibers can be adjusted by controlling various parameters, including the internal diameter of the needle, the electric field, the X-Y stage speed, the PVDF solution concentration, and the solvent concentration. Results showed that the PVDF fiber diameter depends on the needle size. With 17#(1.12mm) and 21#(0.51mm) needles, when the droplet overly accumulated on the tip, there was not enough space between the Taylor cone tip and the collector. Thus, a large droplet would directly drop on the collector, blocking the spinning route. When the needle was 26# (0.23 mm), the PVDF solution was difficult to spin because of high viscous resistance on the internal wall of the needle. Thus, experiments showed that the needle size of 0.3mm (24#) and 0.26mm (25#) produced a stable jet of polymer solution during the printing. It was also showed the relationship between the electric field and the diameter of the PVDF fibers, demonstrating a linear relationship between the fiber diameter and applied electric field. Under a higher electric field, both the Taylor cone size and polymer jet diameter increased. This resulted in thicker fibers and made it difficult to control the fiber diameter. In continuous printing process, the effect of the Coulomb repulsion force in the polymer jet can be reduced by decreasing the needle-to-collector

distance¹⁰⁰. Some detailed technology specification was listed as below:

Various patterns can be deposited on the substrate to demonstrate the process controllability of printing technology using programmable path X-Y stage. The delays of X-Y level make polymer jets unstable and spiral in corners. The process parameters for adjusting the diameter of PVDF fibers included the inner diameter of the needle, electric field strength, needle tip velocity and solution concentration, etc. When using thicker needles such as 17 # (inner diameter 1.12 mm) and 21 # (inner diameter 0.51 mm), the droplets will accumulate excessively at the tip due to the large size, which will result in insufficient space between the Taylor cone tip and the substrate. Therefore, sometimes large droplets fell directly on the collector, blocking the printing route. When the needle was too thin, such as 26(0.23 mm), the PVDF solution was difficult to eject because of the high viscosity resistance of the inner wall of the needle. Therefore, experiments showed that the optimized size of needle was 0.3 mm (24#) and 0.26 mm (25#). At this point, a stable polymer solution injection will occur during the printing process. Previous experimental results also showed a linear relationship between the electric field strength and the diameter of PVDF fibers. However, if the electric field intensity was too high, the size of Taylor cone and the diameter of polymer jet will increase which will lead to fiber thickening, and making it difficult to accurately control the diameter of the fiber¹⁰⁰. Some detailed technical specifications were listed as below:

1. Film dimension 20mm×20mm;
2. Needle horizontal moving speed 30mm/s;
3. Needle type: 26# (0.23mm), 25# (0.26mm), 24# (0.3mm), 22# (0.41mm), 21# (0.51mm) and 17# (1.12mm);
4. Printing environment: Room Temperature (28°C); standard atmosphere; relative humidity 40%~50%.



Figure 3.4 The needles, the syringe, and the printing platform used in this study

Before the printing process begins, it is essential to adjust the printing parameters to form a uniform layer with clear boundaries. Because ink type and nozzle diameter was determined, a key parameter determining accuracy is the spacing between continuous droplets. If such spacing is too small, too many droplets will be deposited, resulting in poor resolution. Excessive spacing will lead to voids in materials. Therefore, preliminary calibration must be carried out before formal printing to determine the optimum distance between droplets. This calibration should be carried out on the same substrate surface for the following process of thin films.

Researchers have developed the effects of different ink characteristics on print resolution. Examples include organic fugitive ink ¹⁰², concentrated polyelectrolyte complex ¹⁰³, colloidal suspension ¹⁰⁴, hydrogel ¹⁰⁵ and thermosetting polymer ¹⁰¹, etc. Different solidification mechanisms exist for different inks to maintain the geometry of extruded filaments. These mechanisms include viscoelastic recoil, ultraviolet polymerization or solidification by solvent evaporation. Some of these methods provide high spatial resolution. Therefore, the dimensional accuracy can be improved by controlling the rheological property and curing mechanism of the ink.

For all of the additive manufacturing process, the major physical procedures occurred on the surface, which include solidification, phase transformation, and crystallization in this study.

These three procedures are not happened separately. In reality, the phase transformation occurred throughout all of those steps. But generally, the solidification occurred in the early stage. And crystallization occurred close to the final stage. The same parameter in the printing process could influence single or multiple physical procedures. As shown in this figure, the solidification is mainly influenced by temperature and the added Acetone; The phase transformation will be influenced by temperature, solvent, evaporation time, electrical field, and etc.. The crystallization is mainly influenced by temperature and additives. And these three physical procedures are interconnected to each other. Thus, the complex interaction between the physical procedure and processing parameters dramatically add the difficulty of this study. A simple parameter study is not enough for our goal. Only combining the parameter study with our proposed theory, can we find the correct method to optimize the piezoelectric performance of the material.

3.1.4. SEM Results

The cross section of SEM topographic images (Figure 3.4(a) below) showed the thickness of the printed PVDF thin film was around 40 μm . And this thickness was evenly distributed throughout the area of thin film. From the surface image (Figure 3.4(b) below), high concentration of hole sites can be observed which were created by the evaporation of organic solvents out of the PVDF thin film sample. The high porosity of the printed PVDF thin film could bring some difficulty during the following step of sensor fabrication. Because when a high electrical field was applied during poling process, all of those holes would become the weak point of the structure and would be subject to the breakdown, especially if the poling was exposed to the air. The breakdown of the printed film occurred within 10min under the field of 30MV/m.

Besides there were several tiny circular micro particles appeared in the film as shown in the inset of Figure 3.4(b), which was believed to be spherulites. A lot of filamental-shaped structures were also observed in Figure 2(b) indicated by the arrow. In the case of the printed PVDF thin films, the film was composed layer by layer. The evaporation of the solvent and the solidification of each printed layer must almost complete before the printing of the following layer with the help of Acetone additive and heating plate under the substrate. Otherwise, the whole shape of the film structure would become uncontrollable, just as the solidification of a large liquid PVDF solvent drop. As a result, the whole time for the semi-liquid state of the PVDF is very limited, the upper

limit of which was around the printing time for each layer (1.14min). It can be observed that the effective time of semi-liquid state under the influence of electrical field were rather shorter due to the mobility of the needle.

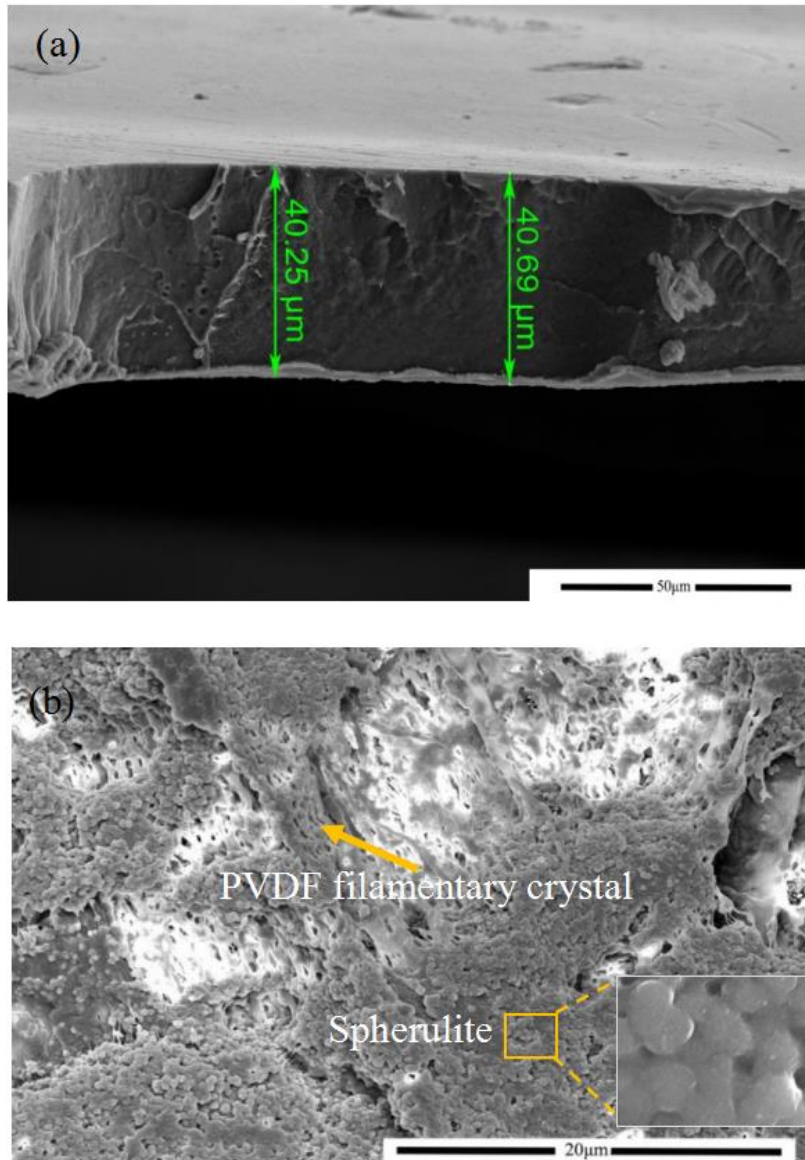


Figure 3.5 SEM results for the (a) image of cross-section in PVDF thin film; (b) surface image of PVDF thin film

3.2. Parametric studies on the β -phase content of PVDF thin films

In this section, it was tried to obtain the PVDF thin films with high β -phase content by controlling the processing conditions. X-ray diffraction (XRD) analysis showed a high diffraction peak at $2\theta=20.8^\circ$ in the piezoelectric crystal β -phase structure. Therefore the XRD patterns were important indication of β -phase. Other than the XRD, the FTIR method was also applied to characterize the material. The current study presented a method of controlling the β -phase content in PVDF based on the newly proposed mechanism. The parameters of printing temperature, the applied voltage and solvents can strongly influence the transformation of $\alpha \rightarrow \beta$. This method can potentially be extended to the copolymers of PVDF and other piezoelectric polymers for various sensing and actuation applications.

3.2.1. The selection of solvents and additives

The selection of the organic solvents on the production of β -phase in PVDF was first studied. There were other important properties of solvents, such as viscosity, that will influence the smoothness of printing and the quality of the products. But they were not in the scope of this research. Based on some analysis proposed in chapter 2, there were two critical factors in solvent that will decide the formation of β -phase:

1, the polarity of the solvents;

From the electrical term in equation (2.1) ($\mathbf{E} \cdot \Delta \mathbf{P}$), we knew that applied electrical field can influence the production of β phase by the induced polarization during the phase transformation. However in the solvent, we should replace this applied \mathbf{E} into the effective \mathbf{E}_e . Because in the PVDF solution, the real applied electrical field around the region nearby the PVDF chain, were not the nominal \mathbf{E} calculated by the applied voltage. It was strongly influenced by the polarity of the solvent media. The higher the polarity with the solvent, the higher effective electrical field was applied, and the driving force for the phase transformation will become stronger. In this study, we selected Dimethyl sulfoxide (DMSO), N-Methyl-2-pyrrolidone (NMP) and Dimethylacetamide (DMAC) with the polarity index of 7.2, 6.7 and 6.5 respectively [-3], which

were the highest among all the organic solvents.

2, the evaporation time for the solvents.

During the printing process, the PVDF solution will solidified and form the thin film layers on the substrate. Although the phase transformation in PVDF can still occur in its solid state, the carbon chain backbone had much higher mobility in its solvent state. If the PVDF solution had a longer evaporation time under electrical field, a higher β phase production will be obtained. However, the extension of evaporation time had its limitation. For each layer, it was necessary to make sure most of solvent evaporated before the beginning of the printing process of the next layer. In order to realize this goal, Acetone were needed to mix with the PVDF solution to acceleration the evaporation procedure of the solvent. In the result of preliminary work, it was found that adding 2g Acetone in 10g PVDF solution will make one layer of PVDF solution almost solidified at the moment the next layer printing got started (When using 24#needle and substrate temperature of 60°C). The PVDF concentration will also influence the evaporation time. The higher content of PVDF meant the lower content of solvent, and thus less time for solvent to evaporate.

Below was the XRD pattern of the printed thin film using 12wt% PVDF in NMP and DMAC solvent respectively. Because of the very close value in polarity, the PVDF thin films prepared using different solvent but with the same PVDF content will exhibit similar XRD patterns which indicated similar content of β phases were obtained.

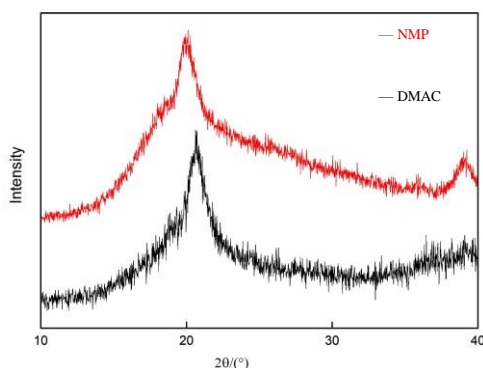


Figure 3.6 XRD patterns of thin film prepared by 12wt% NMP and DMAC solvent

In recent years, more and more attentions were spend on safety and environment friendliness issues. Unfortunately, those organic solvents with high polarity usually were all highly toxic. Besides the toxicity, all of the solvent used in this study (DMSO, NMP and DMAC) were high volatile which were easily adsorbed by human body during the printing process. To address this issue, it was necessary to take protective measures such as enhancing ventilation, wearing protective suit etc... But these methods cannot ultimately resolve the problem, especially as the extensive applying and industrializing of this technology. Are there any alternatives that were relatively healthy? The green solvent γ -Butyrolactone (GBL) was widely considered as an option. It was illustrated how this solvent will perform in this study as below. The thin film showed in Figure 3.5 was prepared in the 14wt% PVDF in GBL solvent. A high percentage of β phase can be observed in this case, which meant GBL was also a promising solvent in printing of piezoelectric PVDF. Although weak α peaks were also observed, it could be improved by further optimization. But the real problem of this solvent was not in this part. One difficulty was that the volatility of this solvent was too low. In order to make sure each layer to be solidified in time, one method was to add 5g Acetone in every 10g PVDF-GBL solution. And because of the high volatility of Acetone, the printing ink was so unstable that it usually blocked up the needle when printing for a long time or when temperature of ink went down. To address this problem, larger needles were tried to reduce the printing time and prevent the blockage. But this will introduce a greater problem that will be discussed in detail in the following subsection. So far, the green solvent GBL was still not a suitable solvent for continuous printing process in our study. For the

replacement of current toxic solvent, it was necessary to first find a way to reduce the Acetone content required for GBL ink, it was also needed to improve the solvent on its smoothness for printing and so on.

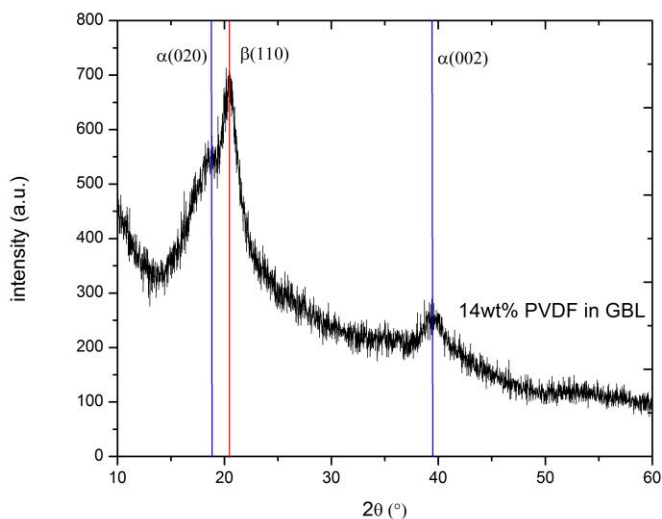


Figure 3.7 XRD patterns of thin film prepared by 14wt% GBL solvent

3.2.2. The PVDF wt% of solutions on β phase production

The PVDF wt% can generally influence two aspect of printing process. Firstly, as the increase of PVDF content, the solution became thicker and the viscosity became higher. In this situation, the surface tension of Taylor cone became difficult to overcome, which will dramatically influence the smoothness of printing process. Secondly, higher PVDF content meant lower content of solvent. The time required for the evaporation of solvent will be shortened. It was analyzed in the last section that the reduction of evaporation time would potentially decrease the β phase production. But whether this reduction of evaporation time had this effect depended on the real time the phase transformation needed. In Figures 3.5, it was observed the influence of PVDF content on the production of β phase. It showed the XRD patterns for printed PVDF thin films with PVDF wt% of 12 wt%, 13wt%, 14wt%, and 15wt%, respectively. In these plots, one can observe all of the curves included the diffraction peaks around 20.8° , representing (111) plane in β -phase PVDF. From 12wt% to 14wt%, although not any obvious influence of different PVDF wt% on the β -phase in produced thin films was found, an increase trend of α phase can still be

observed. That is because as the wt% of PVDF increased, each layer of printed PVDF became thicker, the average processing time in liquid state reduced. Thus the conversion rate of β phase will also be reduced. All in all, these XRD results suggested that large amount of β -phase PVDF thin films can be constructed by the ink jet printing process. When PVDF wt% increased to 15wt%, it was observed the peak became much weaker and flattened, which indicated a high content of amorphous phase in produced thin film. As just discussed, one important factor in solvents that can influence the transformation of β phase was their evaporation time. It was clear in 15wt% PVDF solution, the factor of evaporation time dominated the process. Under this condition, because the solution got solidified too soon, the conformation transformation as well as the crystallization procedure, both of them had not enough time to occur. At this time, the major phase produced in the thin film was amorphous phase.

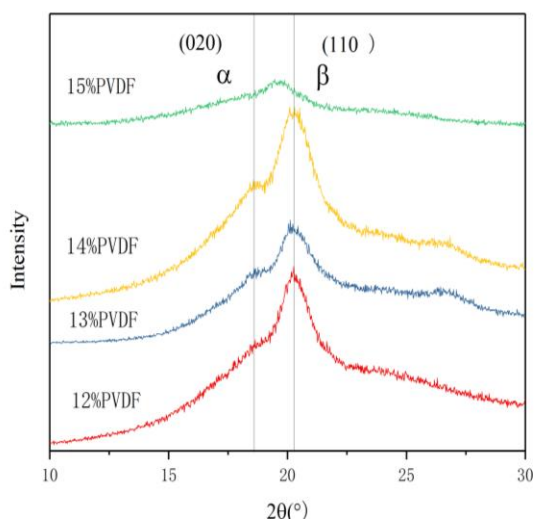


Figure 3.8 XRD patterns of PVDF thin films prepared with varied PVDF wt% in DMAC solvent

3.2.3. The doping of additives on the production of β phase

In the previous two subsections, it was discussed how to enhance the β phase production through the change of solvent, based on the two basic factors (solvent polarity, evaporation time). Another option was to add some additive to improve the present solvents: to intentionally improve the polarity of solvent; or to strengthen other relative properties of the solvents.

Actually, in this study, Acetone was used as additive all the time, to adjust the evaporation time

of the solvent. Without the help of Acetone, it was even impossible to make sure each layer of ink almost evaporated at the beginning of the next layer. From this simple example, one can find the indispensable effect of additives in printing, although they could act in various occasions and mechanisms.

The graphene (GR) and multiwall carbon nanotubes (MWCNTs) were frequently reported to act as solvent additives in PVDF manufacturing. In this study, 0.01-0.05 wt% of MWCNTs and GR were added in the 15wt% PVDF NMP solvent. The XRD patterns were showed as below. It can be seen from Figure 3.7 that the situation in MWCNTs and GR were similar. The major phase in the samples added with both additives were β phase. And in both case, the XRD results were not sensitive to the variation of the concentration of GR and MWCNTs additives, except for the little shift of peak in 0.04wt% and 0.05wt% GR samples. The reason for this phenomenon was still unclear.

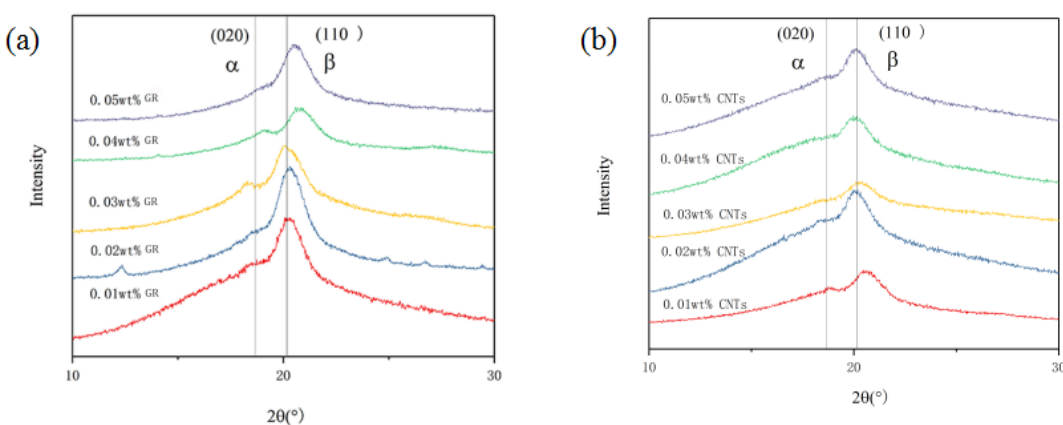


Figure 3.9 XRD patterns of PVDF thin films prepared with 15wt% PVDF in NMP solvent added with (a) 0.01-0.05wt% GR additives; and (b) 0.01-0.05wt% MWCNTs additives.

As introduced in Chapter 1, FTIR technique was another powerful characterization tool to characterize all kinds of conformations in polymers. Compared with XRD, it can provide more detailed information about the microscopic change of the materials. Below was the FTIR results of the samples added with GR and MWCNTs respectively. It was observed from these FTIR patterns that the samples consisted from more complicated chain conformations, not only including α and β chain conformations, a weak but clear γ peak on 1234 cm^{-1} were also observed.

Overall, just like the results in XRD, the results in FTIR showed not obvious difference among the samples added with varied concentrations of additives.

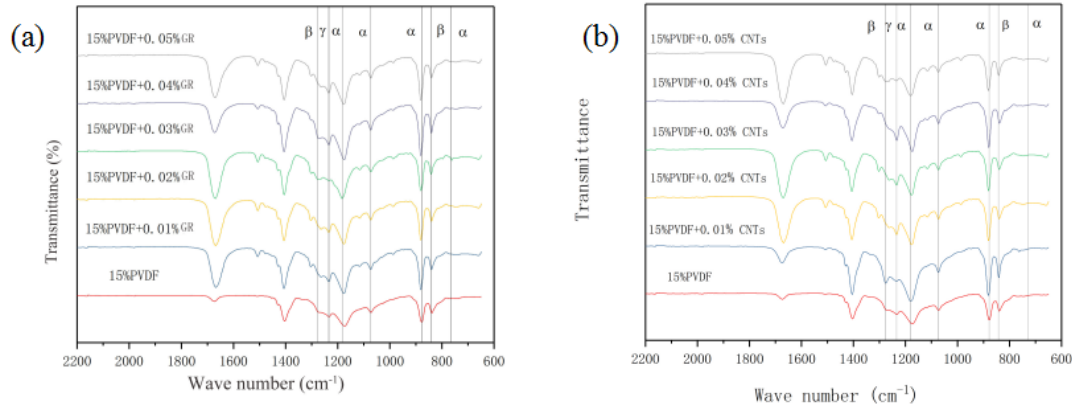


Figure 3.10 FT-IR results of PVDF thin films prepared with 15wt% PVDF in NMP solvent added with (a) 0.01-0.05wt% Gh additives; and (b) 0.01-0.05wt% MWCNTs additives.

Based on the data of XRD and FTIR, the content of β crystal phase and β chain conformation can be calculated respectively. As mentioned in Chapter 1, the XRD can characterize different lattice plane in crystal material. Through the analysis of a specific peak (generally the strongest one), the β phase crystallinity of material can be estimated. In FTIR, the real object of testing was the specific atom group in different chain conformations. Thus this technique can be used to calculate the content of β conformation in the solid state as a whole (including crystal part and amorphous part). The calculated β phase crystallinity and β contented were listed in Table 2.1 below. It was clear that both MWCNTs and GR can improve the crystallinity of PVDF. And compared with pure PVDF, the MWCNTs and the GR can increase the crystallinity of 16.09 in pure PVDF to about 30% and 60% respectively, which approved that both additives can obviously promote the crystallization. It was also seemed that the concentration of additives didn't quite affect the crystallization, no matter added with MWCNTs or GR. That was because in both additives, the mechanism for the promoting of crystallization, was based on the nucleation. Both MWCNTs and GR can actor as good nucleation agent, which provide the nucleation position (nucleus) with lowed energy barrier. However, adding more nucleus cannot furtherly increase the crystallinity if there were already enough amount of nucleus in material. Under this condition, other factors such as temperature, which can influence the grain growth,

will become the dominant effect to decide the crystallinity. In addition, it was also obvious from the results that the adding of GR and MWCNTs had little influence on the transformation of β chain conformations. No matter it was pure PVDF, or samples with GR and MWCNTs with varied concentration, the β conformation content $F(\beta)$ was stable around 0.75. This phenomenon corresponded well with our theoretical expectation. According to our previous discussion, the solvent influenced the $F(\beta)$ majorly through changing the polarization of the media or changing the evaporation time. It had never been reported that the GR or MWCNTs additives can dissipated in molecular/ion scale to change the polarization of solvent. They can also not, by any means, influence the evaporating behavior of solvent. Unless other mechanism were discovered, there was not any meaningful influence of additive GR or MWCNTs on the β conformation transformation.

Table 3.2 The crystallinity and β content of samples added with additives

Additive	wt%	crystallinity (%)	F(β)
Pure PVDF	0	16.09	0.81
Multiwall Carbon Nanotubes (MWCNTs)	0.01%	32.44	0.83
	0.02%	37.77	0.73
	0.03%	28.12	0.67
	0.04%	36.69	0.79
	0.05%	32.75	0.76
Graphene (GR)	0.01%	52.05	0.73
	0.02%	62.11	0.73
	0.03%	44.01	0.69
	0.04%	59.42	0.83
	0.05%	68.27	0.74

Although it was denied that the GR and MWCNTs had any influence on the β conformation transformation. Their enhancement effect on the crystallinity of the β phase was proved, and this effect can also be applied in our processing to promote the piezoelectric properties. They can provide our printing process with high controllability. The optimal parameters of the PVDF solution, such as wt% of the PVDF and MWCNTs additives, were determined to obtain the optimal β -crystalline composition and surface morphology. At the same time, it was more important to look for other additives that can really improve the β conformation transformation. Some kinds of organic salts were considered as the most promising candidates by the author. It

was found in table 3.2 as below that with the adding of 3 wt% organic salt tetrabutylammonium chloride (TBAC) in 20wt% PVDF-DMF solvent, the conductivity of the solution increased from 2.6 $\mu\text{S}/\text{cm}^2$ to 1969 $\mu\text{S}/\text{cm}^2$ (about 760 times higher). And it was widely accepted that the conductivity was an important indication of the polarity in organic solutions. Thus this result strongly indicated that the organic salt TBAC can dramatically promote the polarity of PVDF solutions. It was extremely interesting that what this kind of additive will perform in our printing process.

Table 3.3 Electrical conductivity of the solvents and polymer solutions⁷⁸

Solvent composition and additive	Conductivity without PVDF ($\mu\text{S}/\text{cm}^2$)	Conductivity with 20 wt% PVDF ($\mu\text{S}/\text{cm}^2$)
DMF/acetone 60/40	1.6	2.6
DMF/acetone 60/40 + 3 wt.% acetic acid	10.2	4.1
DMF/acetone 60/40 + 3 wt.% TBAC	3770	1969

3.2.4. The effect of voltage on β phase production

From the theoretical analysis in Chapter 2, the electrical field was considered as the basic and the most important factor to decide the conformation of PVDF chain. Various DC voltages from 3kV to 6kV were applied in this work. It should also be pointed out that a high applied voltage resulted in smaller diameter of printed fibers, which was consistent with the results of previous EHD-based processes. On the contrary, at lower voltage, the applied electric field can not produce enough force to produce Taylor cone, which will lead to unstable polymer droplets, resulting in thick ejection which is difficult to control. In this study, when applied a voltage lower than 3kV, the ink jet won't eject from the needle, and the printing process cannot normally get started.

All of the XRD patterns in Figure 3.9 showed the combination of α phase ((020) peak at 18.4° and (002) peak at 39°) and β phase ((110) peak at 20.8°). In the black curve in representative of

sample printed in 3kV, both the peaks of α phase and β phase were strong. With the increase of applied voltage, the peaks of α phase turned weaker and flatter, while the peak of β phase became sharper, which was in good agreement with our theoretical anticipation. In fact, the results showed that, the major phase in PVDF became β phase when the applied voltage increased above 4kV. In the curves of samples printed in voltage higher than 3kV, the (020) peak at 18.4° of α phase became unclear. But the (002) peak at 39° of α phase can still be observed in all of the samples. The sample with pure β phase cannot be obtained only depending on the electrical effect with limited voltage.

Because the increase of voltage can also reduce the dimension of ink jet from the needle. Higher voltage can make each layer of printed PVDF thinner, thus increase the average evaporation time, which will furtherly promote the phase transformation. Increasing the voltage were always consider beneficial for the piezoelectric performance of the printed PVDF thin film. However, it also had its limitation. Especially when the electrical voltage exceed the air breakdown voltage, there will be more and more arcing produced between the needle and the substrate, which could influence the stability of the processing, reduce the quality of the thin film, and potentially damage the instrument.

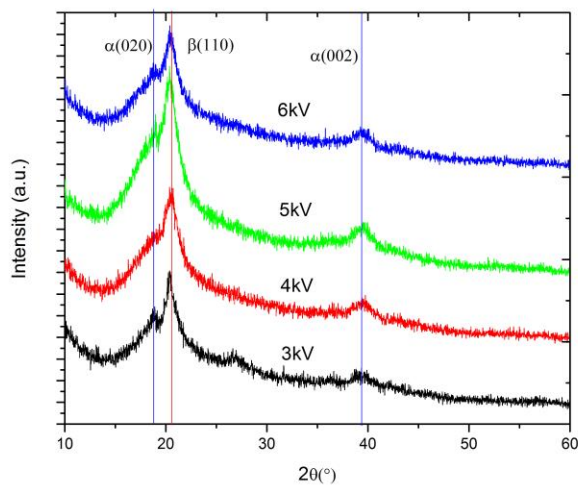


Figure 3.11 The XRD pattern of 14wt%PVDF in NMP under different voltages from 3kV to 6kV

3.2.5. The effect of printing speed on β phase production

In this study, the adjustment of printing speed was majorly through changing the diameter of needles. The needles with varied diameter could produce the ink jet with different dimension. However this could bring a new problem. Suppose with replace the 24# needle with diameter of 0.3mm to the 22# needle with the diameter of 0.41mm. The amount of ink arriving at the substrate will increase a lot within the same amount of time because each ink jet fiber can carry more amount of ink than before. Under this condition, in order to conduct the process continuously, it was still required that each layer be evaporated before the next layer getting started. And to make sure the increased amount of ink be evaporated in time, the substrate temperature should be elevated at the same time. For excluding the effect of temperature when studying the influence of processing speed, it would be better to apply the same substrate temperature on those needles with different dimensions. Thus those substrate temperature was relatively higher than the normal substrate temperature adapted to the smaller needles (about 70°C for any samples).

The demand for the study on processing speed originated from the study on the green solvent GBL. It was mentioned before that this solvent need a high processing speed to avoid the abundant evaporation of the Acetone during the printing. So a larger needle was tried for this solvent. Then it was found that the processing speed can make a great difference in this process, as the Figure 3.10 showed. It was distinct from the variation of solvent concentration, the varied dimension of needle can produce huge differences in the amount of ink arriving at the film surface within equal periods of time, which will ultimately result in the different thickness of each layer. In the sample prepared with 24# needle, because of the relative lower processing speed, the average time under electrical field was longer, so a high transformation ratio to β phase can be observed. On the contrary, in sample prepared with 22#needle, the higher processing speed led to the much higher percentage of α phase. As shown in the red cure of the Figure 3.10, the α peaks (020), (001), (002) can be clearly observed. This phenomenon made the replacement of solvent using GBL even more difficult. And this explained why the green solvent GBL still cannot become a real option in this area. In the future, adding some TBAC additive into GBL solution may become the solution for this problem. As discussed in subsection 3.2.3,

this additive had a large capability to improve the polarity of organic solutions, which can optimize the β phase production. And if it can increase the processing speed without sacrifice the β phase production in GBL solution, this green solvent would really be considered as a promising alternative to those solvent with high toxicity.

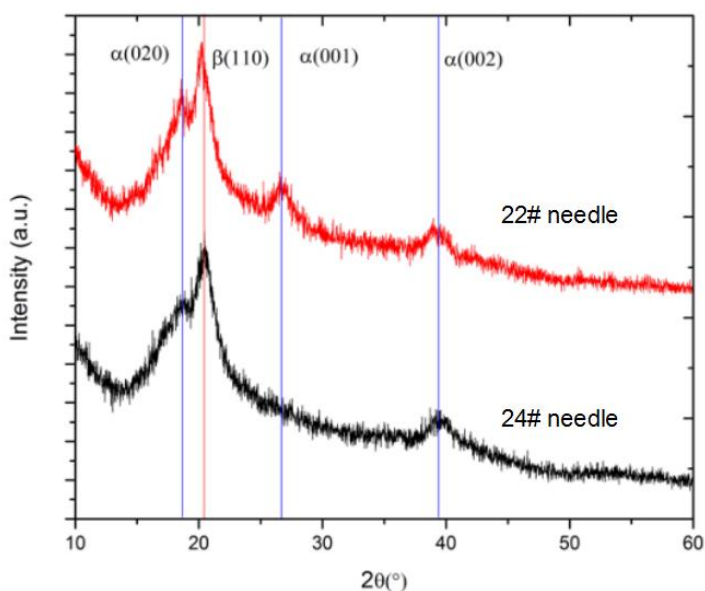


Figure 3.12 The XRD patterns of PVDF thin films prepared in GBL solution using different types of needles.

The similar influence of printing speed on the β phase production can also be observed in NMP solution as shown in the Figure 3.11 below. For the red curve in representative of samples prepared using 21# needle, the α peaks (020) and (001) can obviously be observed. All of peaks in red curve exhibited low intensity, compared with the strong and sharp β (110) peak in black curve, which indicated high percentage of amorphous phase in sample with high processing speed. Thus the high printing speed could not only reduce the β transformation, it may also hinder the procedure of crystallization.

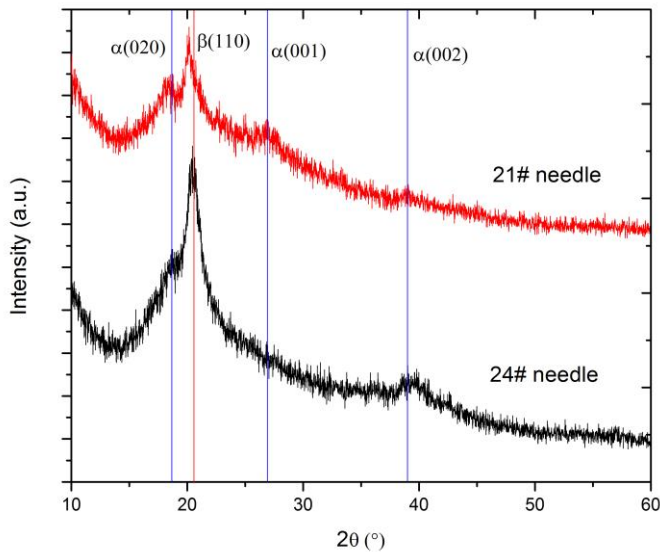


Figure 3.13 The XRD patterns of PVDF thin films prepared in NMP solution using different types of needles.

It should be noted here that in other literatures, especially those processed by melt printing or extrusion⁷⁴, the faster processing speeds usually brought a high β phase production than slower speeds. Apparently, this conflicted with the results in this study. It was meaningful to discuss the fundamental reason behind this phenomenon.

Firstly, in melt extrusion, fast printing speeds usually produced higher stretching stress than slower speeds. And this higher stress field likely induce more β phase, according to our previous theoretical analysis. While in the solution printing process, this stretching effect can be ignored.

Secondly, in melt printing/extrusion, the optimal strategy to obtain a higher β phase production was to produce the thin film with high amorphous percentage. And the amorphous phase can easily transform into β phase in the subsequent poling procedure. If there were too many crystallized PVDF chain produced (most crystal formed in melting temperatures were α phase) in forming procedure, the transformation to β phase in the subsequent step became more difficult, because the α crystal phase was stable and it will need extra energy to be activated into the

amorphous intermediate state. Thus, the higher processing speed, which was beneficial for the amorphous phases, will finally be beneficial to produce β phase in melt/extrusion process.

However in the solution EHD printing, the strategy was on the totally opposite way. Because the in-situ electrical field applied during printing, the best option was to take advantage of the optimized conditions (high electrical field, low temperature, carbon backbone chain freely in solution state) to finish the whole transformation in one step. At this time, the goal was no longer to obtain the high percentage of amorphous phase. And as a result, it was needed to reduce the printing speed to provide sufficient time for the phase transformation to occur.

3.2.6. The effect of post printing treatment

After the printing, there were still some opportunities to additionally optimized the thin film. Because a lot of β conformations remained in their amorphous state that can be finally crystallized into β crystal phase. It was widely believed that the piezoelectric performance of PVDF was decided by the content of β crystal phase. Thus if the crystallization process can be promoted in the as-printed PVDF thin films, and at the same time the reverse transformation of β conformations being prevented, then the materials with optimal phase composition can be obtained. For achieving this goal, two important aspects should be considered:

On one hand, curing (annealing) was the general method to promote the crystallization in amorphous materials. However simply increasing the temperature, there will be a great risk of reverse conformation transformation from β to α . According to the analysis in Chapter 2, when applied a higher temperature, the driving force for the reverse phase transformation will become stronger. The solution for this problem also rested on Chapter 2. Since the electrical field was considered as equally important factor to decide the driving force in the phase transformation, it was easy to think about conducting the curing and at the same time apply the electrical field to offset the adverse impact of high temperature on the Gibbs free energy change.

On the other hand, since the goal in this study was to develop the all-printed smart system, it was natural to consider about the possibility of integrating this post printing treatment methods into

our existing platform. And this idea looked feasible. For the curing procedure, the heating plate that already installed under the substrate on the printing platform can be utilized. And since the needle can provide the electrical field during the printing process, the empty needle connected with a power applier will play the similar role after printing in the similar way. The setup of the integrated post printing treatment instrument was shown in Figure 3.12.

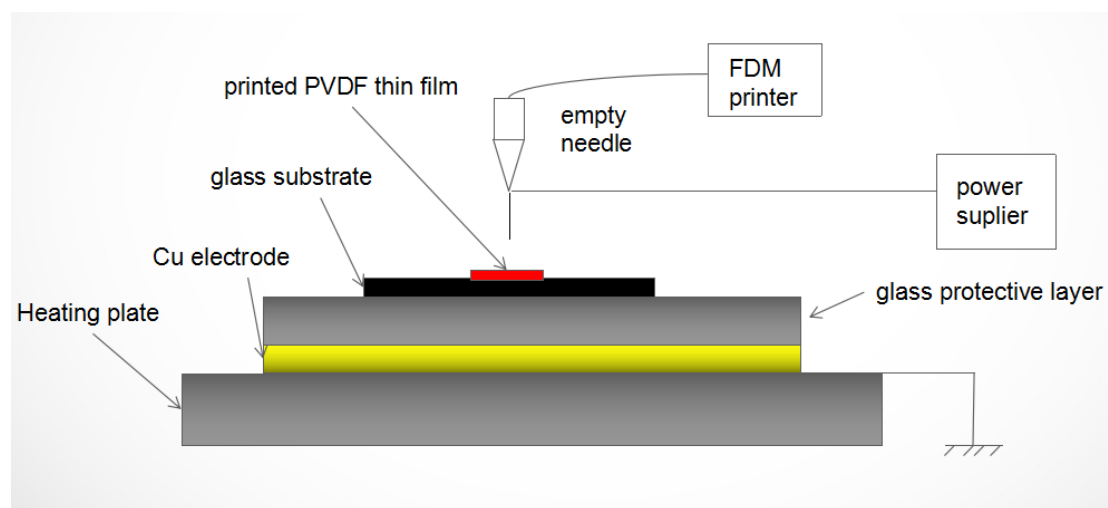


Figure 3.14 The integration of poling and post heat treatment procedure in the printing platform

The curing procedure was conducted in 70°C for 1 hour, under the varied voltages from 2kV-6kV. The results were shown in Figure 3.13. In the as-printed sample, as discussed before, the PVDF thin film with β phase was obtained. From the black curve in the Figure, a strong β (110) was observed. When conducting the curing process through the heating plate on the platform for a long time, the reverse phase transformation would occur. It was found from the red curve in the Figure 3.13 that even 2kV voltage was applied, the occurrence of this reverse transformation was obvious. In this case, the major phase in the sample became the α phase. Then as the increasing of the applied voltage, it was found that when the value of voltage exceeded 4kV, the reverse transformation can be effectively restrained. In the curves of 4kV and 6kV, not only the major phase in the samples were still β phase, a stronger and sharper shape for the β (110) peak than the as-printed sample was observed. This result proved that the crystallinity of the PVDF thin film can be effectively controlled without sacrificing the β phase production through this electrical

assisted curing processing, which would result in the final enhancement of the piezoelectric performance. And both the heating plate and the electrical supplier can be successfully integrated into the printing platform.

Researchers used to apply the sequential treatment in which they first applied ‘annealing and cooling-pressing’ or ‘pressing-annealing and cooling’, and then conducted poling process⁴. This sequential treatment were also considered a useful method to optimize the piezoelectricity of PVDF. However similar to this in-situ poling in printing process, the in-situ poling in heat treatment had its advantage over the conventional sequential treatment on that, it can prevent the formation of α phase crystal during the curing. It should be noted that once this stable α phase already formed, it would be much more difficult to transform it back in the sequential poling process.

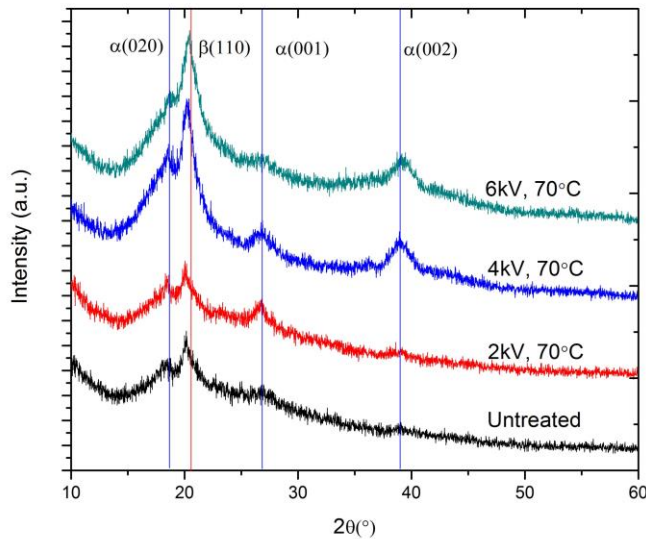


Figure 3.15 The XRD patterns of sample as printed and samples cured in 70°C for 1hour under the voltage from 2kV to 6kV.

Other than the curing process, a post-deposition electrical poling was required to align the dipoles. It was mentioned in Chapter 1 that there were a lot of misunderstanding in the concept of poling in this study. Strictly speaking, the poling should specifically denote the alignment of dipoles or the ferroelectric switching. However, it was found from this study as well as several

previous studies that, the applied electrical field can also be used to promote the β phase transformation and enhance the crystallinity. And in some cases, this procedure was conducted along with the alignment of dipoles in one step. As a result, all of those steps applied electrical field were called ‘poling’ as a joint name in this area. At first, this joint name was called for convenience. With the deepening of research, it was found this terminology can lead to confusion and sometimes even disturb the research. Thus in this study, the term ‘poling’ was specifically used to denote the alignment of dipoles to prevent misunderstanding. Now that the PVDF samples with the optimized β phase content and crystallinity was obtained. The research results associated with the poling procedure were included in the following chapter.

4. The integration of the poling process into the printing platform

The poling process of piezoelectric film was usually the step following the deposition of electrode. In conventional electrode poling, two electrodes on both sides should be deposited before poling, while in the corona poling, one electrode is required before poling. And because the printing of electrode and conductive wires was not included in the scope of this thesis research, the developing of poling technology on the printing platform should be conducted after the printing of electrodes. Some preliminary research can be conducted in advance, and if it was possible to process the poling on the as-printed PVDF films, this sensor printing technology can gain more opportunities in varied applications. Thus, the major concern in this chapter was to explore the method to integrate the poling procedure on the printing platform before the deposition of electrode on the thin film.

The polarization process of polymer will destroy its symmetry and form piezoelectric properties. Symmetrical damage has not only been observed in general porous polar polymers, it also has been reported in new hollow porous or cellular space charge electrets¹⁰⁶. The piezoelectric effect in polar polymers was based on the directional arrangement of dipoles at the molecular level, such as residual polarization in ferroelectric domain or frozen polarization in amorphous state. Piezoelectricity was produced by the change of dipole density in the process of mechanical stress or electric field application. In this chapter, the structure of polymer chains, different preparation methods, polarization processes and their different properties are discussed. It should be noted that a special electret structure was brought by this EHD printing process, which could add in the asymmetry of the material. And this electret structure may result in changes of properties within the material which at last would influence the piezoelectric performance of printed PVDF thin films.

4.1. Conventional setup and parameters of poling processes

In the last chapter, some results about the crystallinity and the β phase formation mechanism in PVDF were introduced. But it was still far from the end of story, because our goal was to print the material with high sensitivity that could be applied in SHM which meant preparing the samples with high piezoelectric coefficient. In fact, any piezoelectric material needed a poling process to increase the piezoelectric coefficient. The scenario will be perfect if the poled sample can be directly obtained during the printing process. If not, can we find a way to integrate the poling into the current printing platform as being realized in post treatment step?

It was necessary to first understand the basic setup of the current poling methods. In the previous Chapter, most of the conventional methods were considered as two-step processes. Because in those methods, the first stage is to process the film without adjusting the microstructures and phases (usually with high percentage of alpha crystal phase and amorphous phase). Then the final products with high β crystal phase content were obtained by the sequential steps of stretching and poling.

There has been a misunderstanding about the concept of poling for a long time. The strict concept of poling should be the orientation of domain. But in PVDF, because the electrical field can induce the dipole inside the chain, people thought it as part of poling. In fact, to produce the beta phase is different from the real concept of poling. Let's start this section by analyzing two of the most frequently used methods: the electrode and corona poling to see how we can find the poling process that can integrate the poling process into the printing platform. In electrode poling, the two sides of thin film surface are all required to be deposited with electrode. And then, DC or AC voltage was applied throughout the thickness. The whole sensor will be immersed in Si oil to prevent the air bubble existed in the thin film to become the weakness during the poling, and as a result damage the thin film structure. In our printed thin film, first we cannot immerse the structure in the Si oil, Second, the solution printed thin film has much higher porosity than the common one. It looks the electrode poling is not fit for our goal. As to the corona poling, only one side of electrode was deposited. The other side is the needle with a high voltage. At first glance, this method is similar with the setup in our printing system. The corona poling can apply

a much higher electrical field than the common electrode poling as shown in the table. And at the same time not easy to breakdown. It is because one side of electrode don't contact with thin surface of thin film. On our printing system, because the needle is keep moving, it has the potential to produce the surface with more uniformly distributed throughout the surface. As a result, we can consider this in-situ poling technology as one of the advanced corona poling. However, in our actual experiment, due to the limit of instrument, we cannot apply sufficiently high electrical field. This is the major problem of the current poling process.

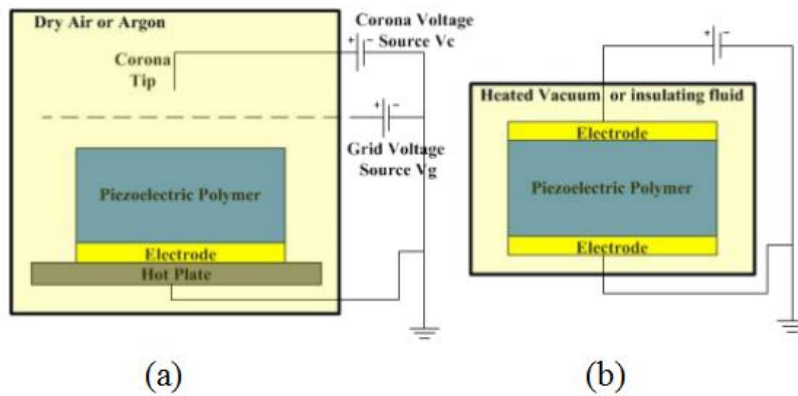


Figure 4.1 The schematic of (a) the corona poling system, and (b) the electrode poling system (conventional poling).

For the electrode poling, the upper limit for poling was clear. It should be close to the electrical coercive force in order to achieve efficient polarization¹⁰⁷. A poling electric field of 90MV/m was reported to cause electrical breakdown of the P(VDF-TrFE) film. Therefore, an electric field of 80MV/m was usually selected for this copolymer. As mentioned earlier, the crystallinity of beta phase was strongly influenced by polarization time and processing temperature. At a fixed polarization voltage, the crystallinity of beta phase increased with the increase of these two parameters. The dipole of PVDF was reoriented to the direction of applied electric field by polarizing the film by electric field. Therefore, the required condition¹⁰⁸ for the enhancement of the crystal beta-phase included appropriate electric field intensity and polarization time. In the polarization process, relatively high temperature will enhance the activity of molecular chains of PVDF films, thus slightly reducing the required electric field strength and increasing the speed of domain motion^{109 110}. This explained why the effect of polarization at 80 °C is better than that at

25 °C.

Generally, corona polarization devices included grounded substrates, polarization domes above the sample, and one or more needles (called corona needles) suspended above the sample. When an external voltage was applied to the needle, the air in the dome ionizes and produced ions to be ejected in the direction of the sample. Deposited ions created a charge layer on the surface of the sample and generated an electric field along the thickness direction. In order to ensure the uniform distribution of charged ions and control the potential of the film surface, it was necessary to install a conductive grid above the PVDF to keep the electric field above the sample stable. It was well known that only when poling is carried out at high temperature in the range of 80-120 degrees °C³¹, can α -PVDF transform to polar β -PVDF. Little is known about the same polarization effect at lower temperatures. However, when planning at high temperatures, it took a shorter time and a longer time at low temperatures¹¹¹. It was reported⁷² in unpolarized samples, the measured d_{33} value was only 1.65 pC/N. When high voltage was applied, the d_{33} increases to 25.3 pC/N after 15 minutes of 80 °C polarization. After 45 minutes, it can reach 34.4 pC/N. And then increased the polarization time, no significant increase of was found in the value of d_{33} was observed. It should be noted that although in many published papers, the symbol of d_{33} is negative, for convenience, the piezoelectric coefficient d_{33} recorded in many places is also often recorded as positive. The conventional parameters in corona poling were shown in Table 3.3 as below.

Table 4.1 Experimental conditions for corona poling process⁷².

Poling Temp.	Stretching ratio	Poling field	Grid voltage	Poling time (min)	Reference
20-120°C	2-5	10-80 MV m ⁻¹	_ ^a	_ ^a	95
103 °C	1-6.5	180 MV m ⁻¹	_ ^a	10	112
20-100°C	4.5	20-180 MV m ⁻¹	_ ^a	_ ^a	113
60 °C	1-7	280 MV m ⁻¹	_ ^a	30	114
_ ^a	_ ^a	8-10kV ^b	0.2-0.3 kV ^b	_ ^a	94
60 °C	_ ^a	125 MV m ⁻¹	5kV	1	115

^aNot reported.

^bNeedle voltage.

4.2. Orientation of the ferroelectric dipoles

The decisive factors for the domain switching as discussed in section 4.1, was poling field and poling time. The major goal in this section was focus on how to integrate the process into the printing platform. Firstly, some important issue in the switching mechanism in PVDF film were discussed. Then we estimated the effective poling time and poling field during printing. Since the domain switching time with respect to the varied field can be calculated based on the switching mechanism, a comparison can be made to decide whether the current conditions in the printing process were capable to produce sufficient polarization within the PVDF samples.

4.2.1. The spatial distribution of dipoles after poling

Some researchers believe that space charge (SC) is necessary for local compensation of dipole deflection during polarization¹¹⁶. Therefore, the interaction between polar grains and local compensation charge is of great significance to the further optimization of ferroelectric polymers.

There is a detection method called laser intensity modulation method (LIMM). This method uses the interaction between space distributed charge and laser beam to characterize the spatial distribution of polarizability and space charge, and then uses numerical deconvolution procedure¹¹⁸ to conveniently observe the evolution of polarizability and SC spatial distribution of polarized samples in the polarization process. From the Figure 4.2, it was exhibited that the profiles of polarization and SC were varied with the poling field. One distinctive feature was the non-uniform polarization distribution, which meant the domain wall cannot move throughout the whole film just like what happened in PZT¹¹⁹. During the movement of domain wall inside the crystal, the polarization process was realized and was compensated by the creation of SC. The polarization can also be brought by the rotation of the crystal particles. The real mechanism in the poling process may even more complicated. However, it was obvious that the distribution of polarization in the direction of thickness is not uniform. It always occurred close to the film surface, especially when the electric field was relatively low, which may also be related to the high surface sensitivity of LIMM. However, as the applied electric field increased, the polarization region extends toward the center of the film. Near the injected cathode (at $x/L=0.1$), the maximum polarizability increased obviously with the increase of electric field. The polarizability near the cathode was very low, which indicated that the injected electrons produced local charge compensation for the polarization. It was pointed out by Lovinger³⁸ that PVDF had a homogeneous across the thickness, and the side facing the positive electrode had higher much high piezoelectricity. This phenomenon can also be explained by the SC and poling distribution in this figure.

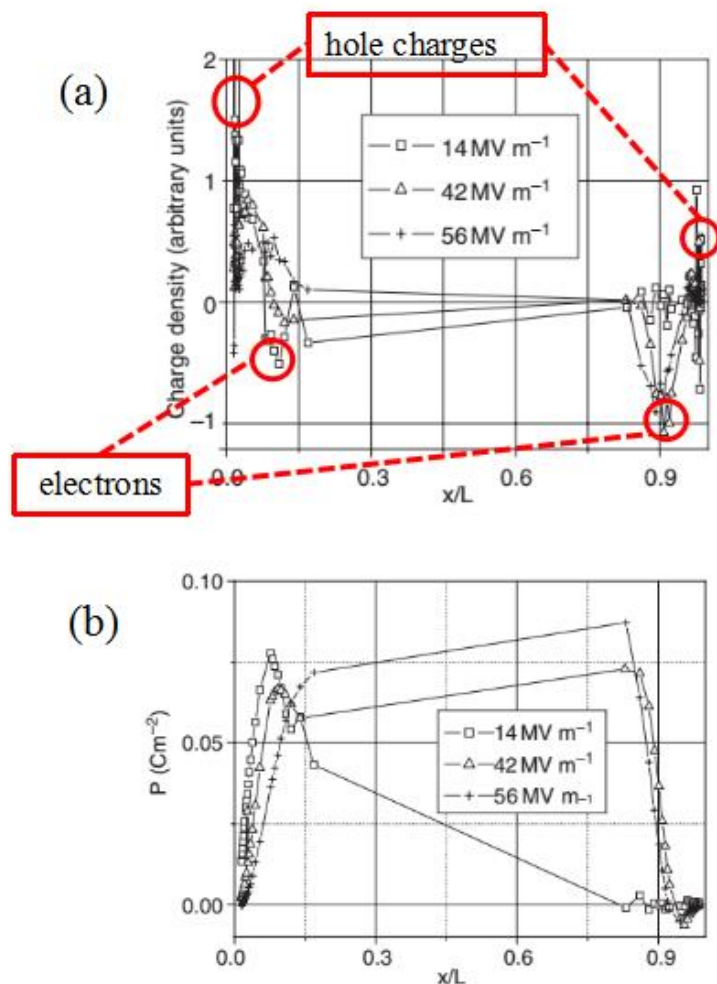


Figure 4.2 The space distribution of (a) space charges (SC) and (b) polarization along the thickness direction in PVDF thin films⁶⁴.

Whether PVDF is a real ferroelectric rather than a transferred charge electret was a controversial issue. Although the crystal structure had obvious dipole moment, there was evidence showing that the polarization of PVDF films was uneven (much higher polarization on the side near the positive pole), so the generation of piezoelectric properties of PVDF films may be the result of trapped charges injected into the electrodes at this moment. However, this anisotropy disappeared when a high polarized electric field was applied. Dipoles were reoriented in this process. Other typical phenomena accompanied with ferroelectricity, such as hysteresis loops and Curie transition, were also observed in PVDF at this time. As shown in the Figure 4.2, the distribution of SC and polarization became quite close after the electrical field of 42 MV/m or

higher was applied.

4.2.2. The estimation of effective poling time during printing and post treatment

The configuration of a needle electrode and an opposing plate electrode on the printing platform was often described as “point-plane” geometry. This geometry was used to study the injection of charges from the needle into a liquid medium that separated the electrodes. Observations and numerical modeling indicated that the electric field between electrodes in this configuration was highly nonuniform and increased at the needle tip. In the point-plane electrode geometry, the electric field along the axis of the needle at its tip had the form¹²⁰,

The configuration of needle electrodes and relative plate electrodes on printing platforms was usually described as "point plane" geometry which was often applied to study cases where needle charges were injected into the liquid medium of the separating electrode. Numerical simulations showed that the electric field between the electrodes in this structure was not uniform and increased on the tip of the needle. In the geometry of the point-plane electrode configuration, the electric field near the tip of the needle will be greatly amplified by the formula below ¹²⁰:

$$E = \frac{2V}{r \ln\left(1 + \frac{4d}{r}\right)} \quad (4.1)$$

where V is the applied voltage, d is the needle tip to plane distance, and r is the radius of the needle point.

Although the calculated electrical field around the needle tip was much higher than its nominal electrical field. The major function of this field was to facilitate the creation of Taylor cone. What really affected the physical process of β phase formation is the electrical field on the substrate. The needle was moving over the glass substrate back and forth. It was clear the real poling time for any region of the film was not the whole time expended on printing process. And the average time for the film processed under the poling can be defined as the “effective poling

time". This effective poling time can help us understanding the condition of poling during the printing and comparing the poling process with other studies. In order to estimate the effective poling time during printing, one should first know the potential distribution on the substrate plate underneath the needle point. A simple electric field model was established by COMSOL mathematical software. The model can visually display the distribution of electric field around the tip and the substrate. The Comsol multi-physical field has a powerful interactive environment for modeling and solving various scientific and engineering problems based on partial differential equation (PDEs). With this software, we can easily solve coupled physical phenomena. Because of the built-in physical model, the model can be constructed by defining related physical quantities (such as material properties, loads, constraints, sources and fluids) instead of defining basic equations.

The EHD printing device was mainly composed of needle tube, needle, high-voltage power supply, glass substrate plate and 3D printer. Considering that the load and motion conditions in the whole printing process were very complex, and these complex conditions will have a certain impact on the finite element analysis. So here they were all simplified in the simulation, omitting the factors that had little effect on the distribution of electric field, so it was simpler and more efficient to simulate the actual situation. The whole device was simplified into three parts: the needle, the air and the glass substrate. In the simulation, the diameter of the needle was 0.3 mm, the length was 10 mm, the size of the glass collecting plate was 40mm×40mm×1mm, the distance between the needle tip and the glass collecting plate was 2 mm, the bottom of the glass protective plate was 100mm×100mm×1mm, and the air contained the needle and the glass collecting plate. 6 kV DC voltage were applied to the needle, and the copper plate was grounded on the bottom surface of the glass collecting plate. Three modes of mesh generation were adopted, which named standard, refined mode and special refinement mode respectively. After meshing, the standard mesh mode consisted of 62365 domain elements, 15094 boundary elements and 688 boundary elements. The refined mode consisted of 154690 domain elements, 29472 boundary elements and 1102 boundary elements. The special refinement mode consisted of 1995502 domain elements, 119174 boundary elements and 4193 boundary elements. Considering the convenience of calculation and the reduction of the error, the refined mode was adopted.

In order to study the specific potential distribution on the glass substrate plate, the surface potential distribution was obtained by software simulation, as shown in Figure 4.3. The potential on the glass collecting plate decreased outward in a concentric circle, and the darkest potential was the point right beneath the needle. Potential existed in the air near the same surface on the glass collecting plate. This required us to consider personal safety during printing and keep away from glass collection panels. One-dimensional potential diagram of the surface potential of the glass collecting plate can be drawn directly, as shown in Figure 4.4. The Figure showed that the potential obtained its highest value of 152V at central point, this value reduced to 50V at 5mm from the center.

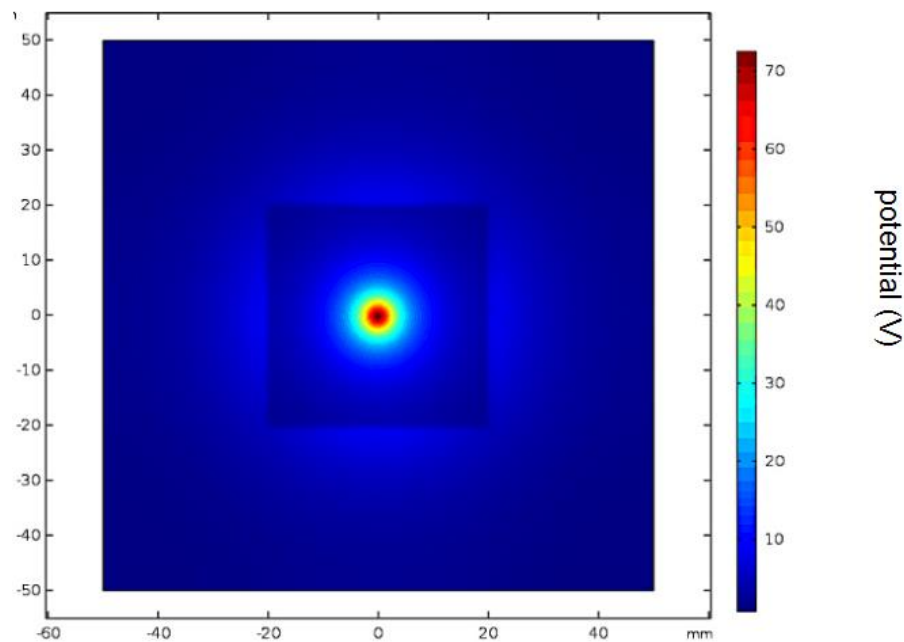


Figure 4.3 Surface potential map of glass collecting board

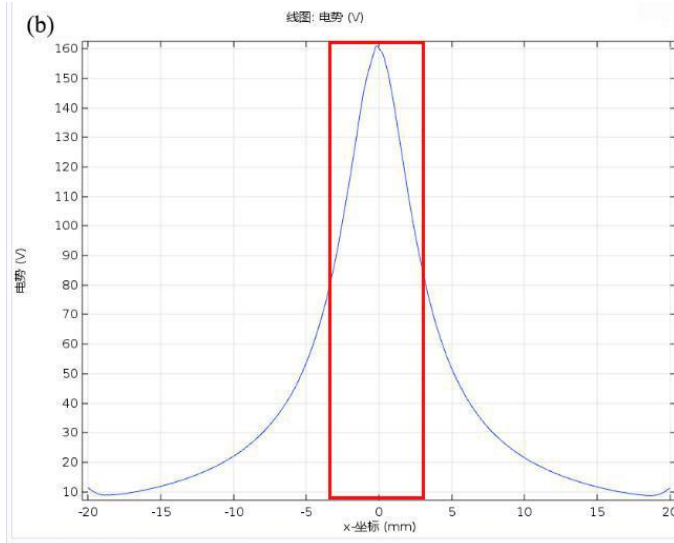


Figure 4.4 1-D potential map of substrate panel

During the poling with low electrical field, the polarization region almost concentrated in a very limited region around 1/10 of the whole thickness. This thickness corresponds to 6 layers during the printing. This unevenly distribution of polarization will deeply influence the piezoelectric property of PVDF thin film, we'll discuss it in detail to show how it will influence the sensitivity of PVDF. In this section, we just use this result to estimate the effective poling thickness, during the printing process. Previously we estimated that the effective thickness of the in-situ poling. In order to calculate the effective poling for the in-situ poling, we need to know how the electrical field is distributed on the substrate. The simulated result is easily obtained by COMSOL. For the simplification of the problem, we use the red rectangle to replace the simulated curve, and the effective region was considered as a circle with a radius of 3.5mm. Combining the calculated effective poling thickness and poling region, we can calculate the effective poling time for each layer. It is shown that, for the whole printing time of 80min, the effective poling time is only 0.66 min. When we apply a post printing poling, the process went back to the 2D process. Similarly, if we spend 80min on this poling, the effective poling time will be 7.6min, much better than the in-situ poling. Although we can expect some semi-liquid effect during the in-situ poling that could promote the orientation of domain. From the current calculation, the in-situ polling is not an effective poling method. In order to further advance the sensitivity of printed PVDF, more effort should be spent on the post printing poling procedure.

From this calculation, one can find the efficiency of poling during the printing was low: For the overall 80min of printing time, only 0.66min can be used for poling. There were two major reasons:

Firstly, there was only one needle that can influence very limited region on the thin film surface, and this needle was always moving back and forth. As a result, only very limited region from the surface can be polarized at any moment.

Secondly, the applied electrical field can only polarize a few layers nearby the surface of the PVDF film. And in AM process, the surface was continually replaced by the new printed layers. Thus, much poling time was spend on the poling of internal region of the thin film, which had little influence on the sensing performance of the PVDF thin film.

To address the first problem, the multiple needles structure or new design of the single needle may be applied to improve the field distribution on the thin film surface. To address the second problem, the post printing poling was required. Because in the post printing poling, there will be no newly printed layer during the process, and the poling time could be fully utilized on the surface layers. Then the average poling time can be easily calculated by the multiplication of effective poling ratio (0.11/1.14) and the total poling time (for example 80min), which was 7.6min. Compared with 0.66min in printing process, the post printing poling made a big progress. Although we can expect some semi-liquid effect during the in-situ poling that could promote the orientation of domain. From the current calculation, the in-situ polling is not an effective poling method. In order to further advance the sensitivity of printed PVDF, more effort should be spent on the post printing poling procedure.

4.2.2. Ferroelectric switching time

It should be firstly noted that the switching time is not exactly the poling time for the domains, only part of the polarization will remain after the applied electrical field is removed. But it can almost reflect the polarization time that is required for the polarization procedure of the samples.

The ferroelectric switching process can provide an analysis of the dynamic characteristics of polarization inversion. When the polarized electric field is not too strong, the switching time of ferroelectricity varies with the electric field intensity as follows:

$$\tau_s = \tau_{s0} \exp(E_a / E) \quad (4.2)$$

where E is the applied electric field, E_a is the activation field, τ_{s0} is the switching time at infinite field, known as ‘time factor’.

In reality, the applied electric field used in this equation should be the actual electric field strength applied on the film surface. However, in some applications, it is difficult to obtain its value accurately. Therefore, in this study, nominal electric field is usually used to replace the actual electric field. The experimental results showed that ferroelectric polymers such as PVDF and copolymer P (VDF-TrFE) follow the exponential law in a wide range⁵⁶. When the dynamic characteristics can be clearly described by equation 4.2, the switching process at low field strength is called external switching. In the external switching process, two mechanisms play the most important role. One is the nucleation of the domain with opposite polarization when the reverse field is applied, and the other is the growth of the domain with wall motion in the nucleated region.

When applied a higher applied electric field, the nucleation speed of the new domain is very fast, and the switching time mainly depends on the time required to move the domain wall with the domain growing. In this case, the dynamic characteristics of ferroelectric switches can be expressed by the following formula:

$$\tau_{ex} = \frac{1}{\mu(E - E')} \quad (4.3)$$

Where μ is the mobility of the domain walls and E' is a limiting field which is similar to coercive field strength.

The results show that in this case, there should be a minimum critical size of ferroelectrics

accompanied by a thermal activation process of ¹¹³. Because the polarization mechanism under low field intensity is mainly used in this study, we do not discuss it in detail here.

Since the applied electrical field was quite low in this study (only 1MV/m), the dominant switching mechanism was clearly extrinsic switching. It was found from equation (4.2), that the switching time can be directly calculated by the applied electrical field, as long as E_a and τ_{s0} is decided. There was still very limited data on E_a and τ_{s0} for PVDF, however the alternative data for P(VDF-TrFE) copolymers can be easily found in ¹²¹. And from¹²¹and¹²², it was found that the E_a and τ_{s0} values for PVDF and P(VDF-TrFE) copolymers was actually very close. So in this study, the E_a and τ_{s0} for P(VDF-TrFE) was used for the calculation of the switching time in printed PVDF thin film. It was shown in Figure 4.5 that the E_a was in proportional to the reciprocal of absolute temperature. Thus the E_a value for 20°C, 40°C, 60°C, and 80°C can be estimated from this Figure, as 1000MV/m, 920MV/m, 800MV/m, and 750MV/m respectively.

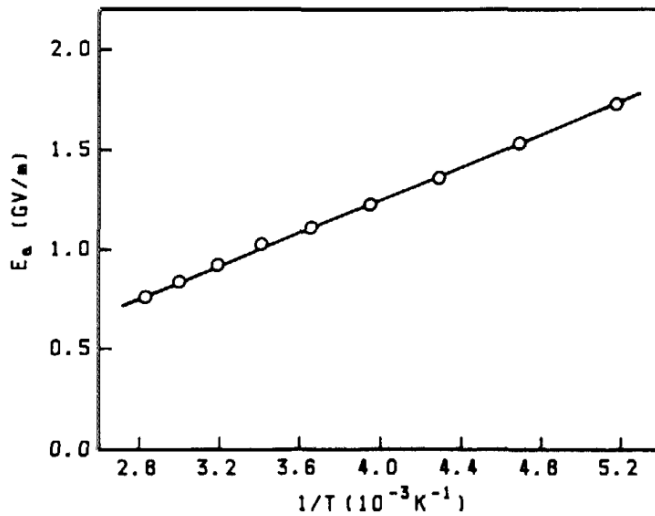


Figure 4.5 Dependence of the activation field E_a on the reciprocal of absolute temperature $1/T$ ¹²¹.

Figure 4.6 illustrated the dependence of switching time (τ) on the different values of applied electrical field. And from the combination of curves in Figure 4.6 and the equation (4.2), the τ_{s0} in 20°C, 40°C, 60°C, and 80°C can be deduced as 1.17×10^{-9} , 9.12×10^{-10} , 8.32×10^{-10} , and 5.50×10^{-10} respectively.

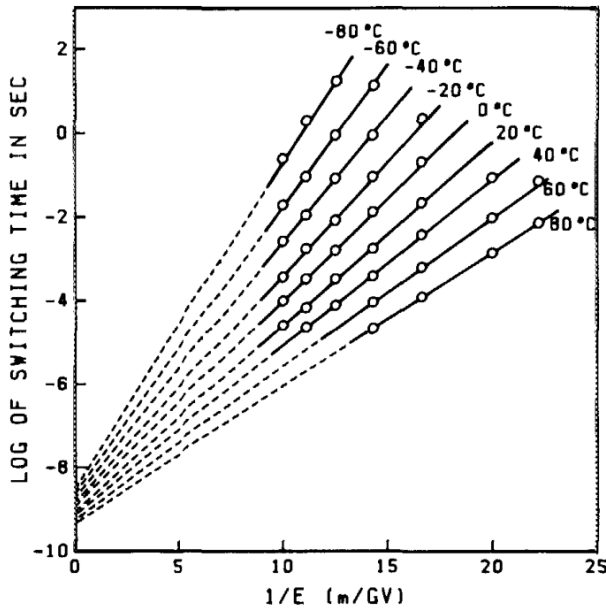


Figure 4.6 Plots of the logarithm of switching times against the reciprocal of applied field¹²¹.

Based on the value of E_a and τ_{s0} , the influence of applied field on the switching time under different temperatures can be obtained as shown in Figure 4.7. And from the previous analysis, there were three major factors that can influence the polarization behavior of the PVDF, including electrical field, poling time and temperature. Usually, the poling time applied is limited. If considering the switching time within 5 hours as meaningful, at least 24-33 MV/m were required. Because the switching time decreased exponentially with electrical field, the most efficient method was to increase the electrical field. However, the voltage generated by power supplier was limited, and it was difficult to reduce the gap between positive and negative electrodes too much. From the trend exhibited in Figure 4.7, as the temperature increased, the minimum electrical field can be reduced. As a result, the poling temperature higher than 80°C were usually applied. Under this temperature or higher, if electrical field of 27 MV/m were obtained, the switching can be finished within couple of minutes.

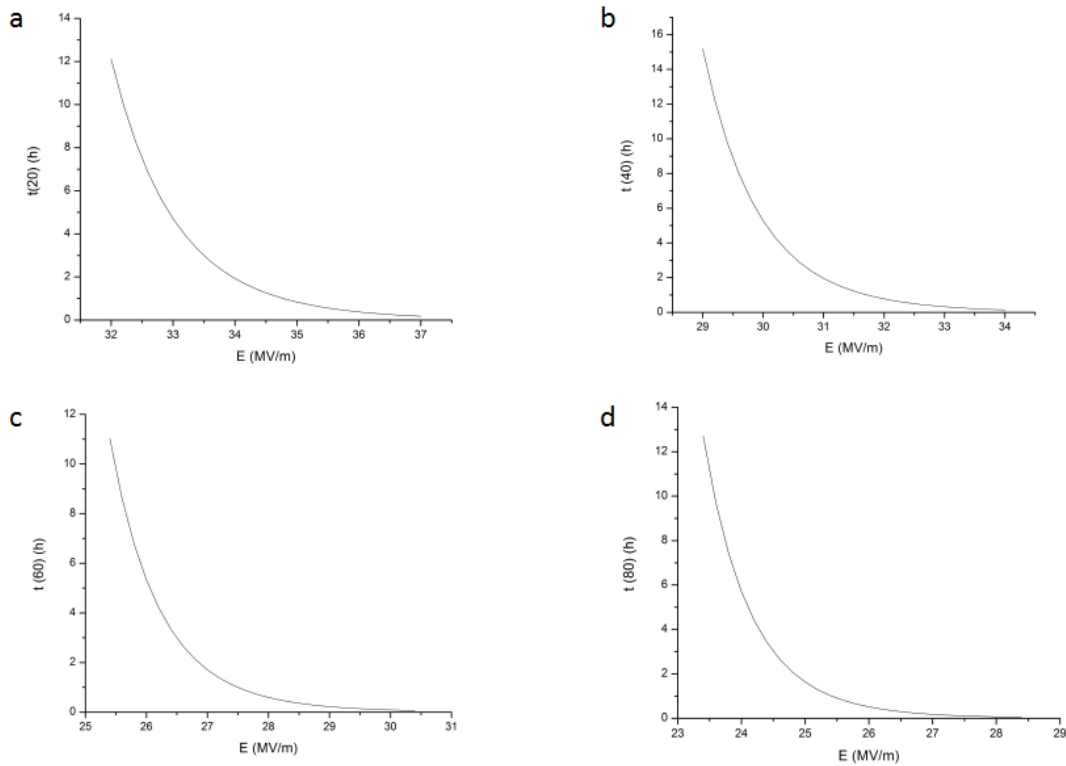


Figure 4.7 The varied switching time as a function of applied field in PVDF under different temperatures: (a) 20 °C, (b) 40 °C, (c) 60 °C (d) 80 °C

4.2.3. The design and promotion of the poling instrument on the printing platform

Based on the above analysis, there are three major method that can promote the poling process of printed sensor including increasing the effective poling time; raising the temperature and strengthening the poling field. Among the three factors, the strengthening the poling field is the decisive factor, because of the exponentially decrease of switching time with the electrical field.

Increasing the poling time: The understanding of poling process and the effect poling time was discussed using simulation with respect to the potential distribution on the substrate plate. Although there should be a huge difference between the real value and the simulated one, because of the corona currency between the needle and the substrate. In this case, we mainly apply this method to estimate the effective poling area around the tip position. Two designs for prolong the effective poling time were shown in Figure 4.8. In the first design, a electrode cap was setup above the printed thin film. The advantage of this design was that every minute of

poling time was used as effective poling time. The draw back was also obvious: this setup of poling system need a major rebuild of the current printing system which added up the cost and time-consuming. Other design which showed in Figure 4.8(b) was just made some modifications on the needle part: to change single need into multiple needles, and to add metal grid as what usually used in corona poling. This design was much simpler than the first one, and it fully took the advantage of the current printing platform. It had a better potential to be used in this sensor embedding technology.

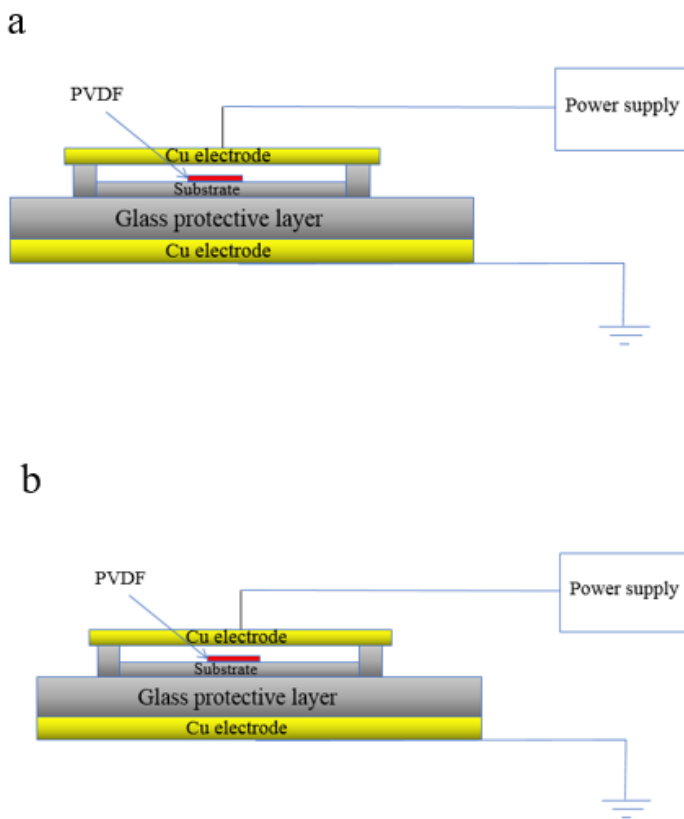


Figure 4.8 The designs for prolong the effective poling time: (a)metal cap; (b)multiple needles

Raising the temperature: It was shown in previous sections that raising the temperature can reduced the required poling time and poling field. And because high electrical field was applied, this method can also optimize the crystallization without worrying about the reduction of β phase. From this point of view, a temperature close to the melt point should be selected to reduce the required electrical field. It is simple to apply this method in the printing platform, because the

heating plate can be easily setup at the bottom of the substrate.

Strengthening the poling field: The major advantage in corona poling was that the poling field can be increased much higher than the air breakdown voltage. However in the printing platform, it is still necessary to consider the stability of the instrument. A high work voltage will seriously reduce the stability of processing and jeopardize the safety of the whole printing system. In the previous section, the relation between the domain switching time and poling field was discussed in detail. Considering the poling time was limited, and the upper limit of temperature was the melting temperature of 172°C, to apply a high poling field was unavoidable. We took poling temperature of 80°C as an example. Under this temperature, if a poling time less than 1h was considered as meaningful, a poling field of 25.5MV/m was required. According to the current setup of printing system, that meant the voltage of 133kV, which was unimaginable. The only option was to reduce the needle to electrode distance. The structure of the printing platform as shown in Figure 4.9 exhibited that the current applied voltage was 6kV, and the needle to Cu plate distance was 6mm, the nominal electrical field in our printing and post treatment was about 1MV/m, which was much lower than the required field strength. The possible method that can be used to reduce the electrode distance was shown as below:

The analysis of minimum tip to electrode distance:

1. Tip to substrate distance of 2mm can be reduced to 100 μ m if automatic control system applied.
2. PVDF film thickness of 40 μ m.
3. Protective layer and glass substrate of 4mm in total, can be removed.
4. Theoretically, the tip to electrode distance can be reduced to about 140 μ m.
5. Under this extreme situation, a 25.5MV/m field can be achieved by only 3.57kV applied voltage (worth trying!).

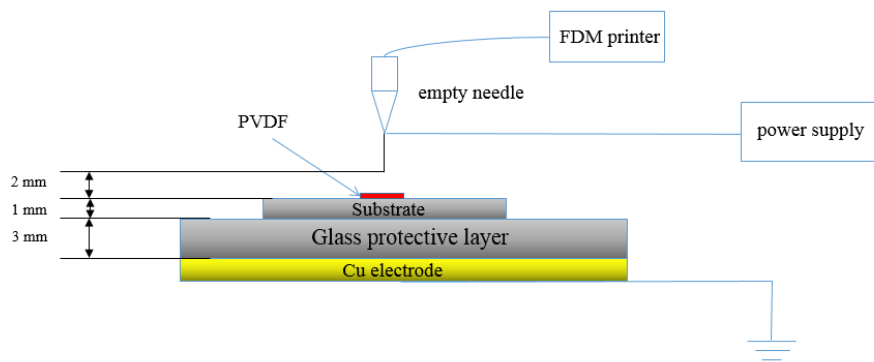


Figure 4.9 The structure of printing platform showing the needle to electrode distance.

All in all, the corona poling was capable to integrate in our current printing system, however it was difficult to obtain the saturated polarization based on the current instrument. At this moment, one may ask a question: “Is there a method that can improve the piezoelectric performance of material with very limited poling time?”, or in other words, “what if we can produce high piezoelectricity with unsaturated polarization?” This will be mentioned in the next chapter.

5. Sensitivity evaluation of the PVDF sensors

The major objective of this chapter was to characterize the sensing performance of the printed PVDF thin films. In this part, a film based piezoelectric sensor was fabricated and tested. The sensors consisted of one layer of printed PVDF thin film sandwiched by layers of electrodes. The printed sensors tested in this study were all as-printed which didn't experience any post poling step. The sensing elements were created by the optimized processing doped with Graphene (GR), which exhibited the highest β content and crystallinity. Both the 33 mode and 31 mode were operated with the sensitivity evaluation. The films' sensing performance was validated using a variety of experiments, including PFM method, d_{33} meter, cantilever beam method, free vibration testing, and hammer impact testing. All tests measured the voltage output of the films. Based on the results, it was concluded that the fabricated sensors exhibited promising sensitivity even without any post printing poling procedure. And the sensitivity of this printed PVDF thin film sensor can be further increased by post poling and other optimization in printing process.

In the previous chapter, we discussed the special process of the in-situ poling procedure for the printing PVDF. Although the effect of semi-liquid poling effect is not clear. We can see that the low efficiency of in-situ poling due to the extremely low effective poling time. There are several methods can be used to promote the poling process. But the real decisive factor is the electrical field. Because of the limit in the current printing system, we are not able to build the complete poling process based on this printing system right now. And before we can improve this poling process, we can first evaluate the sensitivity using those as-printed PVDF samples. The result of this chapter can be used to compare with future samples conducted with the post poling process.

5.1. Sensor preparation

In our research project, the electrodes in the smart layer should also be deposited like PVDF films. In order to evaluate the sensitivity of PVDF films in advance. We fabricated PVDF sensors based on traditional deposition and coating methods. As a sensor, PVDF film can use its voltage

output without external power supply or complicated circuit. Because of its high compatibility, it can be adhered to various structures and surfaces by simple bonding technology. The PVDF sensor used in this study consisted of a PVDF film sandwiched between the electrodes. Leads or copper were connected to the electrodes so that the response voltage can be measured. Possible methods of coating electrodes included screen printing with conductive silver ink. The resulting metallized layer is thicker (5-7 μm). This method provided additional strength and durability, making the film more suitable for mechanical applications. Silver-ink metallization also provided good surface finish and low reflectivity. Other coating technologies, including sputtering metallization, resulted in thinner electrode layers. Deposition thickness of various metals and alloys can reach 50-70 nanometers. Although this made the film more flexible, the metallized layer was not so strong and cracks easily due to repeated deformation. In addition, the surface of the sputtered electrode layer had a high reflectivity, which made it a low reliability target of the laser rangefinder. When the preparation of the electrode was completed, thin insulated copper wires needed to be connected to the electrodes. Finally, the translucent tape was used to package the whole sensor structure ¹¹¹.

When the electrodes on the upper and lower surfaces of the film contact for some reason, a short circuit will occur. This can interfere with the test results and even damage the equipment. Therefore, when the electrode preparation process is completed, each sample needs to be checked to eliminate short circuit. The samples with infinite resistance between the electrodes are considered qualified.

Wire is very important for the use of sensors, which will strongly affect the size and reliability of signals. In this study, thin copper wire (0.12 mm) coated with electrical insulation was used. The insulating layer prevents unexpected contact between the lead wires, which will be removed near the connection point with the sensor. There are many ways to insert wires. However, due to the size of the sensor, the application of common methods such as low temperature welding and epoxy resin is limited. Simply using Scotch tape as an adhesive is the most effective and commonly used. In order to provide a good electrical connection, an insulating layer of about 2mm in length was removed from the end of each wire using sandpaper. Exposed leads were placed on each side of the sensor and need to be slightly separated to avoid possible connections

between them. Then, the sensor and the wire were fixed between two layers of tape.

Several types of electrodes were also considered: Au deposited by physical vapor, CircuitWorks CW2400 conductive epoxy resin and etc. CircuitWorks epoxy resin adheres well, but eventually becomes fragile and cracks due to repeated use. Ejector coated Au electrodes (300nm) adhere well, but because printed PVDF films often have many micro-holes, this method can easily lead to local short circuit, thus reducing the effective area of PVDF films ⁷⁴.

The commercially available PVDF sensor LDT1-028K (Measurement Specialties Inc.) was also used in some of the experiments performed in this research as control specimen. Figure 5.1 showed a diagram of the LDT1-028K sensor. The sensor consists of a 28 μm thick PVDF film sandwiched between two 6 μm thick silver ink electrodes. This assembly was sandwiched between two 55 μm thick Mylar sheets. Two leads were attached to the sensor. The capacitance of the LDT1-028K PVDF sensor was measured as 1.57 nF.

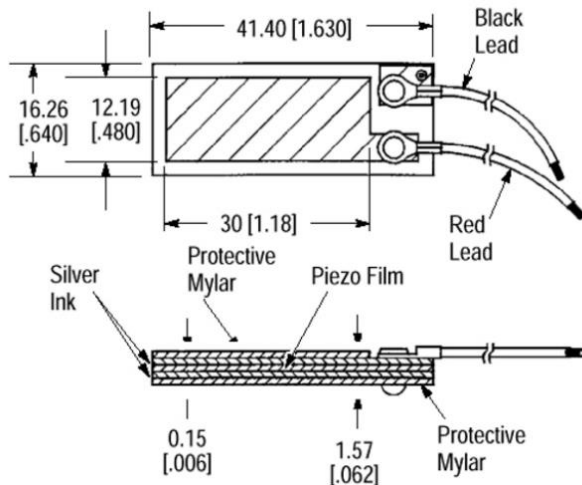


Figure 5.1 PVDF sensor LDT1-028K¹²³.

The electric field generated by the PVDF sensor and the stress acting on the PVDF sensor were the two parameters that will be required for analysis of the experimental and simulation-based data in this research. The sensing formulation or strain-field formulation of the linear piezoelectric equations was discussed early in chapter 1. The basic properties of the LDT1-028K sensor were listed as below.

Table 5.1 Properties of the LDT1-028K sensor¹²³.

Symbol	Parameter	Value	Units
d_{31}	Piezoelectric strain constant in the 1 direction	23×10^{-12}	$\frac{\text{m/m}}{\text{V/m}}$
d_{33}	Piezoelectric strain constant in the 3 direction	-33×10^{-12}	$\frac{\text{m/m}}{\text{V/m}}$
g_{31}	Piezoelectric stress constant in the 1 direction	216×10^{-3}	$\frac{\text{V/m}}{\text{N/m}^2}$
g_{33}	Piezoelectric stress constant in the 3 direction	-330×10^{-3}	$\frac{\text{V/m}}{\text{N/m}^2}$
ϵ/ϵ_0	Relative permittivity	12-13	
E_s	Elastic modulus	2-4	GPa
ρ_s	Mass density	1780	kg/m ³
h	Film thickness	28	μm

5.2. Piezoelectric characterization in 33 mode of operation

In the 33 mode of operation, the stress was applied in the 3 direction (or compression direction). To effectively use the PVDF sensor in 33 mode, the sensor must be positioned on the structure in such a way that it fell directly in the path of the applied load. In other words, this meant that the PVDF sensor was compressed in the thickness direction in 33 mode. Thus, the PVDF sensor acted as a pressure sensor in 33 mode. The piezoelectric stress constant of relevance in this mode is g_{33} . The structure must be rigid in order to use the PVDF sensor in 33 mode.

Static sensitivity is defined as the ratio of the output voltage to the pressure acting on the PVDF material in a certain direction.

$$K=V_o/P \quad (5.1)$$

Figure 5.2 showed the circuit of a “sandwich” PVDF film sensor. The open circuit voltage developed along the film thickness direction is

$$V_0= -g_{33} \cdot P \cdot h \quad (5.2)$$

where g_{33} is the piezoelectric stress constant, P is the applied pressure along 3-direction, and h is the thickness of the PVDF film.

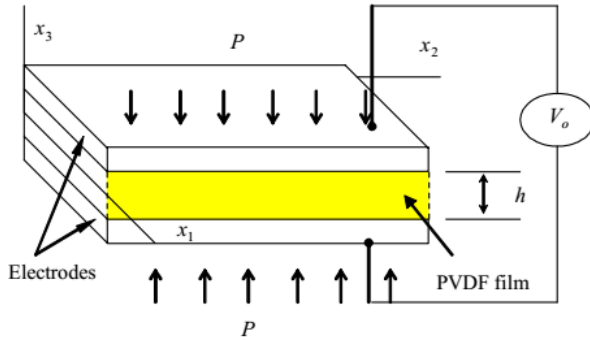


Figure 5.2 PVDF film open circuit. (operated in d_{33} meters)

Equation (5.2) described the basic sensor mode of the piezoelectric device. In our test, the second and third terms were ignorable. Thus, (5.2) turn out to be:

$$D_j = d_{ij} T_{kl} \quad (5.3)$$

Where D_j is the electrical dislocation, d_{ij} is the piezoelectric charge constant, and T_{ij} is the mechanical stress. The piezoelectric charge constant d_{33} can be determined from (5.3).

The voltage across the film was related with the charge on the surface of the sensor as followed:

$$V_{\max} = \frac{Q_{\max}}{C} \quad (5.4)$$

where V_{\max} is the maximum voltage measured across the sensor, Q_{\max} is the maximum charge on the film surface induced by the applied force, and C is the capacitance of the sensor.

If the capacitance of the sensor is known, the charge generated on the electrode surface of the

sensor can be determined according to the voltage measured on the sensor. This enables the use of oscilloscopes to simply measure the charge on the sensor and derive its function over time. In order to characterize the d_{33} coefficient of the sensor, the pressure applied on the PVDF wafer can be measured using the commercially available piezoelectric weighing sensor. Then the voltage response function of the printed material is recorded by an oscilloscope. Finally, the piezoelectric charge coefficient d_{33} can be simply determined according to (5.4).

5.2.1. Piezoelectric Force Microscopy (PFM) test

In order to further the understanding of piezoelectric behavior in the sensor, surface characterization analysis was carried out with the use of Atomic Force Microscopy (AFM). The studies were focused on determining the relationship between microstructures of PVDF and its piezoelectric behavior. Atomic force microscopy was a technique which allowed for detailed measurement of the material surface topography with a resolution as low as a few nanometers. A diagram of AFM operation was shown in Figure 5.4³³.

Atomic force microscopy (AFM) is a technique which can measure the surface morphology of materials as low as several nanometers in detail. Its schematic diagram is shown in Fig. 5.4³³. In order to further study the piezoelectric behavior of the sensor, atomic force microscopy (AFM) can also be used to characterize the surface. The research focuses on microstructures of PVDF with respect to its piezoelectric behavior. In order to simulate the piezoelectric behavior in PVDF, an applied electric field (Sinmeter, HY3020E) was applied to the film during the experiment. This resulted in charge accumulation and surface morphology changes induced by applied electric field. Figure 5.3 showed the piezoelectric response image of PVDF using a piezoelectric stress microscope (PFM SPA400). The AC bias voltage was 15 V and the frequency was 60 kHz.

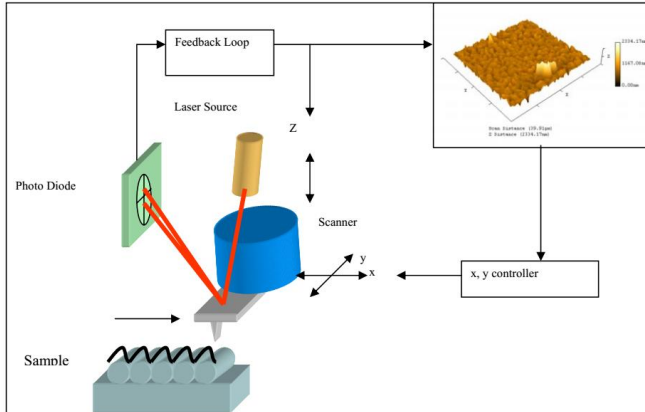


Figure 5.3 Schematic diagram of AFM operation ¹²⁵.

Two printed PVDF samples were randomly selected to conduct the PFM measurement from 50V to 120V as shown in Figure 5.5. For each data point, the voltage was varied from 0V all the way to the peak value (offset), thus the V_{p-p} corresponded to the maximum value of displacement.

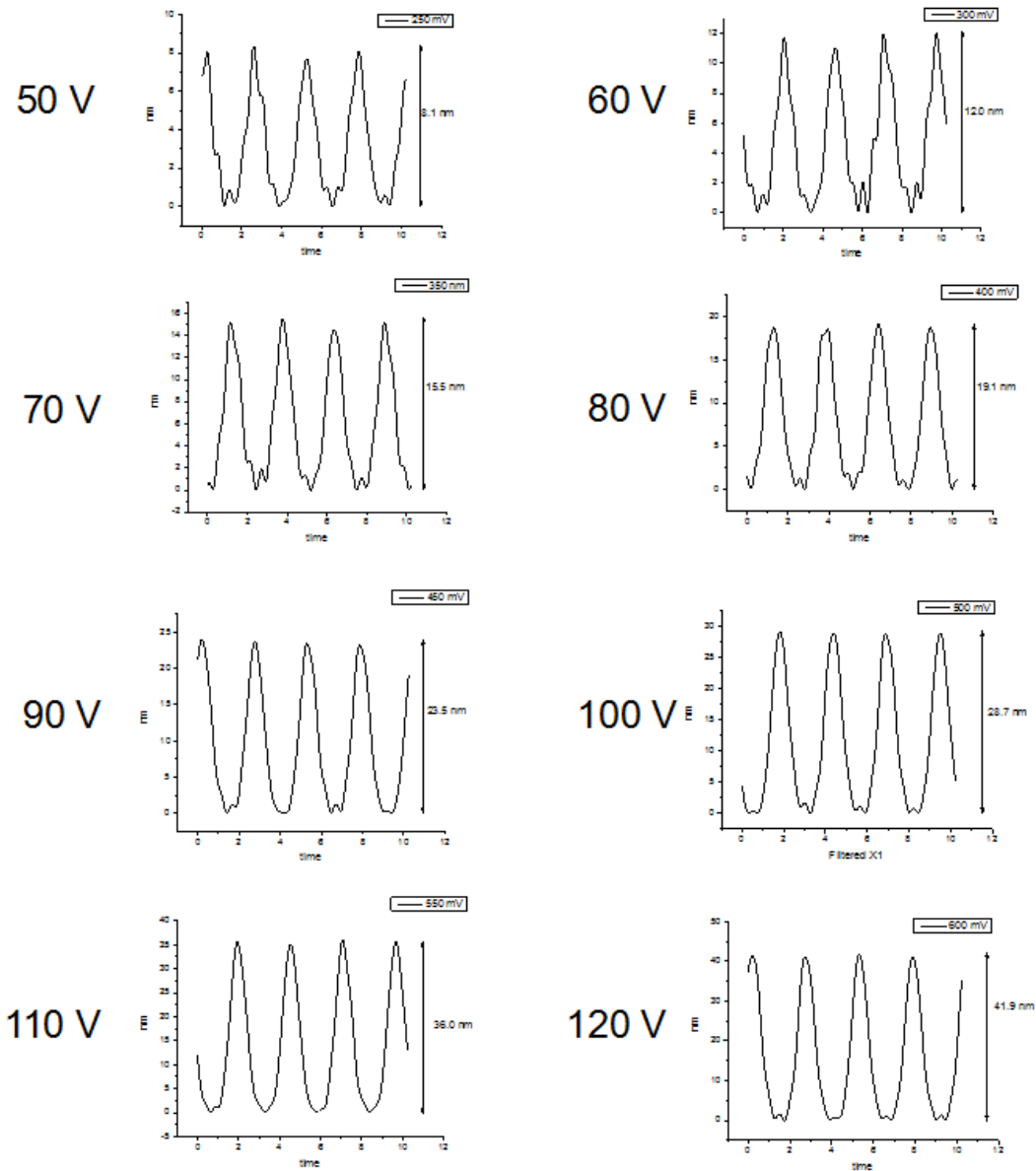


Figure 5.4 The harmonic displacement response produced by the voltage from 50V to 120V

It was illustrated in the Figure 5.5 that the displacement-voltage data can be fitted in a Quadratic Polynomial Curve. The Figure 5.5(a) and (b) exhibited this fitting for sample 1 and sample 2 respectively. The fitting curve consisted two components: the linear part and the pure quadratic part. And the coefficients for each component matched quite well in different samples. It was generally considered that there were two major sources of quadratic term in Strain-Electrical field relationship: the Maxwell stress and the electrostrictive effect. For the linear correlation, the only option was the piezoelectric effect. Since the induced piezoelectric response had its own

polarity orientation based on the electrical poling process, the electrical measurements should have reversed responses when the connection of electrical field was reversed. The fundamental origin of these two components will be discussed as below.

1. Maxwell stress. The Maxwell stress originated from free charges on electrodes, its value can be calculated by:

$$S = -\frac{1}{2} s \varepsilon E^2 = -\frac{1}{2} s \varepsilon V^2 / h^2 = -\frac{1}{2} \cdot \frac{1}{0.5 \times 10^9} \cdot 5 \times 8.85 \times 10^{-12} \cdot \frac{1}{(40 \times 10^{-6})^2} \cdot V^2$$

$$= -0.0125 \times 10^{-9} \cdot V^2$$

$$X = Sh = -5 \times 10^{-16} \cdot V^2$$

which was much lower than the fitted coefficient (2.6×10^{-12}). Thus, the quadratic term discovered in this test cannot be the contribution of Maxwell stress.

2. The calculation of electrostrictive coefficient. For: ε - the total strain in 3 thickness direction; ε_1 - the strain brought by piezoelectric effect; ε_2 - the strain brought by electrostrictive effect; X -displacement; h - thickness (40 μ m); V-voltage

$$\varepsilon = \varepsilon_1 + \varepsilon_2; \varepsilon = \frac{X}{h}; \varepsilon_1 = d_{33}E = d_{33} \frac{V}{h}; \varepsilon_2 = M_{33}E^2 = M_{33} \frac{V^2}{h^2}$$

Thus:

$$\frac{X}{h} = d_{33} \frac{V}{h} + M_{33} \frac{V^2}{h^2}$$

$$X = d_{33}V + M_{33} \frac{V^2}{h}$$

in sample 1: $d_{33}=-31.5\text{pm/V}$, $M_{33}=-104 \times 10^{-18}\text{m}^2\text{V}^{-2}$

in sample 2: $d_{33}=-58\text{pm/V}$, $M_{33}=-88 \times 10^{-18}\text{m}^2\text{V}^{-2}$

Since it seemed the Maxwell stress impossible to produce such a high quadratic term. The

remaining option was the electrostrictive effect. The calculated M_{33} was much higher than the normal reported value (around $2 \times 10^{-18} \text{m}^2 \text{V}^{-2}$ for commercial samples, $10 \times 10^{-18} \text{m}^2 \text{V}^{-2}$ for electron irradiate samples). However giant electrostrictive effect with M_{33} up to $100 \times 10^{-18} \text{m}^2 \text{V}^{-2}$ in several PVDF copolymers were reported. The possible mechanism for this giant electrostrictive effect will be discussed in section 5.3.

It was clear the opposite sign of linear coefficient (0.0315 and -0.058) were caused by the reversed circuit in the two samples. The calculated d_{33} was also higher than expectation, considering the measured samples were prepared by as-printed PVDF thin films without post poling procedure. (It will be analyzed in the following subsection in detail)

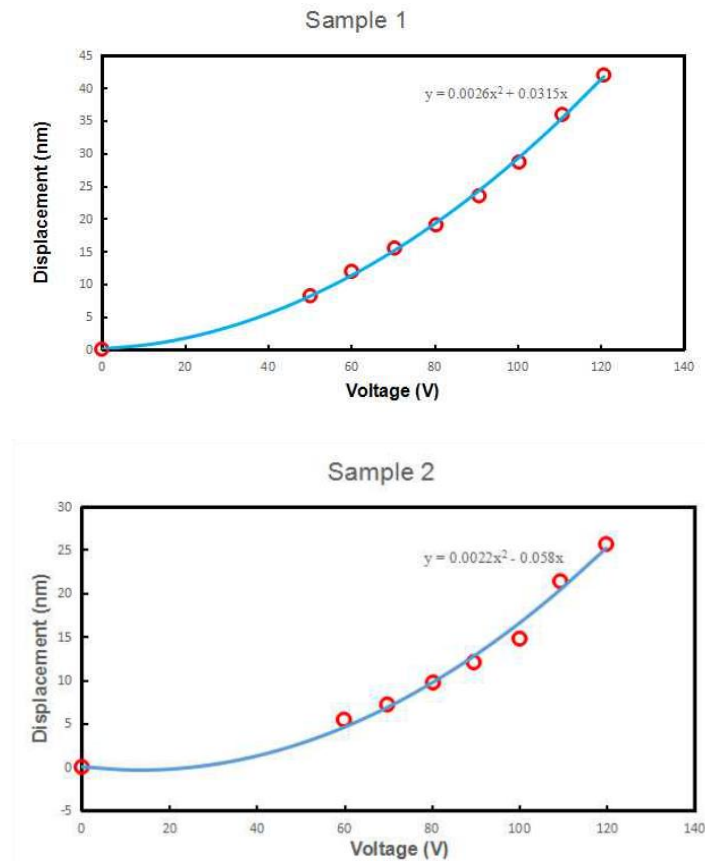


Figure 5.5 The polynomial regression of displacement response for two randomly picked samples (a) sample 1, and (b) sample 2.

5.2.2. The simplified model for the measured d_{33} values

A high fitted d_{33} value was obtained in the PFM test. At first, people may wonder if this high value is real considering the low level of polarization by the in-situ poling procedure. One problem to verify the origin of the linear term was that there was a large discrepancy between the fitted d_{33} value (-31.5pm/V~-58pm/V) in PFM and the d_{33} values attained from d_{33} meter (-4pm/V~-9pm/V). Although the value was still very high, considering the low P_r value. But how to understand the large discrepancy between the value obtained from different method? This phenomenon can be explained by the special distribution of polarization we have discussed in the previous section. Some brief theoretical derivation was given below to provide a brief explanation.

The concept of polarized region and active region in PVDF thin films:

As discussed in previous chapter, the charges throughout the thickness of PVDF thin film are majorly transported by the electron. When the PVDF thin film was subject to applied stress, only the region nearby the electrode can transport the compensate charges for dipole orientation to the electrode. And only if the electrical displacement induced by the direct piezoelectric effect reached the electrode, the piezoelectric material of this region can really influence the sensitivity. Thus, we called the region in PVDF film which can really influence the sensitivity as active region. It was reported that the active region was about 3.5 μm or 1/10 of the whole thickness (35 μm). It was also reported in the same literature⁶⁴ that remnant polarization is unevenly distributed throughout the thickness direction. During the poling process with low electrical field, the polarized region was highly correlated with the active region. Because the polarization can be stabilized by the transportation of compensate charges. And most polarization in the internal region will disappear after the electrical field was removed. When the ultra-thin PVDF film (thinner than 1 μm), it was clear the whole region throughout the thickness was active. At the same time, because the compensate charges from any region can be transported to the electrode, the region throughout whole thickness can be considered as polarized region. For the printed PVDF, because the film was fabricated layer by layer, and for each layer, the applied electrical field, and poling time was equivalent. The polarized region was uniformly distributed throughout

the whole thickness, although the value of polarization is still low, because of the much lower electrical field (less than 1MV/m) than the normal poling procedure (more than 30MV/m). However, because the thickness of printed was close to those common processed PVDF thin films, the active region should still similar with those common processed one. Thus, in the printed PVDF thin films, the polarized region and active region were no longer coincided with each other just as the cases in the common processed films and ultra-thin films. The spatial distributions of polarized region and active region throughout the thickness direction in common PVDF thin films, printed PVDF thin films, and ultra-thin PVDF films were shown in Figure 5.6 respectively.

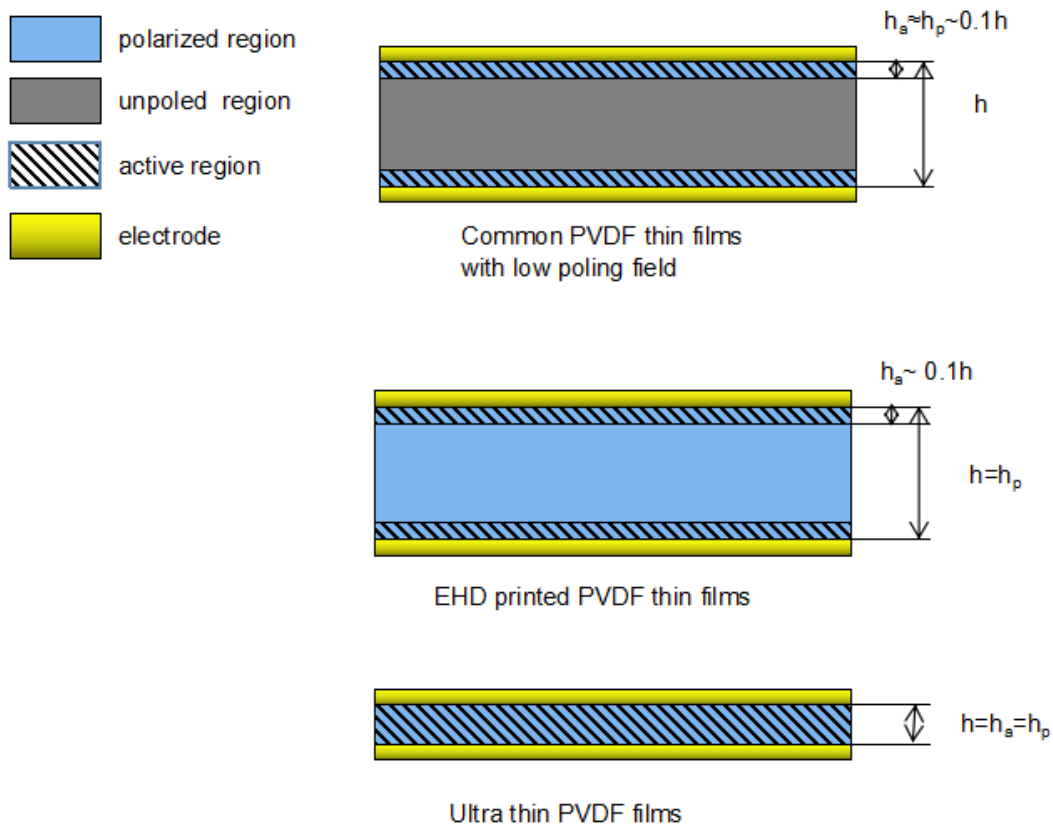


Figure 5.6 The distribution of the polarized region and the active region of the printed PVDF thin films compared with common processed PVDF thin films (with low poling field) and the ultra thin PVDF films.

Where:

The whole volume in PVDF film: V

The whole thickness throughout the film: h

Volume of polarized region: V_p

Thickness of polarized region: h_p

Number of domain in polarized region: n_p

Domain density in polarized region: ρ_p , $n_p = V_p \rho_p$

Volume of active region: V_a

Thickness of the active region: h_a

The value of h_a is about $0.1h$

The calculation of piezoelectric effects on single domain:

In PFM testing, the converse piezoelectric effect was applied where we denote the tested d_{33} as $d_{33}^{(1)}$

In d_{33} meter, the direct piezoelectric effect was applied, where we denote the tested d_{33} as $d_{33}^{(2)}$.

To simplify the calculation, we suppose each single domain has the same dimension, with piezoelectric coefficient d_0 ; total numbers of the domain n ; the volume of each single domain V_0 ; domain density ρ .

In PFM testing, under the applied electrical field (E), the induced strain in each domain: $S_0 = Ed_0$

In d_{33} meter, similar with the above analysis, under the applied stress (T), the induced electrical displacement: $D_0 = Td_0$

The contribution of single domain to the whole:

Then we analyze the contribution of single domain to the whole PVDF film.

In converse piezoelectric effect, the tested strain can be calculated by:

$$S = n_p \int_V S / V = \rho_p V_p S_0 V_0 / V$$

In direct piezoelectric effect, the tested electrical displacement can be calculated by:

$$D = n_a \int_V D / V = \rho_p V_a D_0 V_0 / V$$

From this calculation, it was found, an important difference between converse piezoelectric effect and direct piezoelectric effect lied on the active region. In the formal case, every poled

domain can contribute to the strain induced by the electrical field. In the latter case, only the poled domain located in active region can contribute to the electrical displacement induced by the applied stress.

The comparison of d_{33} tested by different piezoelectric effect.

Using the calculated S and D, divided by E and T value, the tested value in PFM and d_{33} meter can be obtained and compared with each other:

$$d_{33}^{(1)} = S/E = n_p S_0 V_0 / V = V_p \rho_p V_0 d_0 / V$$

$$d_{33}^{(2)} = D/T = n_a S_0 V_0 / V = V_a \rho_p V_0 d_0 / V$$

$$d_{33}^{(1)} / d_{33}^{(2)} = V_p / V_a = 2h_p / h_a$$

For normal PVDF thin film, $h_p = h_a$, $d_{33}^{(1)} = d_{33}^{(2)}$

For ultra-thin PVDF thin film $h_p = h_a$, $d_{33}^{(1)} = d_{33}^{(2)}$

For Printed thin film, $d_{33}^{(1)} / d_{33}^{(2)} = h_p / 2h_a = 5$

From this simplified model, it was clear that when the normal fabricated PVDF film or ultrathin PVDF film were characterized using PFM and d_{33} meter respectively, there will be close values for both cases ($\rho_a V_a d_0$). If the printed samples were tested, there will be a large discrepancy between the two method. The ratio between the two value ($d_{33}^{(1)} / d_{33}^{(2)}$) was depending on the ratio $h / 2h_a$ (about 5 in this case). Thus, according to the obtained d_{33} value (-31.5 pm/V and -58 pm/V) in PFM, the corresponding value in d_{33} meter will be -6.3~-11.6 pm/V. This is very close to the value obtained from d_{33} meter (-5~-8 pC/N). This discussion showed that the fitted linear value can precisely reflect the d_{33} value in its converse piezoelectric effect.

At this moment, the large discrepancy between the d_{33} value obtained by different testing methods for the printed PVDF thin film was explained. The fitted d_{33} value is real (up to -58 pm/V), but it cannot be applied in sensing application at this moment. As a sensor, it only corresponded the value of -6.3~-11.6 pC/N.

5.2.3. The electret structure and giant electrostrictive

A giant electrostrictive effect was discovered in the PFM test. The possible mechanism was the special electret structure in the EHD printed PVDF thin film.

The analysis of printing process and the printed electret structure:

In previous studies, three important factors have been identified to play an important role on the EHD printing process: (1) the production of charge carriers; (2) charge transfer as electrical currency; (3) residual charge in solid state⁹⁸. The primary factor that makes jet injection possible is the generation of excess charge accumulation in solution. In the case of applied electric field, Taylor cone is generated in the region close to the tip, which is eventually affected by the electrostatic force, resulting in fluid jet, thus depositing the desired film. The charge transfer from the charge solution to the substrate produces a significant current. This current transport may occur not only by the ink jet, it also exists in the atmosphere around printing equipment. The undissipated charge generated in the fluid remains in the cured film and exists in the form of residual charge.

In the printing process, the transport and distribution of charges in ink results in stress, which leads to fluid flow. The grounding electrodes of the high voltage source are connected under the substrate as the target of the polymer jet driven by electrostatic force. When the ejected stream forms a filament, which passes through the Taylor cone at the tip of the capillary and deposits on the substrate, part of the solvent component is lost due to evaporation, and the remaining polymer solution diffuses and solidifies into the film structure, which is the whole physical process of film formation. Figure 5.7 describes the generation, transmission, dissipation and residue of charges during printing.

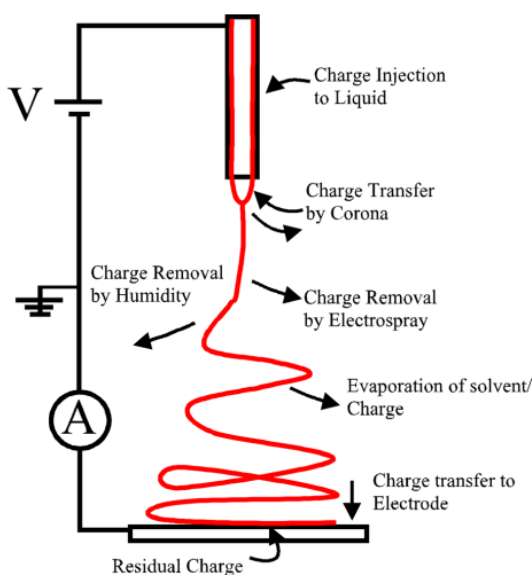


Figure 5.7 Schematic diagram of a typical EHD printing process. The charge injection and transportation is described⁹⁸.

After solidification, any charges that dissipate in the ink jet are trapped in the inner film. Because PVDF film solids are electrically insulated in nature, there is no way to capture the charge as a constant current through the insulating film to the conductive substrate. Of course, there must be other mechanisms to slow the release of these residual charges. However, on most experimental surfaces, this residual charge can exist stably within the polymer for a considerable period of time.

As described by Filitov et al.⁹⁸, the deposition of charged ink jet on the substrate will obviously change the electric field distribution in the point-plane system. When charged fibers accumulate on the collector, the electric field of the Taylor cone decreases slowly due to the presence of charges on the substrate. As the electric field decreases to the threshold required for injection, the ink injection process will be terminated. This is why we need to print films directly on insulated glass substrates rather than conductive substrates. In addition, this mechanism limits the thickness of the printed film to about 80 microns. It is shown in Figure 5.8⁹⁸ that some residual charges on the polymer film after the partial charges on the jet are dissipated, and the resulting electret structure is essentially an electret structure. Electrodes can disperse this excess charge

through different mechanisms, depending on a series of parameters including the dielectric properties of polymers, solvents, ambient humidity and temperature. The location of the charge trapped also strongly affects the process.

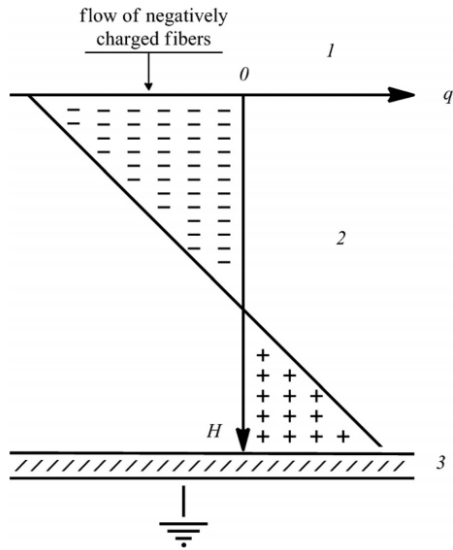


Figure 5.8 Distribution of trapped electric charges. (1) space between electrodes; (2) layer of material; (3) substrate and electrode. ⁹⁸

Before discussing the mechanism of charge dissipation, it is important to ask where the excess charge exists in the polymer and in what form. In-depth studies of electret physics have shown that there are many ways to inject charges into polymers. Moreover, the polarization of the material may be caused by either the deflection of dipole direction in the material or the actual charge injection. Conversely, injecting charges into polymers can also be achieved by the reorientation of permanent dipole moments in directional polymers or polarizing the moving charges inside the polymers. Space charges can also be injected into polymers by other methods, including Corona Polarization and Ion Beam. In EHD printing, due to the intrinsic dielectric properties of the printed polymer, the charge injection mechanism is intrinsically realized in the printing process.

In polymer electrets, charge storage depends on a series of parameters, such as crystallinity, polymer structure, additive¹²⁷, etc. Residual charge is generally easy to combine with various traps in materials: in hemicrystalline polymers, it is believed that there are many defects at the interface between crystals and amorphous regions, as well as in the interior of spherulites; in pure amorphous polymers, charge is trapped in some specific areas of its structure, such as heteroatoms and aromatic ring¹²⁷. According to Sessler⁹⁸ data, surface traps may be caused by surface stacking faults, impurities and adsorbed molecules, while volume traps are located at three different levels: atomic sites, molecular chains and heterogeneous particles. The counterpart part of charge storage or capture is charge dissipation, which depends on the motion activity of charge in the medium. Temperature plays a key role in these mechanisms because molecular activation caused by chain motion is the main cause of predation. In addition, different conducting mechanism (holes or electrons) may vary greatly in mobility.

Mechanism of electrostrictive effect in the printed PVDF

Early studies showed that the piezoelectric properties of ordinary PVDF ferroelectric copolymers originated from their electrostrictive effect¹²⁸. Therefore, this high electrostrictive strain response stimulates our interest in applying this giant electrostrictive effect to enhance its piezoelectricity. Giant electrostrictive strain response was reported in Electron Irradiated P (VDF-TrFE) copolymer³¹. Under high electric field, the electrostrictive strain response can be obtained up to 4%.

As shown in Fig. 5.9, direct piezoelectric response can be induced by external DC bias in Electron Irradiated copolymers samples. Fig. 5.9 (a) showed a very good linear relationship between polarization and applied stress. The nominal piezoelectric coefficient d_{31} of the electronically irradiated PVDF-TrFE copolymer was 116 pC/N. Under 40 MV/m electric field, it can reach 5 times that of the ordinary ferroelectric PVDF-TrFE copolymer³⁸. Fig. 5.9 (b) also showed that the piezoelectric coefficients of Electron Irradiated copolymers can be adjusted by DC bias field. It is reported that there is a difference between the d_{31} values obtained from reverse and direct piezoelectric measurements. The higher d_{31} calculated by inverse piezoelectric effect may come from other factors such as Maxwell stress effect¹³⁰. This phenomenon was

quite similar with the FPM result observed in our study.

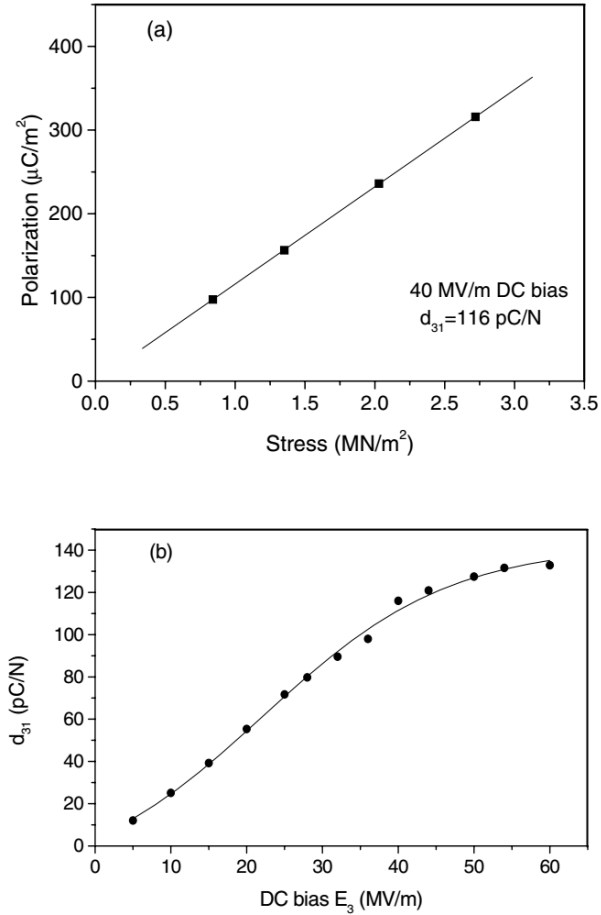


Figure 5.9 Direct piezoelectric effect in electron irradiated PVDF-TrFE 50/50 copolymers: a) polarization versus stress at 40 MV/m bias field, b) d_{31} versus DC bias field strength¹²⁹

In most insulating polymers, the electrostrictive effect is generally weak. One of the main reasons for the lower electrostrictive stress in polymers is the low dielectric constant. The experimental results showed that the M values of most polymers with elastic modulus of 1 GPa were lower than $2 \times 10^{-20} \text{ m}^2/\text{V}^2$. Therefore, even under electric field of 100 MV/m, the electrostrictive strain was lower than 2×10^{-4} . Polymers with low elastic modulus may have relatively larger electrostrictive coefficients. For example, in high energy electron irradiated (HEEI) P(VDF-TrFE) copolymers, about 5% of the electrostriction can be obtained under electrical field of 150 MV/m. As shown in Fig. 5.10 (a), the strain had a linear relationship with

P^2 , which indicated an essentially electrostrictive strain. For HEEI copolymers, Q_{33} can vary from -4 to $-15\text{m}^2/\text{C}$ depending on the processing conditions of the samples. As shown in Fig. 5.10 (b), the strain of the polymer did not change significantly with temperature.

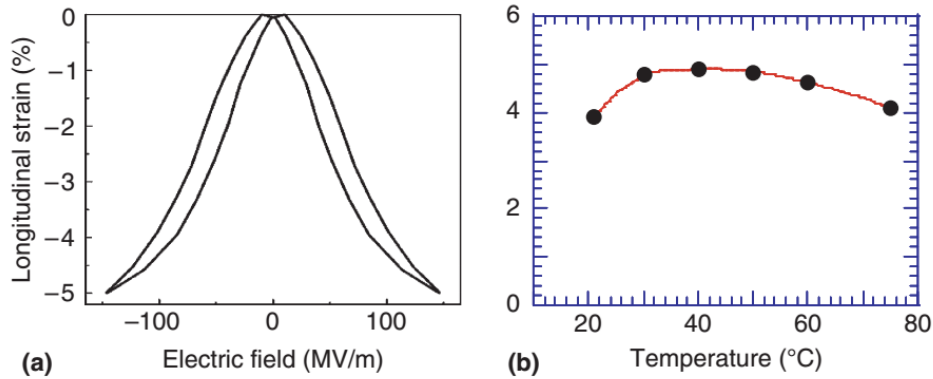


Figure 5.10 Longitudinal strain in a high-energy electron irradiated P(VDF-TrFE) copolymer, (a) with respect to the varied electric fields; and (b) with respect to the varied temperatures³²

P (VDF-TrFE) 56/44ml% copolymer under high energy proton irradiation also obtained high electrostrictive strain. The M_{33} measured from the copolymer is about $-1.83 \times 10^{-18} \text{m}^2/\text{V}^2$, which is approximately the same as that obtained from HEEI copolymer. While using the fitting data, M_{33} value of $-1.6 \times 10^{-15} \text{m}^2/\text{V}^2$ was obtained which was much higher than the corresponding data in HEEI copolymer. The author believed that one of the main effects of irradiation is the formation of a three-dimensional network of high crosslinking density P (VDF-TrFE) using free radical crosslinkers and adjuvants. Moreover, the grain size under the applied electric field is greatly reduced due to the high degree of cross-linking.

This giant electrostrictive may be related to a special microstructure produced in this special PVDF thin film structure, which is called electret structure. All of those printed drops include positive charge, with the evaporation of the solvent, most of them have no time to dissipate, and will be locked inside the film structure. This microstructure produced by locking the high density of space charges inside the bulk of materials is called electret structure. And these space charges (SC) usually result in some special electroactive properties of the materials. Coincidentally a widely accepted mechanism for the giant electrostrictive effect in PVDF and its copolymers was the crosslinking of polymer chains by the charged particles. In fact, this crosslinking structure itself

is one kind of electret structure, because it consisted of charged particles inside the material. The high electroactive effect in polymers was always connected with the electret structure introduced above. The method (electron irradiation) to produce this structure in PVDF was also the most frequently applied method to produce other electret polymers. This mechanism can also explain why this printed PVDF thin film had such a high electrostrictive effect than those sample produced by other method: It is clear that the printed PVDF thin films should have a much higher space charge density than the electron irradiated one. However, so far there was still not any direct evidence to support the electret structure and this giant electrostrictive effect.

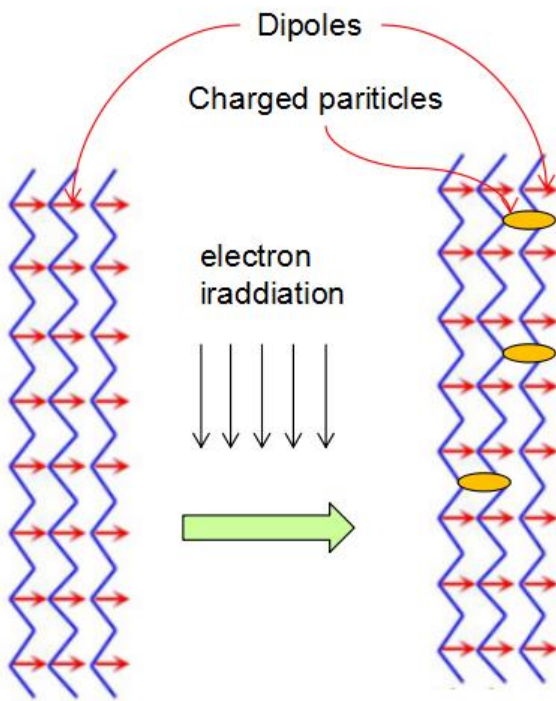


Figure 5.11 The mechanism for Giant electrostrictive effect in PVDF and its copolymers (Cross linking)

The influence of the electrostrictive effects on the piezoelectric properties in PVDF thin films:

To increase the piezoelectric response of the polymers, there were several methods to be applied. One method was based on the increase of remnant polarization. This method was realized either by synthesizing new polymers to increase the dipole concentration of the monomer unit⁴⁵, or by

adjusting the poling process to maximize the dipole orientation in a given structure. Almost all the conventional methods to improve the piezoelectricity were based on this mechanism. In fact, the piezoelectric performance of materials was not only decided by the remnant polarization. The electrostrictive property can also strongly influence the piezoelectric performance. In real research and development of piezoelectric material, the electrostrictive property were usually simplified as constant, and the fundamental within the electrostrictive property were not well understood. Thus it was difficult to promote the piezoelectricity by intentionally maneuvering its electrostrictive coefficients. From the estimation in section 4.2, there was not any switched dipole under the printing condition and the post printing treatment on our process platform. However, the electret structure produced by the EHD printing process could result in extra switched dipoles because of the compensation effects of the space charges. Besides, it was intensively reported that the ion bombardment/ionizing radiation can result in extremely high electrostrictivity in PVDF copolymers. Since the whole printed PVDF thin film was composed by the ions (charged particles), we may expect the similar phenomena occurred in ionizing radiated samples. It would be interesting to study how this special microstructure could influence the properties of the printed PVDF thin film, especially its piezoelectric performance.

The electrets structure can even directly increase the piezoelectric performance of polymer material. Unlike polar nonporous polymers, this material generally does not contain micro-dipoles. On the contrary, symmetrical breaking occurs on macro scale, due to the separation of positive and negative charges in the gap and the capture of charges by the inner surface of the cell structure. Therefore, the change of dipole moment leads to the quasi-piezoelectric behavior of these materials when mechanical stress is applied to the polymer surface.

5.3. Piezoelectric characterization of PVDF sensors in 31 mode of operation

In order to obtain the piezoelectric coefficients (d_{31}) as well as the sensitivity of PVDF in 31 mode for the various thin film samples used throughout this experiment, a beam bending method

was utilized. This method coupled the modal analysis of a cantilevered beam under its first natural frequency and used lock-in amplifier or charge amplifier to record data. In this section, first the governing beam bending equations for the cantilevered beam will be derived and explained. Next, an in-depth discussion of the lock-in amplifier and the microstrain will be presented. After that, the experimental set-up and procedure will be explained. The experimental results will be obtained through this experiment and then discussed.

5.3.1. Experimental setup of instrument in 31 mode of operation

The purpose of this analysis was to determine the strain in the Z direction in PVDF film samples. Since the beam in the experiment was vibrating at a constant frequency, ω , the differential equation describing the beams behavior was dependent on position only (it was independent of time). The equation was as follows¹³² :

$$\frac{d^4W(x)}{dx^4} - \beta^4W(x) = 0, \quad 0 < x < L$$

Where: $\beta^4 = \frac{\omega^2 m}{EI}$, ω is the frequency of the beam, m is the linear mass of the beam; E is the Young's Modulus of the beam; and I is the beam's area moment of inertia.

The general solution for this differential equation is:

$$W(x) = C_1 \sin(\beta x) + C_2 \cos(\beta x) + C_3 \sinh(\beta x) + \cosh(\beta x)$$

In the case of the experiment, a cantilevered beam was utilized. This beam was illustrated as below:

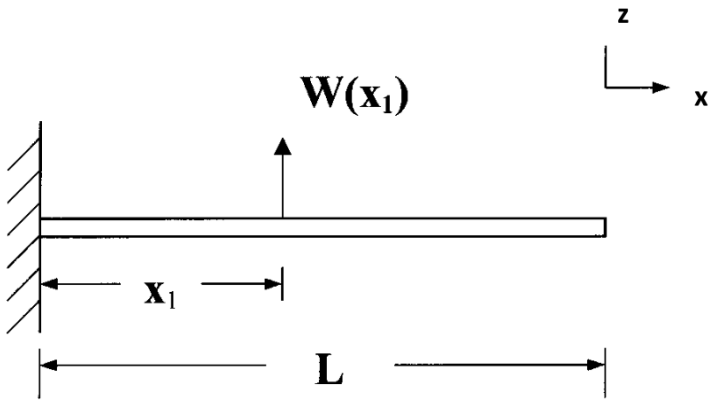


Figure 5.12 The setup of a Cantilever Beam¹³²

From the definition of the 31 mode of operation, it was evident that the applied stress in this mode was in the longitudinal direction, or the 1 direction. This can be achieved in multiple ways. As an example, consider a PVDF sensor that was bonded to a flexible substrate. Upon bending of the structure, the PVDF sensor experiences significant stress along the 1 direction because the neutral axis no longer passes through the center of the PVDF. Another example of 31 mode was bonding the PVDF sensor to the sides of a beam and impacting it at the top. This was usually the method used in the impact tests on the aluminum beams.

In the experiment using the solid beam, PVDF sensors were bonded to the sides of the beam. During each impact event, the shaker hits the bottom of the solid bar. The force exerted by the shaker led to the development of longitudinal strain in the bar. The PVDF sensors bonded to the side of the bar were also subjected to the impact-induced longitudinal strain. In an ideal case, the amount of strain on the surface of the beam at the location where the PVDF sensor was bonded would be the same as the amount of strain in the PVDF sensor. However, the PVDF film in the sensor was separated from the solid beam's surface by layers of Mylar, silver ink electrode, and cyanoacrylate glue. Hence there was a small difference in the amount of strain developed in the PVDF film and the amount of strain developed in the solid bar at the PVDF sensor's location. Thus, the strain acting along the 1 direction led to the development of stress in the 1 direction, thereby causing the generation of voltage by the PVDF sensor.

Measurement of the PVDF sensor's voltage: A PVDF sensor was capacitive in nature. A model

for the equivalent circuit of a PVDF sensor was required in order to analyze the interfacing circuit between the PVDF sensor and the measurement system. There were two equivalent circuit models that can be used for the PVDF sensor. The PVDF sensor can be modeled either as a voltage source in series with the PVDF film capacitance or as a charge source shunted by the internal resistance in parallel with PVDF film capacitance.

The voltage source model was shown in Figure 5.4(a), in which V_s denoted the voltage generated by the sensor (which is directly proportional to the applied stress), C_s denotes the internal capacitance of the PVDF film, and V_t is the voltage available across the terminals of the PVDF sensor. The charge source model was shown in Figure 5.4(b). In both cases, the part of the circuit inside the dotted rectangle comprised the PVDF sensor. The voltage source equivalent circuit model of the PVDF sensor was most commonly used for analysis of interfacing circuits. An oscilloscope (Agilent 54622A) was used to record the voltage generated by the PVDF sensor because it satisfied both criteria mentioned above. The oscilloscope had a maximum input voltage rating of 400V and a sampling rate of 100MHz. The PVDF sensor's terminals were connected to 10× probes (Agilent 10074C), which were connected to the input terminals of the oscilloscope¹²³.

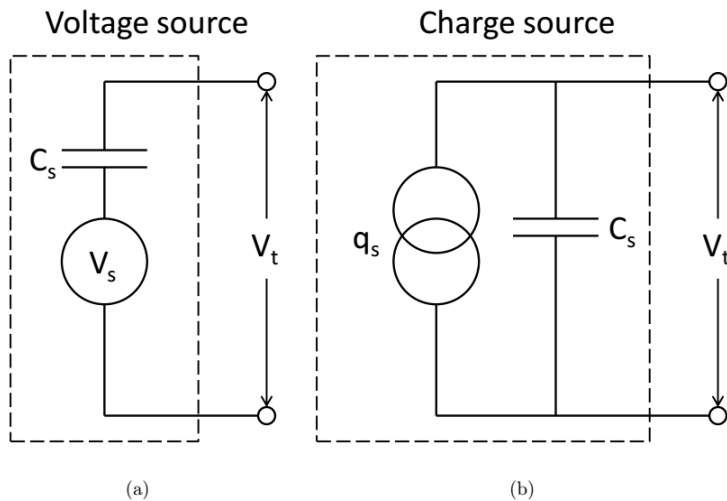


Figure 5.13 Diagram showing (a) the voltage source and (b) the charge source equivalent circuit models of a PVDF sensor¹³².

Amplifier Electronics: Because the sensor element acts as a current source in operation, charge amplifier can be used to minimize the input impedance and electric field, thereby reducing the influence of sensor and line capacitance. The circuit shown in Fig. 5.14 acts as a single pole high-pass filter and achieves a sufficiently low cut-off frequency to detect correctly the signal response³⁷ in the range of 1Hz-1000hz. The transfer function of the circuit is as follows:

$$H(s) = \frac{V_{out}(s)}{V_{in}(s)} = \frac{sRC_s}{sRC + 1}$$

Properly designing the system can lead to a low corner frequency calculated as below:

$$f_c = \frac{1}{2\pi RC}$$

The signal was then subject to low-pass filtered with a cut-off frequency to remove unwanted signals and conditioned for input to the analog to digital converter (ADC).

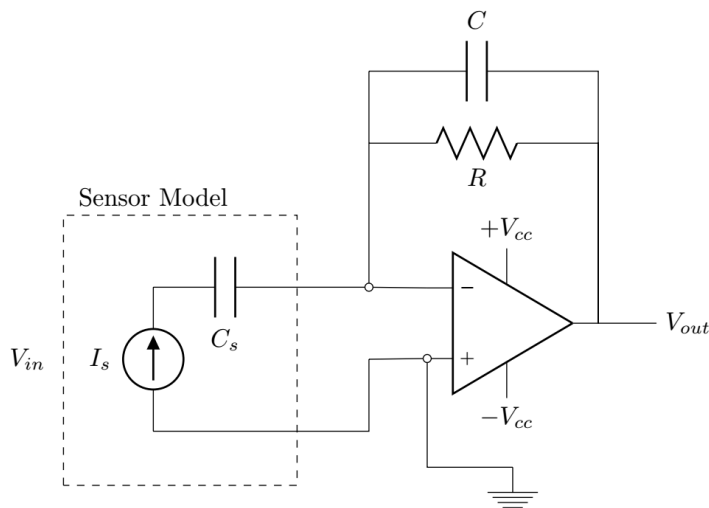


Figure 5.14 Charge Amplifier Circuit Design¹³²

Otherwise, in this experiment, a model SR830 DSP Lock-in Amplifier was also used. Therefore, it is important that the signal frequency and the Lock-in frequency are equal (this is done automatically by the Lock-in amplifier). A Lock-in amplifier requires a reference frequency

(provided in the case of this experiment by an external function generator). The Lock-in amplifier can only detect the response from the experimental equipment at the reference frequency. By utilizing a low pass filter, only signals with frequencies that are close to the reference frequency of the Lock-in amplifier will be measured. Other signals with frequencies far from the reference frequency will be attenuated. The bandwidth of the low pass filter determines the degree to which signals will be attenuated. Again, only signals that have a frequency equal to the reference signal will result in a true DC PSD output signal and will be completely unaffected by the low pass filter. These are the signals that we wished to measure.

5.3.2. Testing d_{31} of PVDF thin film by the cantilever beam method

The electromechanical properties d_{31} of the printed PVDF sensor films were characterized using a cantilever-based setup shown in Figure 5.15. The sensor was mounted on the top surface of the steel cantilever, just for the purpose of sensor characterization. The specimen was fixed at one end and deformed by an actuator at the other end. The loud speaker was used to initiate the structural vibration, and a lock-in amplifier and ampere meter was used to monitor the vibration of the beam. The generated current from the PVDF sensors was measured by a lock-in amplifier. The whole system will sit in an environmental controlled chamber to obtain responses representative of in-service condition.

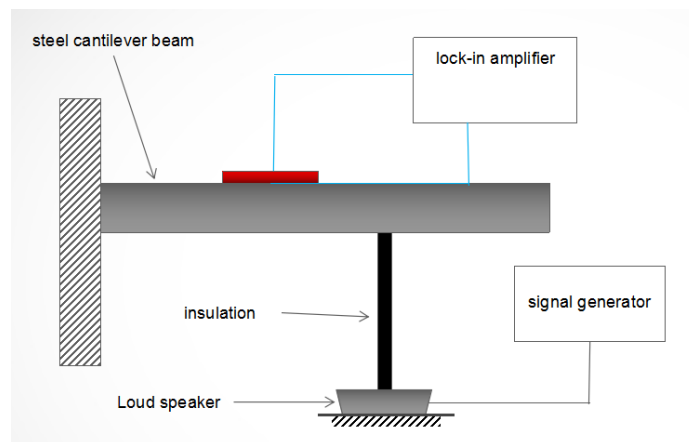


Figure 5.15 The setup of d_{31} characterization tester system using cantilever beam method

Calculation: A typical piezoelectric film can be considered as a parallel plate capacitor, whose capacitance is calculated by¹³³:

$$V_c = q / C_p$$

$$C_p = \frac{e_{33}^{\sigma} l_c b_c}{t_c}$$

where l_c , b_c and t_c are length, width, and thickness of the sensor respectively.

The voltage generated by the sensor can be expressed as:

$$V_c = \frac{d_{31} Y_c b_c}{C_p} \int_{l_c} \varepsilon_1 dx$$

Assuming the value of ε_1 to be averaged over the gage length, and defining a sensitivity parameter

$$S_q = d_{31} Y_c l_c b_c$$

where Y_c is the Young's modulus of the material.

The equation relating strain and voltage generated by the sensor is

$$\varepsilon_1 = \frac{V_c C_p}{S_q}$$

Considering only the charge generated by strain in the 1-direction, the current i can be expressed as

$$\begin{aligned} i = \dot{q} &= d_{31} Y_c l_c b_c \dot{\varepsilon}_1 \\ &= S_q \dot{\varepsilon}_1 \end{aligned}$$

Based on the above analysis, and integrate the current through out a period, the effective current can be calculated as ¹³³:

$$I = d_{31} Y_c A \varepsilon / \Delta t,$$

where I is the generated current, d_{31} is the piezoelectric constant, Y_c is Young's modulus of PVDF film, A is the cross-sectional area of PVDF thin film, and ε is the applied strain.

It should be pointed out that the deduction of the above equation is based on the basic assumption that only 1 direction of strain contributes to the charges on electrode, and the effect of other strain components can be neglected, in addition, there is no strain loss in the bond layer. Finally, d_{31} can be calculated as follows:

$$d_{31} = \frac{I_{eff}}{\sqrt{2\pi Y_c A f \varepsilon_0}}$$

In this experiment, the PVDF film was mounted on the surface of the cantilever beam with repeated bending. The piezoelectric coefficient d_{31} was characterized by the current and voltage response with respect to the alternative strain. The bending displacement were obtained by the keyence VHx2000 3D microscopes. Below is the calculated result with randomly selected frequency (370Hz and 560Hz). We choose this frequency in order to avoid the interference of the natural frequency of the beam.

Although the obtained value was much lower than the d_{31} value of about 30pC/N from commercial PVDF thin films. It should be noted that the poling process was not applied on this printed PVDF. In other study using the melt printing process, the d_{31} value of 1.19pC/N was obtained⁷⁴. ChaBum Lee at al.¹²⁴ even reported the d_{33} value as low as 0.26pC/N obtained by printing. The much higher value of d_{31} in this study should be related to the giant electrostrictive effect.

Table 5.2 The calculated d_{31} value with varied frequency

f(Hz)	I (nA)	d_{31} (pC/N)
370	15.28	3.05
560	20.2	2.65

5.3.3. Free vibration sensing testing

Free vibration sensing testing was another method to test the sensitivity of the PVDF film in 31 mode. Both the free vibration testing and the later described load frame testing were analogous to testing performed on carbon nanotube/PVDF composite films by Ramaratnam and Jalili¹³⁴. Specifically, the free vibration testing was performed similarly to testing on PZT-based piezoelectric paint by Zhang¹³⁵. This test helped to determine if the film would be an effective dynamic strain sensor.

The selected test article was a 7075-aluminum alloy beam with a size of 0.7×5.5×66 cm. Figure 5.16(a) showed the setup of applied external load via a electrical shaker to produce low-frequency excitation. The physical map of experimental setup was shown in Figure 5.16 (b). The two ends of the aluminum beam were clamped, and the distance between the shaker and the PVDF piezoelectric sensor was 20cm. The induced electric outputs from the sensor were measured using a voltage measurement meter. Because the piezoelectric sensor was stimulated, the feedback signal will be generated. The performance of the sensor can be evaluated after effective collection and analysis of the generated feedback signal.

In order to make sure the PVDF piezoelectric sensor be closely bonded with aluminum beam, DP460 strong glue (produced by 3M company) was used. The sensor was directly bonded to aluminum beam, and then the performance test was carried out after it was completely cured. The glue was applied uniformly to the surface of the PVDF sensor using a brush applicator. The PVDF sensor was then pressed against the surface of the solid beam using a flat headed piece of steel block. This caused the excess glue to squeeze out from under the PVDF sensor and resulted in more uniform adhesion.

The major instruments used in the test included: DG022U signal generator to change the vibration parameters of the exciter; uT4104F charge signal amplifier to amplify the signal to shield noise waves; EDUX1002A digital oscilloscope to collect feedback signals.

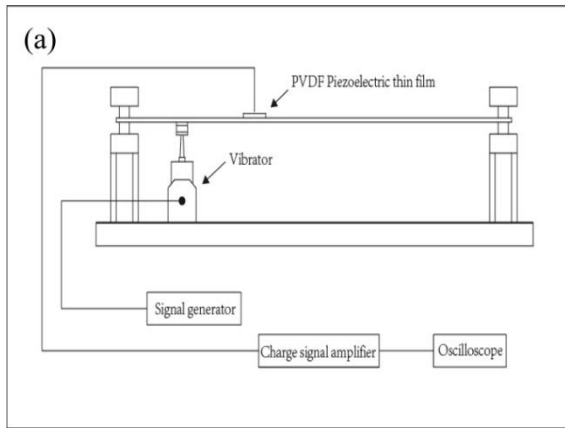


Figure 5.16 A vibration measurement system (a) schematic (b) physical map

In actual measurement, the charge signal generated by PVDF piezoelectric sensor was quite weak, thus it was difficult to directly collect electrical signal by oscilloscope. Otherwise, an interference signal with a fixed frequency of 50Hz was always appeared, and the interference effect of this signal cannot be ignored. To address this problem, we select the charge amplifier with Low pass filter (produced by Wuhan Youtai Electronic Technology Co., Ltd).

In order to eliminate the measurement errors and reduce the external interference, we should pay attention to the following points:

- (1) During the test, the lead and coaxial cables should be fixed to prevent the signal interference caused by the shaking or moving of the conductor.
- (2) The environment needs to be quiet, or the platform be placed on the shock absorber.

This section used commercial PVDF sensor (produced by MEAS) as control group. The effective

working area of the sensor was 10mm×15mm, and the accuracy was 1.4V/g~1.6V/g. The material of the beam was aluminum. The dimension of the beam was 7×55×660 mm. The PVDF sensors were bonded to the beam at a distance of about 67 mm from each free end. The sensor was mounted on the aluminum beam by the super glue (502 glue). The vibration mode, frequency and amplitude of the exciter were adjusted by the function signal generator. The signal was collected by the oscilloscope after the charge amplification. In order to make the experiment convenient for operation and analysis, sine wave form was selected as an excitation signal.

Fig. 5.17 showed the feedback signal of commercial PVDF sensor under fixed excitation voltage (peak value $10V_{pp}$) with varied frequencies (10Hz, 15Hz, 20Hz). The result exhibited that the feedback signal of printed PVDF piezoelectric film was still sinusoidal, which correlated well with the excitation signal. In the frequency range of 10 Hz to 20 Hz, the feedback signal amplitude of printed PVDF piezoelectric thin films had a small increase with the increasing frequency, but not obvious. The sensor feedback was almost not affected by the varied frequency in this frequency range, probably due to the same vibration amplitude with varied excitation frequency.

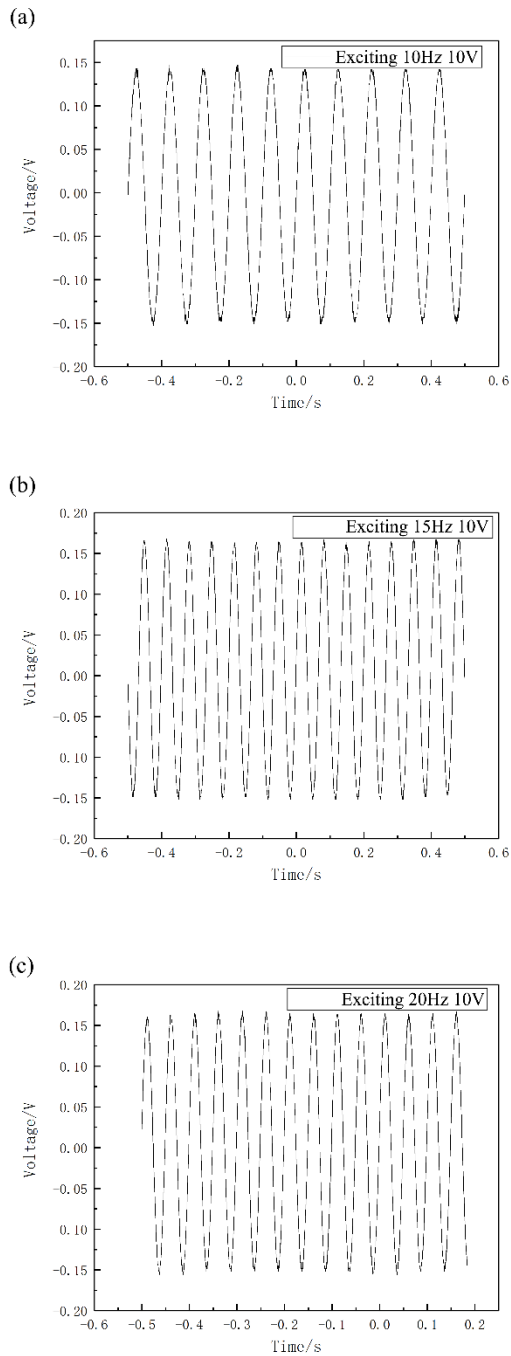


Figure 5.17 Output voltage of PVDF piezoelectric thin film at the input frequency of (a)10Hz, (b)15Hz and (c)20 Hz, with 10V voltage input on shaker.

The purpose of this study was to conduct a so-called proof-of-concept measurements in order to confirm that the sensors manufactured can be used in SHM applications. In addition, compared with the reference sensor, the printed sensor had a comparable sensitivity values.

Figure 5.18 was the respond signal of commercial PVDF film at fixed excitation frequency (frequency 10 Hz) and varied excitation voltage (1V, 5V, and 10V).

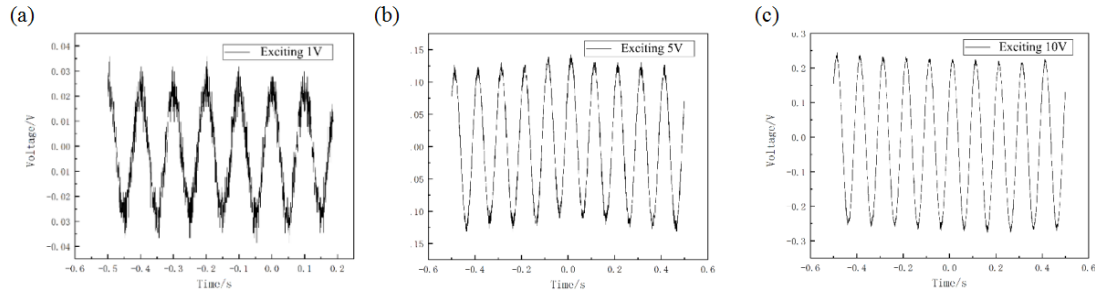


Figure 5.18 The voltage response signal in commercial PVDF sensor under varied excitation voltages

Figure 5.19 was the respond signal of printed PVDF piezoelectric thin film at fixed excitation frequency (frequency 10 Hz) and varied input voltages (1V, 5V, and 10V).

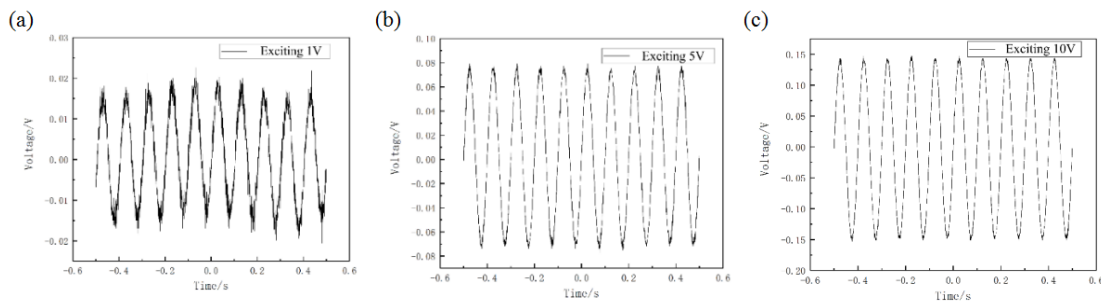


Figure 5.19 The voltage response signal in printed PVDF sensor under varied excitation voltages

From Figure 5.16 and Figure 5.17, it was clear that the respond voltage in both the commercial PVDF sensors and the printed PVDF sensors had strong dependence on the excitation voltage. In order to clearly exhibit this relationship between the two sensor feedback signals and the excitation signals, the linear regression was shown in Figure 5.20.

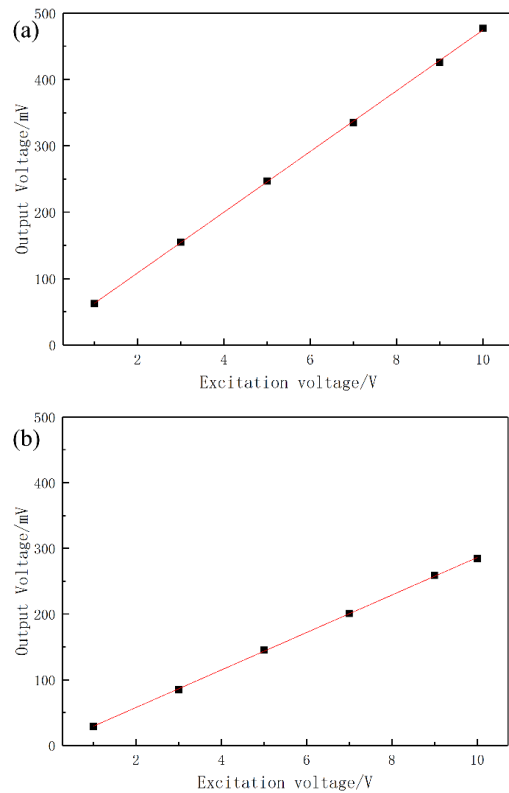


Figure 5.20 Response of feedback signal to excitation signal for (a) commercial PVDF sensor, and (b) printed PVDF sensor

By comparing the slope in Figure 5.20(a) and (b), it can be shown that the sensitivity of the printed PVDF sensor was lower than that of the commercial PVDF sensor. The reasons may be as follows: First, commercial PVDF sensors are prepared by uniaxial stretching followed by thermal polarization, and the polarization effect of commercial samples was much better than in-situ polarization of the printed sample without any post printing poling step. Secondly, the commercial PVDF sensor had lower dielectric loss, lower resistance and higher capacitance because of its more compact and uniform internal structure. Thirdly, the packaging and wiring processes of commercial PVDF sensors were better than the related processes mentioned in this study. Although the performance of the printed PVDF piezoelectric thin film sensor was lower than that of commercial one, it was hopeful that the performance of PVDF piezoelectric thin film sensor can be further improved by continuously improving the beta phase content of PVDF thin film, optimizing the printing process and the electrode preparation method of the sensor. And more important, if the post poling step was conducted, there will be a huge increase on the sensitivity, considering the possible giant electrostrictive effect brought by the special electret

microstructure in this printed thin film. So far, the EHD jet printing technology proved its capability as a simple, low-cost and efficient method for preparing piezoelectric materials and devices.

In this chapter, we evaluated the PVDF sensors prepared by the as printed samples without any post printing poling. Although the sensitivity was still not high enough, but the result was anticipated and acceptable, considering not any post poling procedure were applied. For the next step of the study, there are three options: 1. By the optimization of the material processing, we already obtained the PVDF thin film with d_{33} up to 10 pc/N, and with sensitivity close to commercial sensors. We can continue the current processing without poling and develop the smart layer for some location that doesn't need very high sensitivity. 2. Since a giant electrostrictive effect was discovered, it would be promising to develop the smart layer used in actuator or energy harvest. 3. We can make some modification and optimization in this printing process, to obtain the sensor even exceed its current theoretical highest value. And try to integrate this post poling process into the printing platform.

6. Summary

1. Piezoelectric PVDF thin films with high β phase content (83%) and high crystallinity (68%) were produced by the EHD printing technology.
2. A new β phase formation mechanism was proposed to provide a solid guidance for the Additive Manufacturing of PVDF thin film and the following processing.
3. Varied parameters in the printing process were systematically investigated, including solvent selection, doping with additives, temperature, wt% of PVDF solution, voltage, printing speed, and the heat treatment.
4. The poling methods and mechanisms for the PVDF thin films were discussed and the poling technology on the printing platform is explored.
5. The printed PVDF without poling exhibited a relatively high piezoelectric coefficient (d_{33} up to 8 pC/N, d_{31} up to 3.05 pC/N).
6. A giant electrostrictive effect with M_{33} up to $-104 \times 10^{-18} \text{m}^2 \text{v}^{-2}$ was discovered in the printed PVDF thin films, which could provide a new method to promote the sensitivity of PVDF sensors.
7. Preliminary free vibration tests were conducted on the printed sensors, which exhibit good responses to the stress signals with low frequency. The performances of printed sensors (without poling) are comparable but a little lower than commercial ones.

References

- 1 D. (D.) Zhao, 'Study of a New Manufacturing Technology for Multi-Functional Composite Structures with Aerosol-Jet Printing' (Florida State University, 2011).
- 2 F. Aymerich, and W.J. Staszewski, 'Experimental Study of Impact-Damage Detection in Composite Laminates Using a Cross-Modulation Vibro-Acoustic Technique', *Structural Health Monitoring*, 9 (2010), 541-53.
- 3 Victor Giurgiutiu, *Structural Health Monitoring: With Piezoelectric Wafer Active Sensors* (Elsevier, 2007).
- 4 Ji-Hun Bae, and Seung-Hwan Chang, 'Characterization of an Electroactive Polymer (Pvdf-Trfe) Film-Type Sensor for Health Monitoring of Composite Structures', *Composite Structures*, 131 (2015), 1090-98.
- 5 Xinlin P. Qing, Shawn J. Beard, Amrita Kumar, Teng K. Ooi, and Fu-Kuo Chang, 'Built-in Sensor Network for Structural Health Monitoring of Composite Structure', *Journal of Intelligent Material Systems and Structures*, 18 (2006), 39-49.
- 6 S. Yashiro, T. Okabe, and N. Takeda, 'Damage Identification in a Holed Cfrp Laminate Using a Chirped Fiber Bragg Grating Sensor', *Composites Science and Technology*, 67 (2007), 286-95.
- 7 U. and H. Tzou Gabbert, *Smart Structures and Structronic Systems* (Kluwer Academic Publisher, 2001).
- 8 Hyonny Kim, Myounggu Park, and Kelli Hsieh, 'Fatigue Fracture of Embedded Copper Conductors in Multifunctional Composite Structures', *Composites Science and Technology*, 66 (2006), 1010-21.
- 9 Dibakar Bandopadhyaya, Bishakh Bhattacharya, and Ashish Dutta, 'Modeling of Hybrid Damping Scheme Using Smart Magnetostrictive Composites for Flexible Manipulator', *Journal of Reinforced Plastics and Composites*, 26 (2007), 861-80.
- 10 Ning Hu, Hisao Fukunaga, and Masaki Kameyama, 'Identification of Delaminations in Composite Laminates', *Journal of Intelligent Material Systems and Structures*, 17 (2006), 671-83.
- 11 S. Hurlbaeus, and L. Gaul, 'Smart Structure Dynamics', *Mechanical Systems and Signal Processing*, 20 (2006), 255-81.
- 12 D. C. Lee, J. J. Lee, and S. J. Yun, 'The Mechanical Characteristics of Smart Composite Structures with Embedded Optical Fiber Sensors', *Composite Structures*, 32 (1995), 39-50.
- 13 A. Riccio, F. Scaramuzzino, and P. Perugini, 'Embedded Delamination Growth in Composite Panels under Compressive Load', *Composites Part B: Engineering*, 32 (2001), 209-18.
- 14 A. Abu Obaid, and S. Yarlagadda, 'Structural Performance of the Glass Fiber–Vinyl Ester Composites with Interlaminar Copper Inserts', *Composites Part A: Applied Science and Manufacturing*, 39 (2008), 195-203.
- 15 Kang Hyun-Kyu, Kang Dong-Hoon, Hong Chang-Sun, and Kim Chun-Gon, 'Simultaneous Monitoring of Strain and Temperature During and after Cure of Unsymmetric Composite Laminate Using Fibre-Optic Sensors', *Smart Materials and Structures*, 12 (2003), 29.

- 16 Lan Yao, and Yiping Qiu, 'Design and Fabrication of Microstrip Antennas Integrated in Three Dimensional Orthogonal Woven Composites', *Composites Science and Technology*, 69 (2009), 1004-08.
- 17 T. Pereira, Zhanhu Guo, S. Nieh, J. Arias, and H. Thomas Hahn, 'Embedding Thin-Film Lithium Energy Cells in Structural Composites', *Composites Science and Technology*, 68 (2008), 1935-41.
- 18 Jeffrey M. Lawrence, Pierre Frey, Ahmad Abu Obaid, Shridhar Yarlagadda, and Suresh G. Advani, 'Simulation and Validation of Resin Flow During Manufacturing of Composite Panels Containing Embedded Impermeable Inserts with the Vartm Process', *Polymer Composites*, 28 (2007), 442-50.
- 19 T. A. Dawood, R. A. Shenoi, and M. Sahin, 'A Procedure to Embed Fibre Bragg Grating Strain Sensors into Gfrp Sandwich Structures', *Composites Part A: Applied Science and Manufacturing*, 38 (2007), 217-26.
- 20 R. Hadzic, S. John, and I. Herszberg, 'Structural Integrity Analysis of Embedded Optical Fibres in Composite Structures', *Composite Structures*, 47 (1999), 759-65.
- 21 B. Dauda, 'Delamination of Multilayer Textile Reinforced Structural Composites' (University of Manchester, 2008).
- 22 Mark Lin, and Fu-Kuo Chang, 'The Manufacture of Composite Structures with a Built-in Network of Piezoceramics', *Composites Science and Technology*, 62 (2002), 919-39.
- 23 Xinlin Qing Mark Lin, Amrita Kumar, Shawn J. Beard, 'Smart Layer and Smart Suitcase for Structural Health Monitoring Applications', (DTIC Document, 2001).
- 24 Laura Bechthold, Veronika Fischer, Andre Hainzmaier, Daniel Hugenroth, Ljudmila Ivanova, Kristina Kroth, Benedikt Römer, Edyta Sikorska, and Vincent Sitzmann, '3d Printing: A Qualitative Assessment of Applications, Recent Trends and the Technology's Future Potential', (Studien zum deutschen Innovationssystem, 2015).
- 25 Robert Bogue, '3d Printing: An Emerging Technology for Sensor Fabrication', *Sensor Review*, 36 (2016), 333-38.
- 26 Kambiz Chizari, Mohamed Amine Daoud, Anil Raj Ravindran, and Daniel Therriault, '3d Printing of Highly Conductive Nanocomposites for the Functional Optimization of Liquid Sensors', *Small*, 12 (2016), 6076-82.
- 27 Henry Helvajian, 'Chapter 14 - 3d Microengineering Via Laser Direct-Write Processing Approaches', in *Direct-Write Technologies for Rapid Prototyping*, ed. by Alberto Piqué (San Diego: Academic Press, 2002), pp. 415-74.
- 28 K Blake Perez, and Christopher B Williams, 'Combining Additive Manufacturing and Direct Write for Integrated Electronics—a Review', in *24th International Solid Freeform Fabrication Symposium—An Additive Manufacturing Conference, SFF* (2013), pp. 962-79.
- 29 R. Gregorio, and E. M. Ueno, 'Effect of Crystalline Phase, Orientation and Temperature on the Dielectric Properties of Poly (Vinylidene Fluoride) (Pvdf)', *Journal of Materials Science*, 34 (1999), 4489-500.
- 30 Haisheng Xu, G. Shanthi, V. Bharti, Q. M. Zhang, and T. Ramotowski, 'Structural, Conformational, and Polarization Changes of Poly(Vinylidene Fluoride–Trifluoroethylene) Copolymer Induced by High-Energy Electron Irradiation', *Macromolecules*, 33 (2000), 4125-31.
- 31 (!!! INVALID CITATION !!!).

- 32 Ahmad Safari, and E. Koray Akdogan, *Piezoelectric and Acoustic Materials for Transducer Applications*. (Springer Science & Business Media, 2008).
- 33 Bartosz Mika, 'Design and Testing of Piezoelectric Sensors' (Texas A & M University, 2010).
- 34 S. Trolier-McKinstry, and P. Muralt, 'Thin Film Piezoelectrics for Mems', *Journal of Electroceramics*, 12 (2004), 7-17.
- 35 S. Jassim, A. M. Al-Jumaily, A. J. Easteal, D. Dodd, and D. Crofts, 'Piezoelectric Polymer with Some Optical Characteristics', *Polymer Testing*, 21 (2002), 519-22.
- 36 Aleksandra Vinogradov, and Frank Holloway, 'Electro-Mechanical Properties of the Piezoelectric Polymer PvdF', *Ferroelectrics*, 226 (1999), 169-81.
- 37 James Michael Wooten, 'High-Dynamic Range Collision Detection Using Piezoelectric Polymer Films for Planar and Non-Planar Applications', (2013).
- 38 Andrew J. Lovinger, 'Ferroelectric Polymers', *Science*, 220 (1983), 1115.
- 39 J. B. Lando, and W. W. Doll, 'The Polymorphism of Poly(Vinylidene Fluoride). I. The Effect of Head-to-Head Structure', *Journal of Macromolecular Science, Part B*, 2 (1968), 205-18.
- 40 J. F. Legrand, 'Structure and Ferroelectric Properties of P(Vdf-Trfe) Copolymers', *Ferroelectrics*, 91 (1989), 303-17.
- 41 M. A. Bachmann, and J. B. Lando, 'A Reexamination of the Crystal Structure of Phase II of Poly(Vinylidene Fluoride)', *Macromolecules*, 14 (1981), 40-46.
- 42 Takeo Furukawa, 'Ferroelectric Properties of Vinylidene Fluoride Copolymers', *Phase Transitions*, 18 (1989), 143-211.
- 43 Kiran Kumar Chatrathi, 'Microfabrication and Characterization of PvdF Copolymer Thin Films Suitable for Integrating with Optical Microsystems' (Concordia University, 2006).
- 44 K. Tashiro, K. Takano, M. Kobayashi, Y. Chatani, and H. Tadokoro, 'Structural Study on Ferroelectric Phase Transition of Vinylidene Fluoride-Trifluoroethylene Copolymers (Iii) Dependence of Transitional Behavior on Vdf Molar Content', *Ferroelectrics*, 57 (1984), 297-326.
- 45 Cheol Park, Zoubeida Ounaies, Kristopher E. Wise, and Joycelyn S. Harrison, 'In Situ Poling and Imidization of Amorphous Piezoelectric Polyimides', *Polymer*, 45 (2004), 5417-25.
- 46 Ohigashi Hiroji, Watanabe Takashi, Li Guo Rong, Hattori Takeshi, and Takahashi Sadayuki, 'Piezoelectric Properties of B-Form PvdF Films Crystallized at High Pressure and Their Applications to Heat-Resistant Ultrasonic Transducers', *Japanese Journal of Applied Physics*, 30 (1991), 111.
- 47 VT Rathod, D Roy Mahapatra, Anjana Jain, and A Gayathri, 'Characterization of a Large-Area PvdF Thin Film for Electro-Mechanical and Ultrasonic Sensing Applications', *Sensors and Actuators A: Physical*, 163 (2010), 164-71.
- 48 Shuting Chen, Xue Li, Kui Yao, Francis Eng Hock Tay, Amit Kumar, and Kaiyang Zeng, 'Self-Polarized Ferroelectric PvdF Homopolymer Ultra-Thin Films Derived from Langmuir-Blodgett Deposition', *Polymer*, 53 (2012), 1404-08.
- 49 Ivo B. Rietveld, Kei Kobayashi, Takuya Honjo, Kenji Ishida, Hirofumi Yamada, and Kazumi Matsushige, 'Electrospray Induced Ferroelectricity in Poly(Vinylidene Fluoride) Thin Films', *Journal of Materials Chemistry*, 20 (2010), 8272-78.
- 50 V. F. Cardoso, G. Minas, C. M. Costa, C. J. Tavares, and S. Lanceros-Mendez, 'Micro and Nanofilms of Poly(Vinylidene Fluoride) with Controlled Thickness, Morphology and

- Electroactive Crystalline Phase for Sensor and Actuator Applications', *Smart Materials and Structures*, 20 (2011), 087002.
- 51 Richard J Shuford, Anthony F Wilde, John J Ricca, and George R Thomas, 'Characterization and Piezoelectric Activity, of Stretched and Poled Poly (Vinylidene Fluoride). Part I: Effect of Draw Ratio and Poling Conditions', *Polymer Engineering & Science*, 16 (1976), 25-35.
- 52 K. Matsushige, K. Nagata, S. Imada, and T. Takemura, 'The Ii-I Crystal Transformation of Poly(Vinylidene Fluoride) under Tensile and Compressional Stresses', *Polymer*, 21 (1980), 1391-97.
- 53 P. Sajkiewicz, A. Wasiak, and Z. Gocłowski, 'Phase Transitions During Stretching of Poly(Vinylidene Fluoride)', *European Polymer Journal*, 35 (1999), 423-29.
- 54 YR Wang, JM Zheng, GY Ren, PH Zhang, and C Xu, 'A Flexible Piezoelectric Force Sensor Based on PvdF Fabrics', *Smart Materials and Structures*, 20 (2011), 045009.
- 55 Erik Nilsson, Anja Lund, Christian Jonasson, Christer Johansson, and Bengt Hagström, 'Poling and Characterization of Piezoelectric Polymer Fibers for Use in Textile Sensors', *Sensors and Actuators A: Physical*, 201 (2013), 477-86.
- 56 Dipankar Mandal, 'Ultra-Thin Films of a Ferroelectric Copolymer: P (Vdf-Trfe)' (2008).
- 57 D. L. Dorset, 'X-Ray Diffraction: A Practical Approach', *Microscopy and Microanalysis*, 4 (2005), 513-15.
- 58 Robert John Bell, 'Introductory Fourier Transform Spectroscopy', *American Journal of Physics*, 41 (1973), 149-51.
- 59 Kohji Tashiro, and Masamichi Kobayashi, 'Structural Phase Transition in Ferroelectric Fluorine Polymers: X-Ray Diffraction and Infrared/Raman Spectroscopic Study', *Phase Transitions*, 18 (1989), 213-46.
- 60 Yung Ting, Suprpto, Aditya Nugraha, C. W. Chiu, and Hariyanto Gunawan, 'Design and Characterization of One-Layer PvdF Thin Film for a 3d Force Sensor', *Sensors and Actuators A: Physical*, 250 (2016), 129-37.
- 61 J. Gomes, J. Serrado Nunes, V. Sencadas, and S. Lanceros-Mendez, 'Influence of the B-Phase Content and Degree of Crystallinity on the Piezo- and Ferroelectric Properties of Poly(Vinylidene Fluoride)', *Smart Materials and Structures*, 19 (2010), 065010.
- 62 J. S. Dodds, F. N. Meyers, and K. J. Loh, 'Piezoelectric Characterization of PvdF-Trfe Thin Films Enhanced with ZnO Nanoparticles', *IEEE Sensors Journal*, 12 (2012), 1889-90.
- 63 Yong Zhang, Ivan S. Baturin, Emil Aulbach, Doru C. Lupascu, Andrei L. Kholkin, Vladimir Ya Shur, and Jürgen Rödel, 'Evolution of Bias Field and Offset Piezoelectric Coefficient in Bulk Lead Zirconate Titanate with Fatigue', *Applied Physics Letters*, 86 (2004), 012910.
- 64 E. R. Neagu, J. S. Hornsby, and D. K. Das-Gupta, 'Polarization and Space Charge Analysis in Thermally Poled PvdF', *Journal of Physics D: Applied Physics*, 35 (2002), 1229.
- 65 C. J. Dias, and D. K. Das - Gupta, 'Hysteresis Measurements on Ferroelectric Composites', *Journal of Applied Physics*, 74 (1993), 6317-21.
- 66 Gu Ying, Tong Liyong, and Tan Ping, 'Surface Strain Distribution Method for Delamination Detection Using Piezoelectric Actuators and Sensors', *Journal of Physics: Conference Series*, 305 (2011), 012077.

- 67 Sampo Tuukkanen, Tuomas Julin, Ville Rantanen, Mari Zakrzewski, Pasi Moilanen, Kaisa E. Lilja, and Satu Rajala, 'Solution-Processible Electrode Materials for a Heat-Sensitive Piezoelectric Thin-Film Sensor', *Synthetic Metals*, 162 (2012), 1987-95.
- 68 S. Kärki, M. Kiiski, M. Mäntysalo, and J. Lekkala, 'A PvdF Sensor with Printed Electrodes for Normal and Shear Stress Measurements on Sole', (2009), pp. 1765-69.
- 69 Malti Bansal, Ritu Srivastava, C. Lal, M. N. Kamalasanan, and L. S. Tanwar, 'Carbon Nanotube-Based Organic Light Emitting Diodes', *Nanoscale*, 1 (2009), 317-30.
- 70 Andreas Elschner, and Wilfried Lövenich, 'Solution-Deposited Pedot for Transparent Conductive Applications', *MRS Bulletin*, 36 (2011), 794-98.
- 71 ChaBum Lee, and Joshua A Tarbutton, 'Electric Poling-Assisted Additive Manufacturing Process for PvdF Polymer-Based Piezoelectric Device Applications', *Smart Materials and Structures*, 23 (2014), 095044.
- 72 K. Mahadeva Suresha, Berring John, Walus Konrad, and Stoeber Boris, 'Effect of Poling Time and Grid Voltage on Phase Transition and Piezoelectricity of Poly(Vinylidene Fluoride) Thin Films Using Corona Poling', *Journal of Physics D: Applied Physics*, 46 (2013), 285305.
- 73 C. Chang, Y. Fuh, and L. Lin, 'A Direct-Write Piezoelectric PvdF Nanogenerator', in *TRANSDUCERS 2009 - 2009 International Solid-State Sensors, Actuators and Microsystems Conference* (2009), pp. 1485-88.
- 74 Daniel A. Porter, Trung V. T. Hoang, and Thomas A. Berfield, 'Effects of in-Situ Poling and Process Parameters on Fused Filament Fabrication Printed PvdF Sheet Mechanical and Electrical Properties', *Additive Manufacturing*, 13 (2017), 81-92.
- 75 Madhusudan Singh, Hanna M. Haverinen, Parul Dhagat, and Ghassan E. Jabbour, 'Inkjet Printing—Process and Its Applications', *Advanced Materials*, 22 (2010), 673-85.
- 76 Jiyoung Chang, 'Electrospun Direct-Write Multi-Functional Nanofibers' (UC Berkeley, 2012).
- 77 Chieh Chang, Van H. Tran, Junbo Wang, Yiin-Kuen Fuh, and Liwei Lin, 'Direct-Write Piezoelectric Polymeric Nanogenerator with High Energy Conversion Efficiency', *Nano Letters*, 10 (2010), 726-31.
- 78 Wu Aik Yee, Masaya Kotaki, Ye Liu, and Xuehong Lu, 'Morphology, Polymorphism Behavior and Molecular Orientation of Electrospun Poly(Vinylidene Fluoride) Fibers', *Polymer*, 48 (2007), 512-21.
- 79 Sian F. Fennessey, and Richard J. Farris, 'Fabrication of Aligned and Molecularly Oriented Electrospun Polyacrylonitrile Nanofibers and the Mechanical Behavior of Their Twisted Yarns', *Polymer*, 45 (2004), 4217-25.
- 80 Dan Li, Yuliang Wang, and Younan Xia, 'Electrospinning of Polymeric and Ceramic Nanofibers as Uniaxially Aligned Arrays', *Nano Letters*, 3 (2003), 1167-71.
- 81 S. A. Theron, E. Zussman, and A. L. Yarin, 'Experimental Investigation of the Governing Parameters in the Electrospinning of Polymer Solutions', *Polymer*, 45 (2004), 2017-30.
- 82 Daoheng Sun, Chieh Chang, Sha Li, and Liwei Lin, 'Near-Field Electrospinning', *Nano Letters*, 6 (2006), 839-42.
- 83 Z. H. Liu, C. T. Pan, L. W. Lin, J. C. Huang, and Z. Y. Ou, 'Direct-Write PvdF Nonwoven Fiber Fabric Energy Harvesters Via the Hollow Cylindrical near-Field Electrospinning Process', *Smart Materials and Structures*, 23 (2014), 025003.

- 84 Juan Pu, Xiaojun Yan, Yadong Jiang, Chieh Chang, and Liwei Lin, 'Piezoelectric Actuation of Direct-Write Electrospun Fibers', *Sensors & Actuators A: Physical*, 164 (2010), 131-36.
- 85 Martin Zirkl, Anurak Sawatdee, Uta Helbig, Markus Krause, Gregor Scheipl, Elke Kraker, Peter Andersson Ersman, David Nilsson, Duncan Platt, Peter Bodö, Siegfried Bauer, Gerhard Domann, and Barbara Stadlober, 'An All-Printed Ferroelectric Active Matrix Sensor Network Based on Only Five Functional Materials Forming a Touchless Control Interface', *Advanced Materials*, 23 (2011), 2069-74.
- 86 Sampada Bodkhe, Gabrielle Turcot, Frederick P. Gosselin, and Daniel Therriault, 'One-Step Solvent Evaporation-Assisted 3d Printing of Piezoelectric PvdF Nanocomposite Structures', *ACS Applied Materials & Interfaces*, 9 (2017), 20833-42.
- 87 Haque Rubaiyet Iftekharul, Vié Rémy, Germainy Michel, Valbin Laurie, Benaben Patrick, and Boddaert Xavier, 'Inkjet Printing of High Molecular Weight PvdF-Trfe for Flexible Electronics', *Flexible and Printed Electronics*, 1 (2016), 015001.
- 88 Hong-Jie Tseng, Wei-Cheng Tian, and Wen-Jong Wu, 'P(Vdf-Trfe) Polymer-Based Thin Films Deposited on Stainless Steel Substrates Treated Using Water Dissociation for Flexible Tactile Sensor Development', *Sensors*, 13 (2013).
- 89 M. G. Broadhurst, and G. T. Davis, 'Piezo- and Pyroelectric Properties', in *Electrets*, ed. by Gerhard M. Sessler (Berlin, Heidelberg: Springer Berlin Heidelberg, 1987), pp. 285-319.
- 90 G. M. Sessler, 'Piezoelectricity in Polyvinylidene fluoride', *The Journal of the Acoustical Society of America*, 70 (1981), 1596-608.
- 91 Xiaoniu Yang, Xiaohua Kong, Susheng Tan, Gao Li, Wei Ling, and Enle Zhou, 'Spatially-Confining Crystallization of Poly(Vinylidene Fluoride)', *Polymer International*, 49 (2000), 1525-28.
- 92 C. C. Hsu, and P. H. Geil, 'Morphology - Structure - Property Relationships in Ultraquenched Poly(Vinylidene Fluoride)', *Journal of Applied Physics*, 56 (1984), 2404-11.
- 93 Dandan Song, Decai Yang, and Zhiliu Feng, 'Formation of B-Phase Microcrystals from the Melt of Pvf2-Pmma Blends Induced by Quenching', *Journal of Materials Science*, 25 (1990), 57-64.
- 94 H. Han, Y. Nakagawa, Y. Takai, K. Kikuchi, S. Tsuchitani, and Y. Kosimoto, 'Microstructure Fabrication on a B-Phase PvdF Film by Wet and Dry Etching Technology', *Journal of Micromechanics and Microengineering*, 22 (2012), 085030.
- 95 Robert Dunsch, and Jean-Marc Breguet, 'Unified Mechanical Approach to Piezoelectric Bender Modeling', *Sensors and Actuators A: Physical*, 134 (2007), 436-46.
- 96 Jr Gregorio, Rinaldo, and Marcelo Cestari, 'Effect of Crystallization Temperature on the Crystalline Phase Content and Morphology of Poly (Vinylidene Fluoride)', *Journal of Polymer Science Part B: Polymer Physics*, 32 (1994), 859-70.
- 97 M. P. Silva, R. S. Martins, H. Carvalho, J. M. Nobrega, and S. Lanceros-Mendez, 'Extrusion of Poly(Vinylidene Fluoride) Recycled Filaments: Effect of the Processing Cycles on the Degree of Crystallinity and Electroactive Phase Content', *Polymer Testing*, 32 (2013), 1041-44.
- 98 George Collins, John Federici, Yuki Imura, and Luiz H. Catalani, 'Charge Generation, Charge Transport, and Residual Charge in the Electrospinning of Polymers: A Review of Issues and Complications', *Journal of Applied Physics*, 111 (2012), 044701.

- 99 Wei Chuang, and Dong Jingyan, 'Direct Fabrication of High-Resolution Three-Dimensional Polymeric Scaffolds Using Electrohydrodynamic Hot Jet Plotting', *Journal of Micromechanics & Microengineering*, 23 (2013), 1-9.
- 100 Z. H. Liu, C. T. Pan, L. W. Lin, and H. W. Lai, 'Piezoelectric Properties of PvdF/Mwcnt Nanofiber Using near-Field Electrospinning', *Sensors and Actuators A: Physical*, 193 (2013), 13-24.
- 101 Louis Laberge Lebel, Brahim Aissa, My Ali El Khakani, and Daniel Therriault, 'Ultraviolet-Assisted Direct-Write Fabrication of Carbon Nanotube/Polymer Nanocomposite Microcoils', *Advanced Materials*, 22 (2010), 592-96.
- 102 Bruneaux Julien, Therriault Daniel, and Heuzey Marie-Claude, 'Micro-Extrusion of Organic Inks for Direct-Write Assembly', *Journal of Micromechanics and Microengineering*, 18 (2008), 115020.
- 103 Gregory M. Gratson, Mingjie Xu, and Jennifer A. Lewis, 'Direct Writing of Three-Dimensional Webs', *Nature*, 428 (2004), 386.
- 104 J. E. Smay, G. M. Gratson, R. F. Shepherd, J. Cesarano, and J. A. Lewis, 'Directed Colloidal Assembly of 3d Periodic Structures', *Advanced Materials*, 14 (2002), 1279-83.
- 105 Jennifer N. Hanson Shepherd, Sara T. Parker, Robert F. Shepherd, Martha U. Gillette, Jennifer A. Lewis, and Ralph G. Nuzzo, '3d Microperiodic Hydrogel Scaffolds for Robust Neuronal Cultures', *Advanced Functional Materials*, 21 (2010), 47-54.
- 106 Axel Mellinger, 'Dielectric Resonance Spectroscopy: A Versatile Tool in the Quest for Better Piezoelectric Polymers', *IEEE Transactions on Dielectrics & Electrical Insulation*, 10 (2003), 842.
- 107 T. Furukawa, M. Date, and G. E. Johnson, 'Polarization Reversal Associated with Rotation of Chain Molecules in B - Phase Polyvinylidene Fluoride', *Journal of Applied Physics*, 54 (1983), 1540-46.
- 108 T. T. Wang, H. Von Seggern, J. E. West, and H. D. Keith, 'High Field Poling of Poly(Vinylidene Fluoride) Films Using a Current Limiting Circuit', *Ferroelectrics*, 61 (1984), 249-56.
- 109 D. Rollik, S. Bauer, and R. Gerhard-Multhaupt, 'Separate Contributions to the Pyroelectricity in Poly(Vinylidene Fluoride) from the Amorphous and Crystalline Phases, as Well as from Their Interface', *Journal of Applied Physics*, 85 (1999), 3282-88.
- 110 R. A. Pethrick, 'The Applications of Ferroelectric Polymers Edited by T. T. Wang, J. M. Herbert and A. M. Glass, Blackie, Glasgow, 1988. Pp. Xii + 387, Price £55.00. Isbn 0-216-92008-6', *British Polymer Journal*, 20 (1988), 533-33.
- 111 Daniel Mason Esterly, 'Manufacturing of Poly (Vinylidene Fluoride) and Evaluation of Its Mechanical Properties' (Diss, Virginia Tech, 2002).
- 112 D. K. Das-Gupta, and K. Doughty, 'Piezoelectricity in Uniaxially Stretched and Corona Poled Polyvinylidene Fluoride', *Journal of Physics D: Applied Physics*, 13 (1980), 95-105.
- 113 H. Kliem, and R. Tadros-Morgane, 'Extrinsic Versus Intrinsic Ferroelectric Switching: Experimental Investigations Using Ultra-Thin PvdF Langmuir-Blodgett Films', *Journal of Physics D: Applied Physics*, 38 (2005), 1860-68.
- 114 T. Kaura, R. Nath, and M. M. Perlman, 'Simultaneous Stretching and Corona Poling of PvdF Films', *Journal of Physics D: Applied Physics*, 24 (1991), 1848-52.

- 115 Yadong Jiang, Yun Ye, Junsheng Yu, Zhiming Wu, Wei Li, Jianhua Xu, and Guangzhong Xie, 'Study of Thermally Poled and Corona Charged Poly(Vinylidene Fluoride) Films', *Polymer Engineering & Science*, 47 (2007), 1344-50.
- 116 D. Schilling, K. Dransfeld, E. Bihler, K. Holdik, and W. Eisenmenger, 'Polarization Profiles of Polyvinylidene Fluoride Films Polarized by a Focused Electron Beam', *Journal of Applied Physics*, 65 (1989), 269-75.
- 117 G. M. Sessler, and R. Gerhard-Multhaupt, 'A Review of Methods for Charge- or Field-Distribution Studies on Radiation-Charged Dielectric Films', *Radiation Physics and Chemistry* (1977), 23 (1984), 363-70.
- 118 Bernd Ploss, Rudolf Emmerich, and Siegfried Bauer, 'Thermal Wave Probing of Pyroelectric Distributions in the Surface Region of Ferroelectric Materials: A New Method for the Analysis', *Journal of Applied Physics*, 72 (1992), 5363-70.
- 119 Sidney B. Lang, and Yin Qing-Rui, 'Spatial Distributions of Polarization and Space Charge in Tin-Substituted Lead Zirconate Titanate Ceramics Using Laser Intensity Modulation Method (Limm)', *Ferroelectrics*, 74 (1987), 357-68.
- 120 J. C. Filippini, and C. T. Meyer, 'Water Treeing Using the Water Needle Method: The Influence of the Magnitude of the Electric Field at the Needle Tip', *IEEE Transactions on Electrical Insulation*, 23 (1988), 275-78.
- 121 M. Date T. Furukawa, 'Ferroelectric Switching Characteristics in a Copolymer of Vinylidene Fluoride and Trifluoroethylene', *Journal of applied physics*, 56 (1984), 1481-86.
- 122 T. Furukawa, and G. E. Johnson, 'Measurements of Ferroelectric Switching Characteristics in Polyvinylidene Fluoride', *Applied Physics Letters*, 38 (1981), 1027-29.
- 123 Kunal Kotian, 'Detection of in-Plane Stress Waves with Polyvinylidene Fluoride (Pvdf) Sensors' (The Ohio State University, 2013).
- 124 Joshua A Tarbutton Max B Kirkpatrick, and Tue Le, 'Characterization of 3d Printed Piezoelectric Sensors: Determination of D33 Piezoelectric Coefficient for 3d Printed Polyvinylidene Fluoride Sensors.', *SENSORS, 2016 IEEE* (2016).
- 125 V. V. Shvartsman, B. Dkhil, and A. L. Kholkin, 'Mesoscale Domains and Nature of the Relaxor State by Piezoresponse Force Microscopy', *Annual Review of Materials Research*, 43 (2013), 423-49.
- 126 Michel Cloupeau, and Bernard Prunet-Foch, 'Electrohydrodynamic Spraying Functioning Modes: A Critical Review', *Journal of Aerosol Science*, 25 (1994), 1021-36.
- 127 Anu Mishra, 'Studies of Polymer Electrets. I. Factors Governing the Stabilities of Homoelectrets Obtained from Poly(1-Olefin)S', *Journal of Applied Polymer Science*, 27 (1982), 381-95.
- 128 Furukawa Takeo, and Seo Naoya, 'Electrostriction as the Origin of Piezoelectricity in Ferroelectric Polymers', *Japanese Journal of Applied Physics*, 29 (1990), 675.
- 129 W. Ma, I. Chou, T. Karaki, and L. E. Cross, 'Dielectric and Field-Induced Piezoelectric Responses in Electron-Irradiated Poly(Vinylidene Fluoride- Trifluoroethylene) Copolymer', *physica status solidi (a)*, 194 (2002), 349-57.
- 130 R. E. Newnham, V. Sundar, R. Yimnirun, J. Su, and Q. M. Zhang, 'Electrostriction: Nonlinear Electromechanical Coupling in Solid Dielectrics', *The Journal of Physical Chemistry B*, 101 (1997), 10141-50.
- 131 Haisheng Xu, Z. Y. Cheng, Dana Olson, T. Mai, Q. M. Zhang, and G. Kavarnos, 'Ferroelectric and Electromechanical Properties of

- Poly(Vinylidene-Fluoride-Trifluoroethylene-Chlorotrifluoroethylene) Terpolymer', *Applied Physics Letters*, 78 (2001), 2360-62.
- 132 Sankar Thiruvannamalai, 'Flexoelectric and Ferroelectric Properties of Quenched Polyvinylidene Fluoride (Pvdf) Homopolymer Films' (State University of New York at Buffalo, 2010).
- 133 Jayant Sirohi, and Inderjit Chopra, 'Fundamental Understanding of Piezoelectric Strain Sensors', *Journal of Intelligent Material Systems and Structures*, 11 (2000), 246-57.
- 134 Arun Ramaratnam, and Nader Jalili, 'Reinforcement of Piezoelectric Polymers with Carbon Nanotubes: Pathway to Next-Generation Sensors', *Journal of Intelligent Material Systems and Structures*, 17 (2006), 199-208.
- 135 Yunfeng Zhang, 'In Situ Fatigue Crack Detection Using Piezoelectric Paint Sensor', *Journal of Intelligent Material Systems and Structures*, 17 (2006), 843-52.